UNIVERSITY OF CAPE TOWN
IYUNIVESITHI YASEKAPA • UNIVERSITEIT VAN KAAPSTAD

Adhesive Properties of Thermoset Fibre Metal Laminates

Talita van Tonder

BISRU

Blast Impact Survivability Research Unit

The financial assistance of the National Research Foundation (NRF) towards this research is hereby acknowledged. Opinions expressed and conclusions arrived at, are those of the author and are not necessarily to be attributed to the NRF

ABSTRACT

Fibre metal laminates (FMLs) are composite materials that consist of layers of metal and fibre reinforced polymers. FMLs are used in the construction of aircraft fuselage skins, such as the Airbus A380. GLARE, the only commercially available FML, is of particular interest due to its damage tolerance and potential impact and blast resistance.

GLARE is not commercially available and attempts at manufacturing FMLs similar to GLARE at the Blast Impact Survivability and Research Unit (BISRU) laboratories have been unsuccessful. The FMLs readily exhibited debonding between the aluminium and glass fibre reinforced epoxy, often upon handling prior to impact or blast events. The purpose of this study was therefore to investigate manufacturing techniques in order to produce FMLs that would be able to withstand impact and blast loads. Adhesive surface pre-treatment techniques and manufacturing methods typically employed in aircraft construction were investigated with particular emphasis on the adhesion of aluminium to epoxy in FMLs. This interface was of particular interest as good bonding facilitates load transfer under dynamic loading and was identified as the point of failure of the previously manufactured FMLs.

The effects of surface treatment techniques used to enhance adhesion were investigated under quasi-static conditions using Single Leg Bend tests. Chemical surface treatments such as alodining, etching, anodising, silane treatments and combinations thereof were investigated. The effect of resin and the inclusion of a film adhesive were also investigated. The silane treatments were identified as the chemical treatments that provided the best adhesion, however the film adhesive significantly improved the fracture toughness regardless of the chemical surface treatment.

FMLs were manufactured for low velocity impact loading using different chemical surface treatments for comparison, all of which included a film adhesive. The performance of the surface treatments was evaluated based on the extent of interfacial debonding at the aluminium-epoxy interface within the FMLs after low velocity impact events. Plastic deformation was also measured to indicate the load transferred by the adhesive interface and the adhesive strength of the surface treatments.

From the Single Leg Bend tests, the film adhesive in combination with a bead-blasted surface was identified as the combination providing superior adhesion, where the silane treatment was identified as the best chemical treatment. The combination of silane treatment and a film adhesive was recommended for the preparation of fibre metal laminates to be subjected to impact and blasted loading.

ACKNOWLEDGEMENTS

The author would like to express gratitude towards Prof G.S. Langdon and A/Prof C.J. von Klemperer for supervising this study and for providing the author with all the necessary support and guidance throughout the learning process.

The author would like to thank Dr R.A. Govender for his support and guidance with the testing and analysis done in this study.

The author hereby acknowledges the staff at the Centre for Materials Engineering, Ms P. Park-Ross, Ms L. Matthews and Dr S. George, for their assistance as well as Mr G. Newins and the staff at the Mechanical Engineering Department Workshop for all their workmanship

The author would like thank all the students and staff at BISRU for their ongoing support and good company.

The financial assistance of the National Research Foundation, UK Royal Society and the Blast Impact Survivability and Research Unit is hereby acknowledged.

PLAGIARISM DECLARATION:

I know that plagiarism is wrong. Plagiarism is to use another's work and pretend that it is one's own. I have used the convention for the citation and referencing. Each significant contribution to, and quotation in, this report from works of other people has been attributed, and has been cited and referenced.

This report is my own work. I have not allowed, and will not allow anyone to copy my work with the intention of passing it off as his or her own work.

Talita van Tonder

TABLE OF CONTENTS

LIST OF FIGURES

LIST OF TABLES

NOMENCLATURE

a	Crack Length
b	Specimen Width
c_{ext}	Crack Extension
d	Characteristic Scale Length
h	Specimen Thickness
C	Compliance
CGR	Crack Growth Rate
E	Impact Energy
F_{CI}	Force at Crack Initiation
F_{max}	Maximum Force
G_{CI}	Energy Release Rate at Crack Initiation
$G_{I\text{-}II}$	Energy Release Rate
G_{SP}	Energy Release Rate at Stable Crack Propagation
L	Support Span
P	Force
R_a	Arithmetic Average of Profile Deviation from a Centre Line
R_q	Root Mean Squared Deviation from the Centre Line
R_t	Maximum Height of Profile
R_z	Average Distance Between Lowest Valley and Highest Peak
T_g	Glass Temperature
T_m	Melting Temperature
δ	Non-dimensional Deflection
λ	Scaling Factor
σ	Stress
χ	Non–dimensional Energy

ADCB	Asymmetric Double Cantilever Bend (test)
ASTM	American Society for Testing and Materials
ATR	Attenuated Total Reflectance (spectroscopy)

BAE	British Aerospace
BISRU	Blast Impact Survivability Research Unit
BSAA	Boric–Sulphuric Acid Anodising
CAA	Chromic Acid Anodising
CAE	Chromic Acid Etching
CAI	Compression After Impact
CF	Carbon Fibre
DCB	Double Cantilever Beam
DDS	4,4’-diaminodiphenylsulfone
DGEBA	Diglycidyl ether of bisphenol A
EDX	Energy Dispersive X-ray spectrometry
ENF	End Notch Flexure
FML	Fibre Metal Laminate
FPL	Forest Product Laboratory (etch)
GF	Glass Fibre
GFPP	Glass Fibre Polypropylene
GFRP	Glass Fibre Reinforced Polymer
GPS	Glycidyloxy Propyl (trimethoxySilane)
IUPAC	International Union of Pure and Applied Chemistry
NDE	Non-Dimensional Energy
PAA	Phosphoric Acid Anodising
PEEK	Polyether etherketone
PEK	Polyetherketone
RDCB	Rigid Double Cantilever Bend (test)
SAA	Sulphuric Acid Anodising
SCRIMP	Seeman Composites Resin Infusion Moulding Process
SEM	Scanning Electron Microscopy
SLB	Single Leg Bend (tests)
TPB	Three Point Bend (tests)
UD	Unidirectional
UTS	Ultimate Tensile Strength
VARTM	Vacuum Assisted Resin Transfer Moulding

CHAPTER 1: INTRODUCTION

1.1. BACKGROUND

The escalating threat of terrorism in society and in aviation has initiated research into the blast resistance properties of aircraft materials as the detonation of explosives onboard an aircraft has catastrophic consequences. The Lockerbie air disaster in 1988 was the largest terror-related aircraft bombing with 270 fatalities [1]. Explosives that detonated in the cargo hold tore through the aeroplane skins and resulted in the Pan Am flight crashing in the town of Lockerbie [2].

Aircraft construction materials can include aluminium alloys, fibre reinforced polymers, honeycomb structures and fibre metal laminates. Fibre metal laminates (FMLs) are hybrid materials typically consisting of aluminium and glass fibre reinforced polymer layers. Research published by Fleischer et al [3] claimed that a cargo hold prototype manufactured from the fibre metal laminate GLARE was able to withstand a blast equivalent to that of the Lockerbie air disaster. This claim initiated research into the blast resistant properties of GLARE, which revealed that the blast resistance of GLARE competes with that of mild steel [4]. Studies comparing the impact resistance of woven composites to that of unidirectional composites found the response of the woven composites to be superior [5, 6]. Blast tests performed on woven thermoplastic FMLs have exhibited a similar blast response to that of the impact tested specimens whereby the woven FMLs performed better than their unidirectional counterparts [7]. This revealed the potential to develop a woven GLARE variant that could have an improved blast resistance over the existing variants.

GLARE is manufactured exclusively for Airbus and attempts at manufacturing thermoset FMLs with a similar composition to GLARE at the Blast Impact Survivability Research Unit (BISRU) laboratory has been unsuccessful prior to this study. Severe debonding between the aluminium and the glass fibre reinforced polymer (GFRP) laminate has hindered investigations into the FMLs' blast response as the debonding resulted in premature loss of structural integrity. The cause of the debonding was identified as weak adhesion between the aluminium and the epoxy resin, which was either a result of the resin being inadequate or the surface treatment not modifying the surface optimally for bonding. This study therefore investigated the techniques used to modify the aluminium surface as well as the materials and techniques used to manufacture fibre metal laminates.

1.2. RESEARCH OBJECTIVES

The purpose of this study was to work towards manufacturing thermoset FMLs with adequate adhesion at the metal-GFRP interface such that the interface did not debond prematurely during dynamic loading such as impact or blast loading. The study focused on aluminium surface treatments to modify the surface such that adequate structural bonds could be formed between the aluminium and the GFRP laminates.

1.3. OUTLINE

Chapter 2 presents a summary of published research that is relevant to this study. The constituents, compilation and manufacturing techniques of composites, fibre metal laminates and GLARE were reviewed. The mechanisms of structural adhesion were investigated and the surface preparation techniques used to pre-treat aluminium in the manufacturing of FMLs were reviewed. The methodology used to test the adhesive ability of interfaces was reviewed. The impact and blast response of FMLs were briefly discussed.

Chapter 3 describes the surface preparation techniques that were employed in this study to enhance the adhesion of the metal to the GFRP. The techniques employed to manufacture the different testing specimens were also described. Selected specimens were investigated to establish the effect of their surface treatments on their surface topography. The different composite manufacturing techniques were tested to determine which technique produced GFRPs with the best fibre to resin ratio.

Chapter 4 reports the adhesive strengths of the different surface treatment techniques obtained from quasi-static testing. Single Leg Bend tests were used to determine the fracture toughness of adhesive interface prepared with various chemical surface treatments, resins and film adhesives.

The surface treatments were compared and promising surface treatments were selected to be compared under dynamic loading conditions.

Chapter 5 reports the performance of various surface treatments under impact loading. FMLs subjected to the same incident impact energies were compared. The performance of the surface treatments were evaluated based on the degree on interfacial debonding, the overall internal damage and the plastic deformation.

The results from Chapters 3, 4 and 5 were discussed separately in the respective chapters and were analysed with reference to results obtained in literature. The efficacy and performance of the surface treatments and manufacturing methods under quasi-static and impact loading were discussed.

Chapter 6 summarises the findings of this study and recommends modifications for future studies.

CHAPTER 2: LITERATURE REVIEW

2.1. COMPOSITES

Composites are generally classified by the material that constitutes the continuous phase such as cement, ceramics, metals or polymers [8]. The International Union of Pure and Applied Chemistry (IUPAC) defines composites as “multi-component materials comprising multiple, different (non-gaseous) phase domains in which at least one type of phase domain is a continuous phase” [9]. Composites are usually high performance materials with very high strength to weight ratios, high durability, high resistance to harsh environments and great design flexibility [8]. Polymer composite structures are of interest in this study.

2.1.1. POLYMER MATRIX MATERIALS

The materials that constitute the continuous phase in composites are referred to as matrix materials [9]. Matrix materials serve as binding materials which transfer and distribute stresses imparted on composite structures to the reinforcement materials [8, 10]. The load transfer from the matrix to the reinforcement is facilitated by good interaction or adhesion between the matrix and the reinforcing material [11]. This adhesion is optimised by complete contact or surface wetting by the matrix material for both of which low viscosities are required [12]. Low viscosities are obtained by heating thermoplastic polymers above their melting temperatures, or are inherent to uncured state of thermoset polymers which harden or cure upon heating [13].

THERMOPLASTIC RESINS

Thermoplastic resins are generally classified by their ability to melt upon heating, where the polymer changes from a solid to a viscous state [14]. Thermoplastic resin molecules are long linear or branched molecules that are either entangled in an amorphous phase or crystallized in a crystal lamellar structure [13]. The melting temperature, denoted T_m, is the temperature above which the lamellar crystal configuration in of the polymer molecules is disrupted and where the crystallized molecules become mobile. The melting temperature is determined by the chemical composition, molecular mass and degree of crystallinity of the resin [15]. The glass transition temperature, denoted T_g, is the temperature above which the polymers in the amorphous phase become mobile and can diffuse into free space [13]. Above this temperature resin flexibility and elasticity increase, but the resin still retains its geometric structure [13].

Thermoplastic resin characteristics such as flexibility and toughness make them suitable for applications that require energy absorption. Polyether etherketone (PEEK), Polyetherketone (PEK), and Polyimides are high-performance thermoplastics used in aerospace applications [11]. The fabrication of thermoplastics composites are, however, very costly due to elevated temperature processes and are only used in niche areas [11, 12]. Thermoplastics are not suitable for use in aeroplane skins due to poor fatigue and creep properties, poor compression properties and the difficulty in manufacturing [16], and are not considered further herein.

THERMOSET RESINS

Thermosets are characterized by a curing process which is an irreversible chemical reaction that causes a low viscosity resin to solidify [14]. The solidification or curing reaction either occurs upon heating, the addition of curing agents such as co-reagents (for example amines, anhydrides, carboxylic acids), basic catalysts (such as tertiary amines) [12], or cross-linking agents or catalysts [10]. Thermoset resins improve the mechanical properties of composites through their highly rigid inherent three-dimensional network structure [15, 17]. The network structure is obtained as a result of monomer molecules with three or more functional groups reacting with each other or with bi-functional cross-linking molecules [13]. The properties of the cured resin are determined by the density of cross-links within the cured network which in turn is dependent on the size and structure of the resin molecules and curing reagents [15, 17].

Unlike thermoplastics, thermosets do not melt and this improves the thermal stability of the composites once cured [17]. Thermoset resins have the advantage that their monomers are usually in liquid form; therefore the resin can flow and wet the reinforcement adequately before the curing process begins [10, 12]. Thermosets are widely used in the composite industry due to their availability, ease of processing and low material and equipment cost [12]. The focus of the following discussion will be on epoxy resin as it is the thermoset resin of choice for this study.

Epoxy resins are used in high performance engineering composites that require their premium mechanical properties and where the cost is justified [18]. Epoxy resins have excellent chemical and environmental resistivity, good mechanical properties and electrical insulating properties [18]. Epoxies burn slowly and have a maximum service temperature of 270°C [18]. Their excellent adhesion properties, especially to metal surfaces [18], make epoxies of particular interest in this study.

The terminal epoxides seen in Figure 2.1.1 (a) and (b) are the distinctive functional groups of epoxy resins. These functional groups react in step growth or poly-addition cross-linking reactions by the addition of curing reagents or catalyzed homopolymerization [19, 20]. The curing agents or co-reactants are compounds that contain active hydrogen such as polyamines, polyacids, polymercaptans, polyphenols, etc [19]. Figure 2.1.1(c) and (d) are carboxylic acid anhydride and diamine hardeners respectively [20]. Homopolymerization is catalyzed by the presence of a Lewis acid or base [20]. The variety of curing mechanisms and curing reagents make epoxies very versatile resins [19]. The curing mechanisms do not produce any by-products therefore epoxies exhibit low cure shrinkage [18].

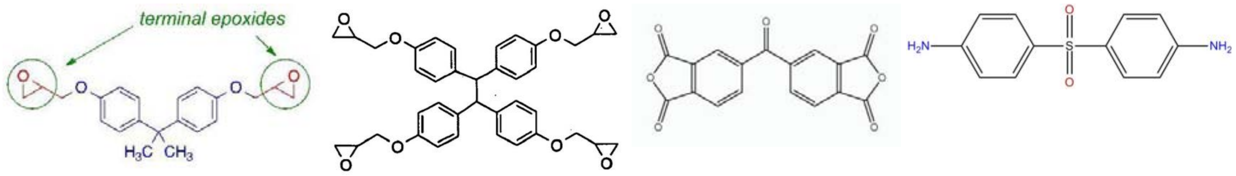

(a) (b) (c) (d)

Figure 2.1.1 Epoxy monomer molecules (a) Diglycidyl ether of bisphenol A (DGEBA) [21]and (b) Tetraglycidyl ether of tetraphenol ethane [22] and curing agents (c) 3,3’,4,4’-Benzophenonetetracarboxylic dianhydride (BTDS) [23] and (d) 4,4’-diaminodiphenylsulfone (DDS) [24]

2.1.2. REINFORCEMENT MATERIALS

Reinforcement materials are distributed within the matrix materials of composites in order to enhance the performance of the matrix material [12]. The reinforcement may be metallic, ceramic or polymeric and are classified according to the reinforcement shape, aspect ratio(s), geometric arrangement and concentration [25].

PARTICULATE REINFORCED POLYMERS

Particulate reinforcement, often termed fillers, are non-fibrous, nominally solid or hollow spheres, flakes, granules or powder [12]. Fillers are added to resins to improve properties such as impact and abrasion resistance, compressive strength and thermal stability [18]. Fillers added to thermosets can reduce shrinking during cure and increase the bulk therefore reducing polymer cost [18]. Particulate systems are predominantly isotropic in physical and mechanical behaviour [25].

FIBRE REINFORCED POLYMERS

Fibre-reinforced polymers (FRPs) are materials that consist of fibres embedded in a polymer matrix [12, 26]. The fibre reinforcement could be available in chopped strand mat, unidirectional (UD) or woven fibre arrangements [26]. Chopped strand mat are used for lower strength applications and will not be discussed here. Continuous fibre reinforcement such as woven or UD fabrics offers significant improvement in stiffness and strength, especially in the direction parallel to the fibre axis [25]. The resulting strength of FRPs and their characteristic light weight structure make them suitable replacements for metals and alloys in the aerospace, marine and automotive industries [11].

The strength of a FRP depends on the strength of the reinforcing fibre and the volume fraction of fibres in the matrix according to the rule of mixtures. The fibre volume fraction has a theoretical limit of 90.7% assuming hexagonal close packing [11], but in practice only 68% fibre volume fraction can be achieved as the individual fibres need to be completely isolated by resin [11, 27]. The presence of voids, dry patches and fibre-fibre contacts weaken the composite [26]. The strength of FRPs also depends on the length and diameter of the fibres: longer lengths reduce the effect of the stresses created at the fibre ends [27] and smaller diameters increase the fibre/matrix interfacial area to fibre volume ratio, therefore improves load transfer for a given volume fraction of fibre [28]. The mechanical properties of continuous FRPs are anisotropic, assuming uniform and aligned packing [18] and therefore exhibit a loss of strength when loads are applied at an angle to the fibre axis as the strength then depends on the matrix and the fibre-matrix adhesion [27]. The arrangement of fibres within a FRP therefore has a significant effect on its mechanical properties [6].

CONTINUOUS FIBRE SYSTEMS:

The anisotropic nature of continuous fibre reinforcement can be compensated for when an FRP is subjected to multi-directional loading by using stacked angle-ply laminates or woven fibre fabrics [26]. Angle-ply laminates are constructed so that each ply is oriented at an angle at which a load will be applied [11]. The plies can be arranged symmetrically, asymmetrically or anti-symmetrically with respect to the middle ply [28]. A cross-ply laminate has a 0°/90° ply arrangement, where one ply has an orientation of 90° relative to another ply with a reference orientation, 0° [29]. A balanced cross-ply has an equivalent number of plies in each direction [26]. Advantages of cross-ply laminates are their high stiffness, tensile strength, good compressive properties, excellent in-plane shear resistance and conformability [6].

Woven fabrics are constructed from interlacing fibre yarns, orthogonal relative to each other [10]. The fibre fabrics have advantages such as ease of handling (especially for automation), thicker fibre forms, improved fibre fracture toughness, enhanced modulus in the transverse direction as well as the reduction of interlaminar surfaces by the integrated fibre arrangement [30]. The undulating shape of the yarns, however, results in limited conformability, poor in-plane shear resistance and reduced tensile and compressive properties [31]. Normal and shear strain concentrations occur at the interstices where the yarns interlace due to stress perturbations under uniaxial tension [32, 33].

GLASS FIBRE

Glass fibres are spun from molten silica (SiO_2) and are attenuated or drawn for increased strength [34]. The mechanical properties of the fibres are isotropic due to the three dimensional lattice network molecular structure which is a result of the introduction of additional elements into the melt [11]. S-glass is produced by adding Al_2O_3 and MgO to the silica melt producing a fibre with a higher fibre modulus and a ternary SiO_2-Al_2O_3-MgO eutectic structure [35, 36]. S-glass fibres are regarded as high performance fibres due to their higher tensile strength and stiffness [36]. The E-glass fibre is produced by adding an additional CaO and B_2O_2 to the ternary eutectic melt resulting in a quaternary eutectic structure with a lower fibre modulus [35].

E-glass fibres are low cost fibres used in sports equipment and automobile applications, whereas S-glass fibres are used in aerospace applications where it may be possible to justify a higher cost [11]. High performance carbon and aramid fibres have lower areal densities than glass and are comparable in price to S-glass, but have poorer adhesion to epoxy resin [37] and have high composite fabrication costs [11], due to their substantially higher cost compared to GF.

2.1.3. MANUFACTURING METHODS

The manufacturing techniques used to fabricate composites are as crucial in the final performance of the product as the selection of the constituent components. Wet lay-up, dry lay-up with resin transfer moulding and prepreg techniques were used for producing laminates in this study.

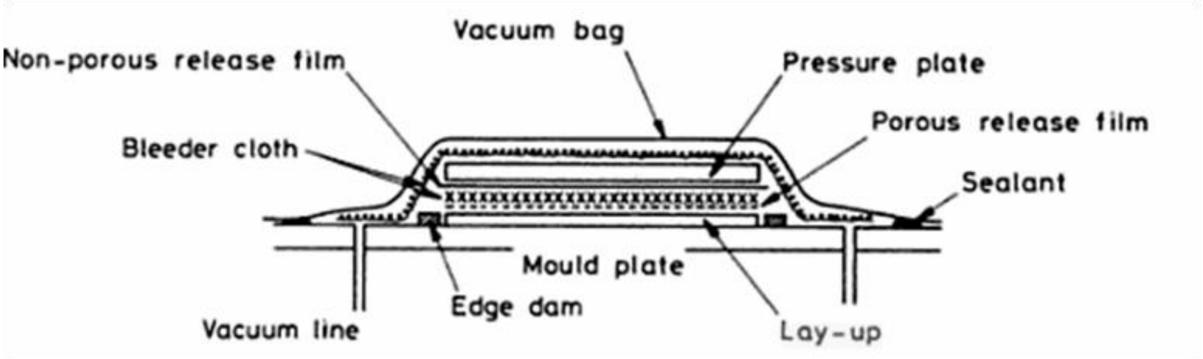

Figure 2.1.2: Wet lay-up manufacturing technique [38]

The wet lay-up technique is highly versatile as the complexity and size of the product is unrestricted [38]. The reinforcement is laid up into a desired form and consecutive layers are individually consolidated using a roller or brush. Excess resin can be drawn into the bleeder cloth by a vacuum if a vacuum bag on a pressure plate is used to compact the lay-up as shown in Figure 2.1.2. Composites produced by this method typically have higher resin content and relatively poor mechanical properties compared to other manufacturing techniques [38]. The low capital cost of this technique makes it suitable for applications with less stringent structural requirements [39].

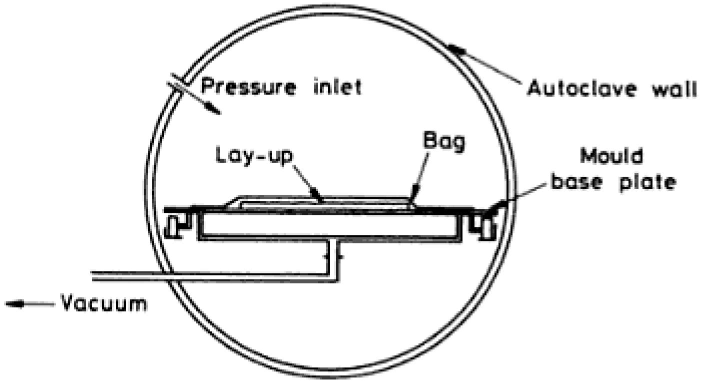

Figure 2.1.3: Autoclave manufacturing technique typically used for the lay-up of prepreg GFRPs [38]

Prepregs are sheets of reinforcement fibres pre-impregnated with partially cured resin. The viscous nature of the partially set thermoset resin holds the fibres in place improving ease of use, handleability and allows the sheets to be cut exactly to size which minimizes waste [38]. Prepregs are manufactured with a set fibre volume fraction and this allows for great consistency when producing composite structures [27]. The sheets are laid-up on a mould plate in the desired preform as seen in Figure 2.1.3 [38]. The prepreg resin is fully cured in an oven under vacuum pressure to remove any voids. This is an expensive process because of the increased skilled labour required and increased capital cost. It is only used when high quality and toughness are required in light weight applications [10]. A typical prepreg lay-up is shown in Figure 2.1.3.

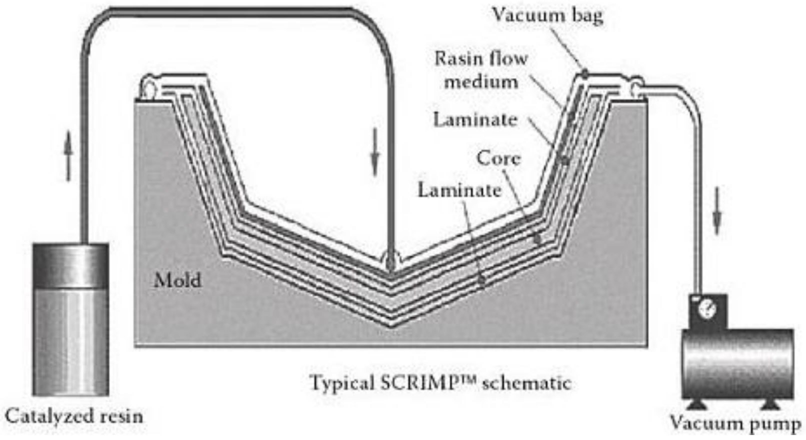

Figure 2.1.4: Mould section view for the Seeman Composites Resin Infusion Process [28]

Vacuum Assisted Resin Transfer Moulding is a technique where pre-mixed resin is drawn through a fabric prefrom in a closed mould connected to a vacuum pump as seen in Figure 2.1.4. [38]. Dry fabric preforms are laid-up in a desired configuration and are impregnated by an advancing resin front that displaces the air around the fibres [39]. Figure 2.1.4 depicts the Seeman Composites Resin Infusion Moulding Process (SCRIMP) which utilizes an open mould surface and a vacuum bag setup [28]. Low pressures are used which allows the use of a low stiffness shell mould (low cost and low weight alternatives to metallic matched moulds) [38]. Fast manufacturing cycle times, reduced volatile organic compounds and reduced scrap make this an attractive technique especially for larger structures [39].

2.2. FIBRE METAL LAMINATES: GLARE

Fibre Metal laminates (FMLs) are hybrid materials consisting of alternating layers of metal and fibre reinforced polymers as seen in Figure 2.2.1. GLARE (GLAss REinforced) is the only successful commercial FML product developed at the Delft University of Technology in the Netherlands by Vlot and Vogelesang [40, 41]. GLARE is suitable for use in aeroplane skins because it has a lower areal density than aluminium, but its initial development was driven by its excellent fatigue resistance, which was a welcome solution to the poor damage tolerance and stress fracturing of monolithic aluminium [40, 41]. Associated fuel cost reductions due to lower mass and maintenance savings also provided financial incentive for GLARE’s development [42].

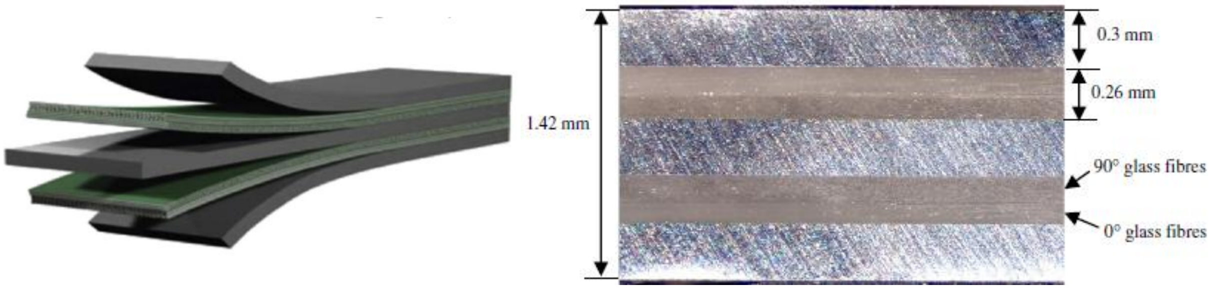

Figure 2.2.1: Images of the (a) alternating layers of GLARE [43] and the (b) cross-section of GLARE displaying the layup of the UD GFRPs [4]

GLARE is produced with aerospace grade aluminium alloy Al2024-T3 and 0°/90° cross-plied prepreg between the aluminium as seen in Figure 2.2 1(b). The prepreg consists of unidirectional S-glass fibres pre-impregnated with FM 94 epoxy adhesive [44]. The preparation of the aluminium for bonding includes mechanical abrasion, chromic acid etching, chromic acid anodizing and the BR-127 corrosion inhibiting bond primer [29]. Variations in the number, sequence and orientation of prepreg and aluminium layers produces different grades of GLARE products [29, 40, 41]. The notation 3/2 denotes three layers of aluminium and two GFRP layers in GLARE 3 which is used on the fuselage of the Airbus A380 aircraft [45]. GLARE 5 is a high impact variant used for the cargo floor of the Boeing 777 and has also been used for bulkheads [29, 37].

GLARE compensates for the poor fatigue resistance of aluminium and the poor impact properties of carbon FRPs [44]. Figure 2.2.2 (a) depicts the crack bridging phenomenon in GLARE whereby the high strength glass fibres bear the load across the crack opening [46]. The stress at the crack tip is reduced below a critical stress therefore reduces the rate at which cracks propagate [40].

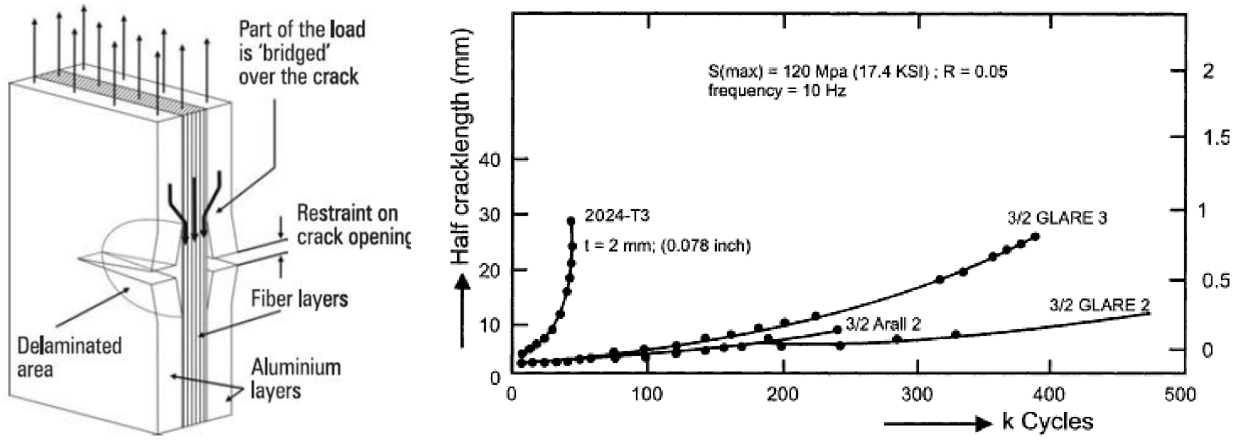

Figure 2.2.2: An illustration of the (a) fatigue crack phenomenon in GLARE [40] and the (b) fatigue crack resistance of GLARE variants compared to monolithic 2024-T3 aluminium [41].

Figure 2.2.2(b) shows the fatigue crack growth rates of two GLARE variants and ARALL (the predecessor of GLARE) in comparison to monolithic aluminium alloy 2024-T3 [41, 44]. GLARE's crack growth is relatively constant and 10-100 times slower than that of monolithic aluminium which greatly increases the service life of aircraft structures and reduces the maintenance costs and inspection times [41]. Circumferential and longitudinal lap joints are particularly prone to fatigue damage due to the stresses induced by riveting [42, 47]. The splice concept is a manufacturing technique developed to avoid the use of riveting sheets together by overlapping the aluminium layers in GLARE as shown in Figure 2.2.3 [40]. Internal doublers reinforce the splice or overlap and improve the residual strength of the material [42]. The splice technique allows the production of large GLARE sheets, limited only by the size of the autoclave reducing assembly and production costs [40, 42].

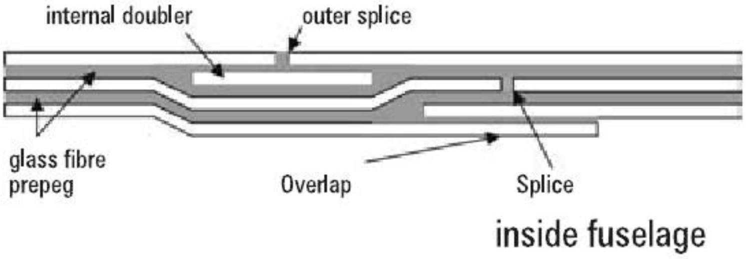

Figure 2.2.3 GLARE splice configuration [40]

GLARE is an attractive material for aircraft parts that are exposed to both high and low velocity impacts such as bird strikes, hail, engine or runway debris and ice due to its reported superior impact resistance and residual strength [41]. The improved impact properties can be attributed to the high strain rate phenomenon of the glass fibres [40]. GLARE displays similar plastic deformation to monolithic aluminium, but only at a higher impact velocity [41]. The visible external damage simplifies inspection and damage detection [42].

Higher impact, residual and blunt notch strengths are other properties that make GLARE desirable for use in aircraft structures [44]. Superior flame resistance is especially important as monolithic aluminium melts away in seconds, where GLARE maintains its structural integrity up to very high temperatures due to the glass fibres [40]. The developers also claim that the production process of GLARE has a significantly lower environmental impact [41].

2.3. STRUCTURAL ADHESIVE BONDING

The structural integrity and performance of composite materials are inherent properties of the adhesion between the matrix and its reinforcement [10]. Structural adhesion requires a bonded assembly to sustain a significant load throughout its service life [48]. This is especially important in aircraft structures where joints are exposed to static, cyclic and intermittent loads as well as harsh environmental conditions [48]. Adhesion mechanisms relevant to FMLs will be discussed further, followed by techniques used to enhance adhesion to aluminium in FMLs. Acid-base bonds, alcoholic bonds (between an opening epoxy ring and an aluminium oxide) and salt bonds (between the polymer adhesive and the metal surface) will not be discussed because these bonds dissolve in water [49] and are unsuitable for most applications.

2.3.1. MECHANISMS OF ADHESIVE BONDING

At a macroscopic level, adhesion is the bonding or joining of two similar or dissimilar materials [9]. Adhesion can be structural or non-structural, where structural adhesive bonds must be able to transfer stress across the interface without losing structural integrity [50]. Adhesion is not only a result of mechanical 'interlocking', but of molecular or atomic interactions at a microscopic level [49]. The precondition for adhesion is intimate molecular contact between two adherent surfaces, typically less than 1nm, in order for intermolecular or intramolecular bonds to form [49]. The different mechanisms of adhesion are classified according to the nature of these bonds.

POLARIZATION THEORY

The polarization theory describes the origin of physical bonds between two adherents that do not chemically interact [49]. The attractive intermolecular interaction exists between dipole moments on the surfaces of the adherent and adhesive [51]. Dipole moments are weakly polarized functional groups due to the non-uniform distribution of the electron density across a covalent bond [50]. The adhesion results from surfaces with opposite polarization attracting each other. These intermolecular forces are much weaker than chemical bonds, but the forces are cumulative and become significant over a large surface area [51]. The different types of intermolecular bonding that may result in adhesion, in order of decreasing strength, are electrostatic (ionic) forces (depicted in

Figure 2.3.1(a)), hydrogen bonding (depicted in Figure 2.3.1(b)) and Van Der Waals forces which include dipole-dipole interactions (depicted in Figure 2.3.1(c)) and dipole-induced dipole interactions [51].

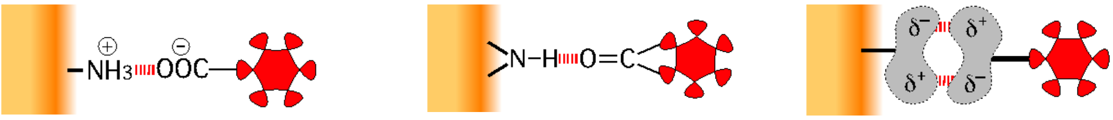

Figure 2.3.1: Illustrations of intermolecular bonds (a) electrostatic (ionic) forces, (b) Hydrogen bonds, and (c) dipole-dipole interactions [52]

DIFFUSION THEORY

Diffusion theory is attributed to the adhesion of polymers and polymer systems as a result of the entanglements of the long chain polymer molecules, where adhesion is achieved in the absence of chemical cross-links [49]. Above the glass transition temperature (T_g) the polymer molecules have sufficient kinetic energy to undergo chain rotations and long range molecular motion due to available free volume between molecular chains [53]. It is this molecular motion that results in the interdiffusion of polymer chains and subsequent entanglements which form an adhesive interface in the absence of chemical bonds, depicted in Figure 2.3.2 [49]. The strength of the bonding interface depends on the distance over which the molecules have interdiffused, the extent of the entanglements and the number of molecules over a given surface area [54, 55]. The requirement for molecular entanglement is the same for dissolution: attractive molecular forces between molecules or the molecules should have similar polarities [51].

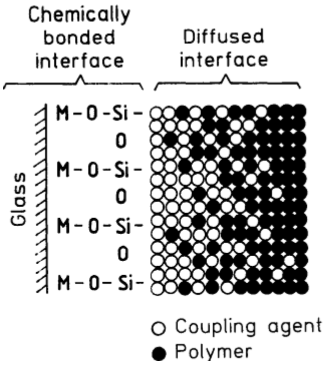

Figure 2.3.2: The diffuse molecular network of the silane coupling agent

CHEMICAL REACTIONS

The adhesion of two surfaces can be achieved by the formation of covalent chemical bonds as a result of chemical reactions at the adhesive interface [51]. The adhesion strength is directly dependent on the strength, type and number of bonds per unit area [54]. Chemical bonds are usually the strongest and most durable, but they require mutually reactive groups on either surface [50]. The durability of a bond is dependent on its ability to resist hydrolysis which is the cleavage of the covalent bond in the presence of water. [49]

MOLECULAR COMPLEXES

Molecular complexes form by the coordination of electron donating molecules or Lewis bases to the non-valence orbitals of Lewis acids, typically metal cations [56]. The electron donating molecules are called ligands and can have one (monodentate), two (bidentate) or multiple (multidentate) electron donating centres. A chelate complex is formed when a bidentate or multidentate ligand forms a ring structure around the cation centre [56]. The metal-ligand bonds of chelates form very strong and durable bonds at adhesion interfaces due to the ability to resistant hydrolysis [49]. The formation of the metal-ligand bonds is dependent on the nature of the metal ion and of the ligands, the solvent, the pH, and environmental factors, such as temperature and pressure [57]. The use of chelating agents as adhesion enhancers and corrosion inhibitors has been reported in literature [58, 59], but are beyond the scope of this project.

2.3.2. SURFACE TREATMENTS TO ENHANCE BONDING

Surface treatment techniques modify the surface structure and composition to maximize adhesion and bond durability [54]. Treatments prior to bonding should increase the number of chemically reactive groups per unit area and therefore increase the interactions at the bonding interface [50]. The prerequisites for adequate interaction between an adherent surface and an adhesive are that the adherent surfaces are to be free from contamination, wettable with either the primer or the adhesive, highly roughened and mechanically and hydrolytically stable [60]. The surface treatment techniques that will be discussed here are used for aluminium surfaces in aerospace applications, specifically for bonding to epoxy resins in FML structures.

STANDARD SURFACE PREPARATION TECHNIQUES

SURFACE DEGREASING

The most basic, yet crucial, surface preparation technique is degreasing which removes dust, grease, oil, rust, scale and miscellaneous dirt that would inhibit any interaction between the adhesive and the surface [49]. Organic solvents and water-miscible detergents are mostly used, while polar hydrocarbons such as methyl ethyl ketone (MEK), acetone and ethanol are the most effective [45]. Vapour degreasing is an effective process, but the volatile organic compounds produced are an environmental issue [51]. Ultrasonic baths are also used [50]. Surfaces are degreased by either immersion (solvent dip), spraying or solvent wipe, but in the case of solvent dip the disposal of large quantities of solvents is an environmental issue [61].

MECHANICAL SURFACE PREPARATION

The surface morphology is important as it influences the contact angle of the metal substrate and therefore its wettability [49]. Mechanical abrasion roughens the surface which increases the surface area and therefore the number of chemical interactions between the surface and adhesive [56]. Roughened substrates have been found to increase adhesion and significantly affect the joint behaviour [60], but mechanical abrasion does not provide adequate durability as a treatment alone [45].

Macro-roughness is achieved by mechanical abrasion that is either performed by grit-blasting or manually by sanding the surface with various grades of grit paper [56]. The adhesion obtained from grit-blasted surfaces is superior to manually abraded surfaces [62, 63]. Micro-roughness is produced by chemical processes that change the surface morphology and porosity at a microscopic and molecular level [64]. Both these type of processes will be described in the following sections.

Grit-blasting is a form of mechanical abrasion whereby abrasive particles are aimed at the adherent surface at high velocity [51]. The degree of abrasion is determined by the form and hardness of the grit, the pressure at which it is aimed at the surface and the distance the nozzle is held from the surface [49]. Grit-blasting induces physico-chemical changes to the adherent surface which enhances adhesive bonding [65]. There are dry and fluid blast processes, with dry blasting processes being most common [49]. Flywheel-blasting, vacuum-blasting and grit blasting are dry blasting processes whereby the abrasive blast media is propelled by compressed air or nitrogen [49]. Water-jet blasting, hot-water blasting and steam blasting are blast processes that use liquids to propel the blast media [49].

CHEMICAL SURFACE TREATMENTS

Chemical surface treatments modify the chemical nature of the surface in order to improve adhesion by increasing the number of chemical bonds that can form (in this case between the aluminium oxide on the adherent surface and the epoxy adhesive) [54].

ETCHING:

Etching is an intermediate production step between degreasing and electrochemical treatments [60]. The purpose of etching is to produce a chemically pure surface, to remove stubborn grease and contaminants and remove unstable aluminium hydroxides and oxides on the surface [29]. The removal of magnesium oxide is especially critical as it is associated with poor bonding [49].

The aluminium is submerged in a bath containing a strong acid or an alkali; the bath may also contain oxidizing agents [49]. The affectivity of the etchant is dependent on the time that the aluminium is submerged, the temperature of the etching bath, the concentration, the pH and the presence of an oxidizing agent [66].

The Forest Product Laboratory (FPL) etch and Chromic Acid Etch (CAE) are the two etching processes that are used for GLARE [45]. The FPL etchant comprises of chromic/sulphuric acid or dichromate/sulphuric acid solutions that produce thin residual oxides that thicken during rinsing and contribute to the adhesive ability of the surface [67]. An X-ray Photoelectron Spectroscopy (XPS) surface analysis has shown an alloy surface to contain only Aluminium, Oxygen, Copper, Carbon and Chromium after etching, which indicated that the magnesium oxide (MgO) and magnesium hydroxide ($Mg(OH)_2$) associated with poor bonding were removed from the surface [48, 68].

Both the FPL and CAE etching processes contain toxic hexavalent Chromium ions, therefore the P-2 Etch is a process that is replacing the FPL Etch as it contains less toxic ferric sulphate in a sulphuric acid solution [69]. The P-2 etch is similar in performance to FPL with regards to adhesion as seen in Figure 2.3.3, but has shown decreased durability and corrosion resistance [67]. The four bars in Figure 2.3.3 represent four different DGEBA epoxy (Figure 2.1.1(a)) resins systems of which the DDS hardener (Figure 2.1.1(d)) produced samples with a superior shear strength as determined by lap shear tests.

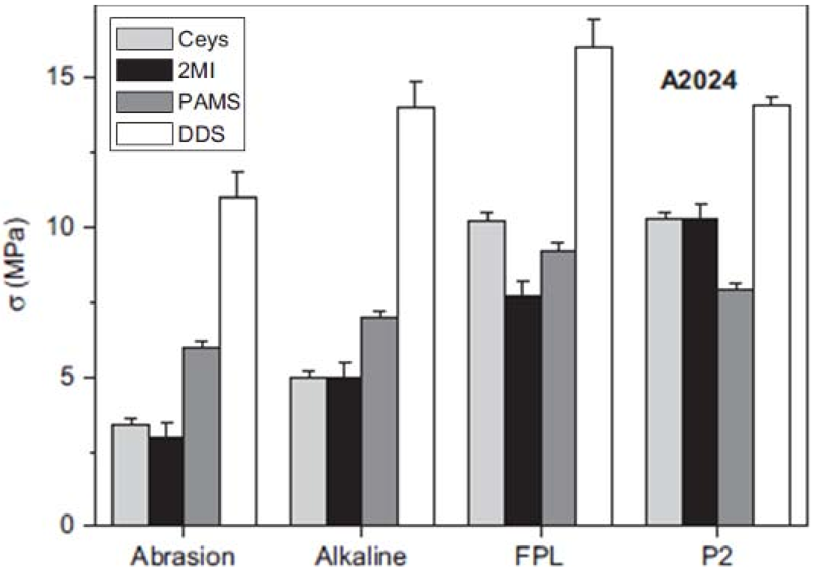

Ceys	Araldyte-Epoxy Rapid (commercial product form Ceys)
2MI	2-methylimidazol
PAMS	poly (3-aminopropylmethylsiloxane)
DDS	4,4-diaminediphenylsulfone

Figure 2.3.3: Lap shear test results of specimens tested with different surface treatements [67]

Alkaline etching is used to remove the existing surface oxide layer without generating new surface oxides [70]. The alumina or oxide layer is stable in a pH range of 4.5-8.5, therefore a strong alkali can also be used to dissolve the oxide layer, hence the alkaline etch [71]. Sodium hydroxide solutions with a pH of 10 are typically used [67].

ANODISING:

Anodising is the method of choice in the aerospace industry to promote adhesion due to its ability to improve corrosion resistance, hydration resistance as well as adhesion to organic polymer adhesives [72]. Anodising is a complex multistage process that is preceded by the roughening, degreasing, and deoxidising processes described prior to this section [48, 71]

Anodizing is an electrochemical treatment where the aluminium alloy is placed in a bath containing an acid electrolyte [71]. The aluminium (anode) is connected to an electrode and both are submerged in electrolyte to complete a circuit as seen in Figure 2.3.4(a) [73]. A current is applied which results in an oxidation reaction at the anodic aluminium surface [48, 74]. A thick aluminium oxide layer is produced on the surface as seen in Figure 2.3.4(b). This layer is highly adsorptive and therefore promotes bonding [63]. The thickness of the oxide depends on the applied voltage, the bath temperature, the electrolyte composition and the duration of the treatment [75]. The morphology of the oxide layer is an array of hexagonal cells forming a highly porous structure as shown in Figure 2.3.4(c) [48]. The pores are created by solvent action and the pore dimensions depend on the applied potential and electrolyte [76, 77].

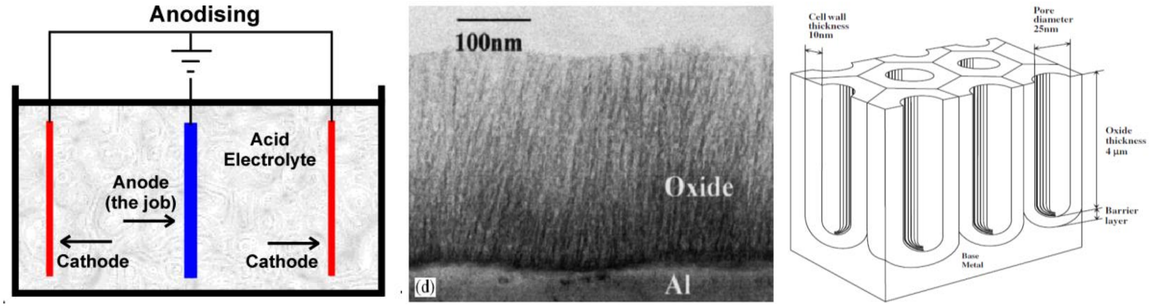

Figure 2.3.4: (a) The anodising bath setup [73], (b) a TEM image of the cross section of SAA-AC anodised oxide layer [63] and (c) the hexagonal cell morphology of the oxide layer [48]

The anodizing process is classified according to the electrolyte or acid used. Chromic acid anodizing (CAA) is the European method of choice and is preceded by a Chromic-sulphuric acid etch [75]. The CAA electrolyte consists of a chromic acid and potassium dichromate solution producing an oxide containing very little electrolyte anion and is almost purely aluminium oxide [78]. The applied voltage is increased step-wise over time which improves the adhesive ability of the surface [56, 79].

Phosphoric acid anodizing (PAA) is the preferred method in the USA [64]. PAA has a slower oxide growth rate which making it more environmentally stable and durable [56, 78]. The aluminium oxide also has whisker-like protrusions which contribute to adhesion [80]. PAA is preceded by either the FPL or P-2 etches [45, 70, 75] and utilizes a constant high voltage as opposed to a voltage gradient as used in CAA [56]. Sulphuric acid anodizing (SAA) and Boric-Sulphuric acid anodising (BSAA) are more economical alternatives to other commercial systems for products that have less stringent adhesive and mechanical requirements [81]. Figure 2.3.5 compares the lap shear strength of various non-chromate anodising techniques before and after both environmental and chemical exposure [75].

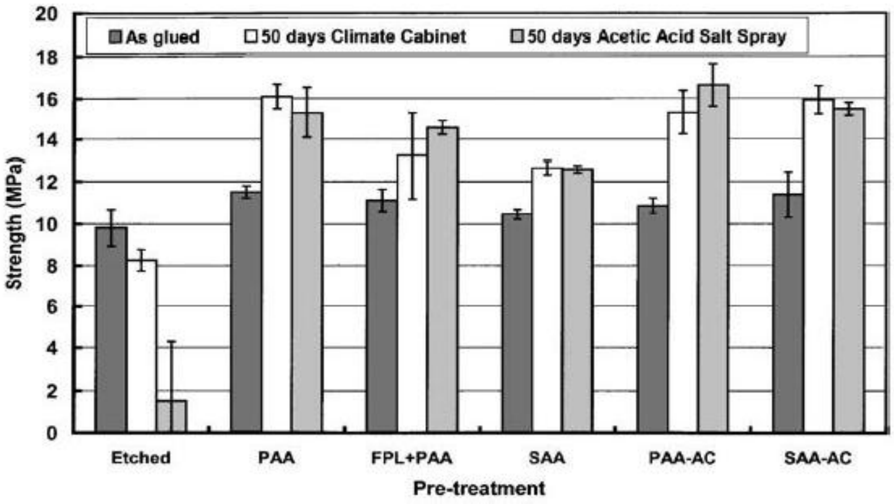

Figure 2.3.5: Lap shear test results comparing the adhesive strengths of various anodising techniques [75]

The use of hexavalent chromate ($Cr6^+$) has been banned in the European automobile industry since 1 July 2007 [82] because of its toxicity [48, 83, 84]. The European aviation industry is however still using $Cr6^+$ in their CAE and CAA processes [48]. The use of chromate can be circumvented by using the PAA process when it is preceded by the P-2 etch, but its durability is inferior to that of CAA as it is more prone to corrosion [45, 72]. PAA is also more time consuming to produce an oxide of similar thickness [75]. International legislation such as the Integrated Pollution Prevention and Control directive of the European Union is becoming stricter regarding the environmental impact of industrial processes [85, 86]. Industrial effluent must be treated on site to comply with the national or regional requirements before being discarded to avoid being penalised [85]. The use of more expensive environmentally friendly processes could be more economical than treating toxic effluent.

CONVERSION COATINGS AND PRIMERS

Conversion coatings are commercial practice for lower cost materials instead of anodizing [87], and the process is generally referred to as alodining [88]. Chromate conversion coatings provide good corrosion resistance through a reservoir of Cr6+ ions that contain available, unreacted ions to oxidize any bare aluminium to inhibit oxidation [89]; however their contribution to the adhesive ability of the adherent surface is generally inferior to that of anodizing. Figure 2.3.6 shows a comparison of bare aluminium, Cr^{6+}, Cr^{3+}, ZTF (Fluorotitanate/Zirconate) and Silane Sol-gel treated aluminium, all coated with an epoxy-polyester powder coating (PW) [83].

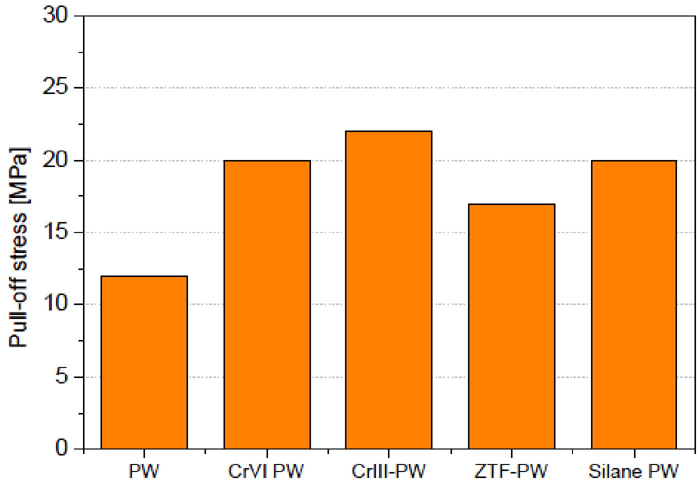

Figure 2.3.6: Comparison of the pull off tests of powder coatings (PW) with conversion coatings [83]

SILANE COUPLING AGENTS

Silane conversion coatings have been investigated as an environment friendly replacement for chromate treatments [64, 83]. Silane coupling agents are of particular interest as their performance has been compared to that of Phosphoric acid anodizing [90, 91] and for their short pre-treatment times [56, 87]. The silanes are attractive replacements because of their durability which is a concern with other non-chromate treatments. The silane molecules form stable covalent bonds as shown in Figure 2.3.7(b) with the aluminium oxide [92] as well as cross-linked diffuse hydrophobic networks that retard the diffusion of water to the oxide and the associated hydration which causes corrosion [93].

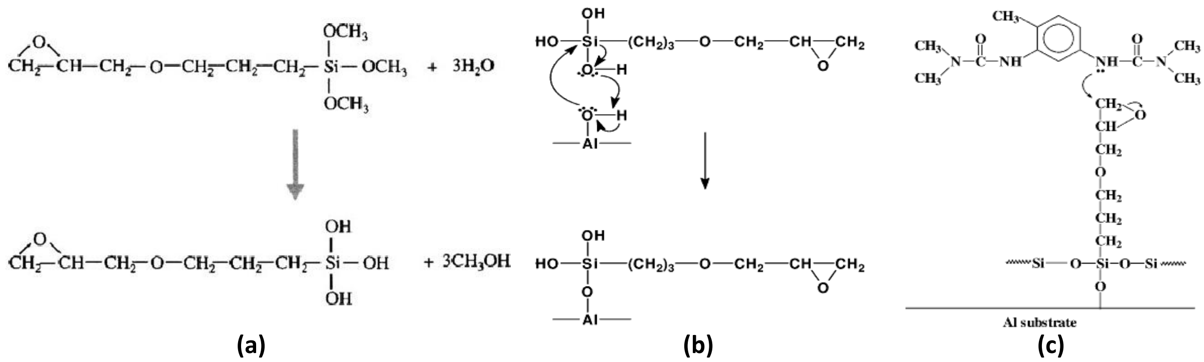

(a) **(b)** **(c)**

Figure 2.3.7: The (a) hydrolysis of silane groups to silanol functional groups, the (b) condensation reaction of silanol group with the aluminium hydroxide and the (c) ring opening reaction of the amine hardener with the epoxy group [94].

The silane molecules have functionalized epoxy groups that react with amine hardeners as seen in Figure 2.3.7 (c), to form part of the epoxy resin network, which contributes to their performance [94]. The silane films consist of either a silane network or a silane mono-layer which is a single molecule thick. Cross-linked polymer networks are formed and classified by the addition of cross-linker molecules to the silane molecules between the resin and the aluminium [63]. Organo-silane films are formed by molecules such as BTSE (1,2 Bis(triethoxysilyl) ethane) which forms covalent bonds with the silane molecules [83]. Sol-gel (solution-gelation) films are characterized by the formation of metal-oxo bonds, where metal ions (typically Zirconium) coordinate to the aluminium which in turn coordinates to the silane molecules [63, 86]. The metal ions also form cross-linker sites within the film itself.

This network forms an interphase region of intermediate modulus between the metal and polymer which facilitates stress transfer [48, 56, 92]. The ability of the silane coupling agent to absorb stress creates promise with respect to its performance in impact and blast tests.

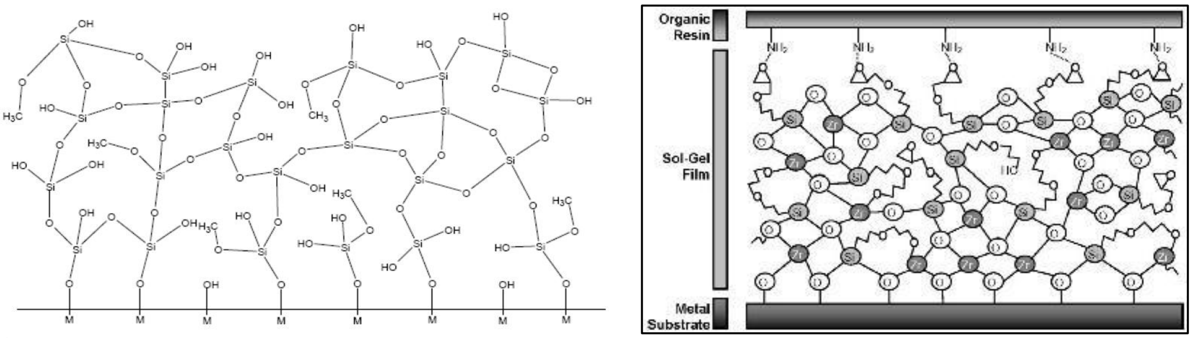

(a)

(b)

Figure 2.3.8: Illustrations of (a) the diffuse silane molecular network [83] and the (b) hybrid organic-inorganic sol-gel network [63].

Silane surface treatments can be used as standalone processes or as part of a complex pre-treatment sequence. The silane treatments have to be applied in an acidic medium in order for the methoxy groups to be hydrolyzed and the reactive silanol functional groups to be exposed [95, 88]. The silanol group in turn reacts with the aluminium surface (silane treatment) or the zirconium ion (sol-gel) in a condensation reaction where water is a by-product [64, 92, 96]. The epoxy group on the silane molecule covalently reacts with the amine hardener to form part of the epoxy resin network [96]. Factors affecting the epoxy-aluminium joint performance are the pH of the silane solution, the duration of the treatment and the solvent used for the deposition [83, 87].

The treatments are very short in duration, as the silane could be applied manually, by spraying the aluminium or by submerging it in a solution. Cathodic electro-deposition has also been reported [97]. The aluminium surface only has to be bead-blasted prior to treatment [83]; however it has been shown that bead-blasted and etched aluminium produces superior adhesion [87]. Commercial products such as Silquest A-187 [98] and the AC-130 surface pre-bond treatment [99] have been produced, the latter being a Boeing Company Licensed Product. Silane treatments have shown great potential, however one distinct drawback was their high cost compared to other conversion coatings [87].

FILM ADHESIVES:

Film adhesives have been used in the manufacture of aircraft structures in British Aerospace aircraft as well as Fokker aircraft [61]. The Redux 775 was the first film adhesive to be used in aircraft structural bonding in 1954 [100]. The benefits of film adhesives were the improved the ease of handling and improved bond-line thickness control [100].

The Redux (Research at Duxford) films were developed by Norman de Bruyne at the Cambridge Aeroplane Construction Company [101]. The Redux chemistry was based on phenol-formaldehyde resin with poly (vinyl formal) resin as reinforcing filler which provided the film with its inherent toughness and excellent environmental resistance [101]. Nitrile-phenolic and epoxy-based films were eventually developed for structural adhesion [101]. The toughened film systems have shown to be critical in the transfer of load from one adherent to another in primary aircraft structures [102]. The Cytec FM 73 and the 3M Scotch-Weld AF 163-2 epoxy film adhesives are currently used for structural adhesion in aircraft structures [61].

2.3.3. ADHESION TEST METHODOLOGY

The standard quasi-static testing procedures used in aerospace applications to determine the adhesive strength of interfaces have been wedge tests, end notch flexure (ENF), double cantilever beam (DCB) and single lap shear tests. The focus of this study was to determine the ability of the aluminium-epoxy interface to resist delamination for which the Single Leg Bend (SLB) tests were established to be the most suitable for measuring delamination in FMLs [103].

The fracture toughness and shear strengths obtained from standard tests were typically reported in $MPa.m^{½}$ and MPa therefore a direct comparison could not be made to the energy release rate (measured in $J.m^{-2}$) determined from the SLB tests without making assumptions with regards to the nature of the fracture and properties of the specimens [104]. The fracture toughness determined from various test methods was dependent on the G_I/G_{II} loading ratios and has shown very little consistency over the range of full opening to shear failure [105]. There are several prediction models that have been developed such as the energy release rate approach by Alderliesten [106, 107] and a toughness versus mode mix curve by Davidson et al [108]. The use of these models to predict the energy release rate is beyond the scope of the study, however it has been established that delamination growth under mixed mode loading is significantly higher than the pure mode II loaded delaminations [107]. Large differences in fracture toughness between test methods can therefore be ascribed to the mode ratio of the respective testing method. This was considered when comparing the results of this study to literature.

2.4. IMPACT RESISTANCE OF FMLS

In-plane low velocity impact testing is a good method to measure the performance of FMLs as there are substantial amounts of published research for comparison [5, 6, 107-109]. GLARE had a very high impact resistance and high resistance to cracking upon impact compared to monolithic aluminium which was attributed to the high strain-rate strengthening property of the glass fibres [40]. A comparison is shown in Figure 2.4.1 between the impact response of GLARE and monolithic aluminium alloy. The depth of the impact dent was a function of impact energy only and was approximately equal to that of Al 2024-T3 [109]. The visible dents made damage detection easier compared to composites which exhibited primarily fibre and matrix cracking and minimal plastic deformation [40, 109]. The internal damage within GLARE was however confined to a very small area surrounding the point of impact and the internal damage was always smaller than the visible plastic deformation which contributed to the ease of damage detection [46].

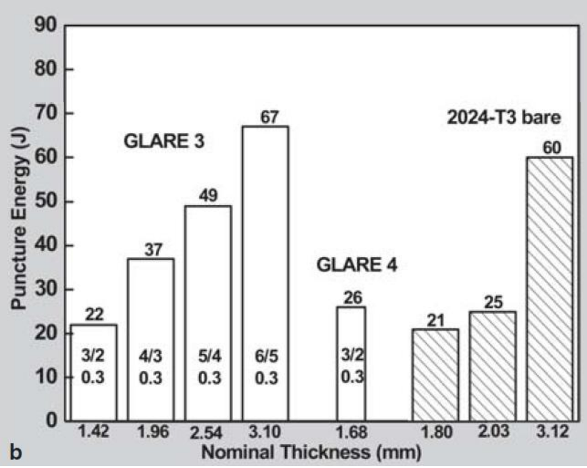

Figure 2.4.1: The low velocity impact response of GLARE variants compared to 2024-T3 aluminium [107]

FMLs that are subjected to low velocity impact generally exhibit four major stages of energy dissipation shown in Figure 2.4.2: (1) plastic deformation of the aluminium layers, (2) delamination, which may include matrix cracking, (3) matrix and fibre damage and then (4) puncture [110]. The response of GLARE to low velocity impact was described as “aluminium critical” because aluminium cracking occurred on the distal face of the FML before failure occurred in the fibres [109]. According to Vlot [109], limited or controlled delamination occurred at the interface to allow for stress redistribution from the cracked aluminium to the unbroken fibres. Cortés et al [111] have shown that interlaminar and interfacial delaminations were important mechanisms for absorbing impact energy, however, a lack of plastic deformation was indicative of a lower impact resistance as the plastic deformation was a primary contributing factor to the superior impact resistance of FMLs [112].

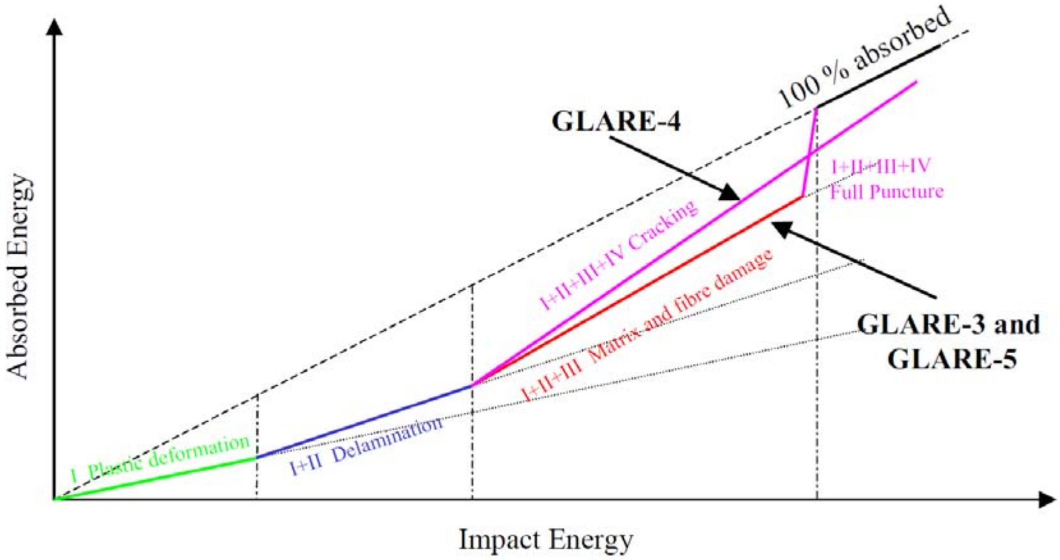

Figure 2.4.2: The four stages of impact damage progression in GLARE [109]

It could be deduced that a controlled amount of interfacial delamination allows for crack bridging, whereas excessive interfacial debonding reduces the amount of energy absorbed by plastic deformation, matrix cracking and fibre failure and therefore lowers the impact resistance of an FML. Reyes et al [113] showed that significant impact energies were absorbed by extensive plastic deformation of aluminium and composites and the localised micro-cracking of glass fibre polypropylene (GFPP) FMLs. Ardakani et al [114] showed that FMLs with better interfacial debonding transferred a higher force to the indentor, as the adhesive was critical in the transfer of load from one adherent to another [102].

2.5. BLAST RESISTANCE OF FMLS

The superior impact resistance of GLARE compared to monolithic aluminium was established for bird strike, engine and runway debris applications during the development of the GLARE product [41]. The Lockerbie air disaster sparked interest in the impact and blast resistance of aircraft materials when a bomb detonated in the cargo hold of the Pan Am flight 103, resulting in 270 fatalities [115].

In 1996, Fleisher et al [3] published a report that claimed that a luggage container made from GLARE was able to withstand a blast larger than that of the Lockerbie bomb explosion. The blast load and the structural response of a luggage container were modelled from which prototypes were developed and tested. Luggage containers were produced using several different materials, of which the GLARE container was the only one to remain intact. Unfortunately insufficient design and experimental details were reported for a detailed comparison of data.

Figure 2.5.1: Cargo hold prototypes made from GLARE, shown before and after blast loading [3].

2.5.1. BLAST RESPONSE OF GLARE

The potential of GLARE as a blast resistant material has initiated several studies with regards to its high velocity impact and blast resistance [4, 115- 117]. Langdon et al [4] investigated the response of GLARE 3 panels, a variant used typically in high impact regions of the fuselage, to blast loading. The damage exhibited by the GLARE panels resembled damage typically seen in monolithic metals as opposed to fibre reinforced composites. Close range testing resulted in perforation of the panels as well as petalling as seen in Figure 2.5.2. Panels that were exposed to blasts with a larger stand-off distance demonstrated plastic deformation shown in Figure 2.5.3, which was a typical structural response of monolithic metals and an atypical response for composites. The yield line formation and pulling in which was as a result of the boundary conditions or clamp frame was another typical metallic response. Transverse sectioning revealed fibre fracture and fibre pull-out which were failure modes associated with composite failure. Interfacial debonding only occurred at the boundary and between fibre layers, not at the aluminium/epoxy interface as shown in Figure 2.5.4(a). Low velocity impact tests performed on GLARE/hybrid materials did not reveal any delamination at the aluminium/epoxy interface, and all damage such as matrix cracking and fibre fracture was confined to the composite layers [116].

Figure 2.5.2: Petalling of a GLARE panel blasted from a close proximity [4]

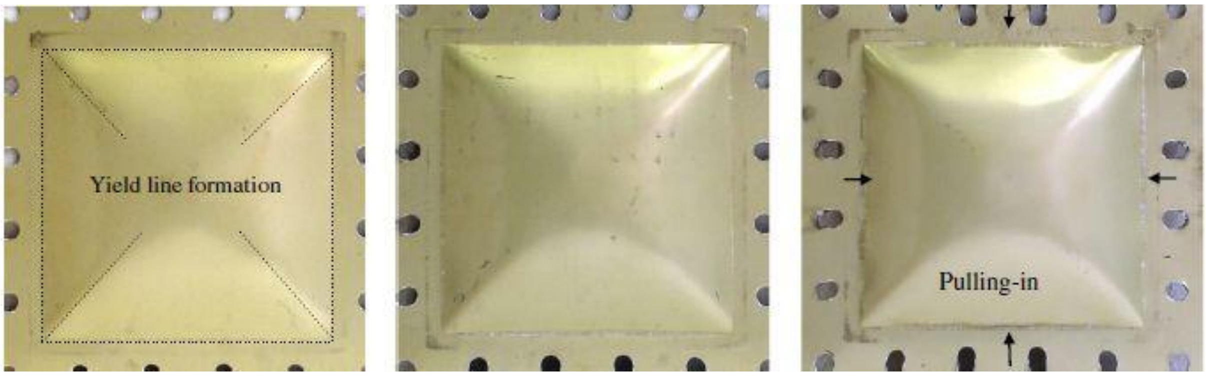

Figure 2.5.3: The plastic deformation of the distal face of GLARE panels blasted from a distance of 200mm [4]

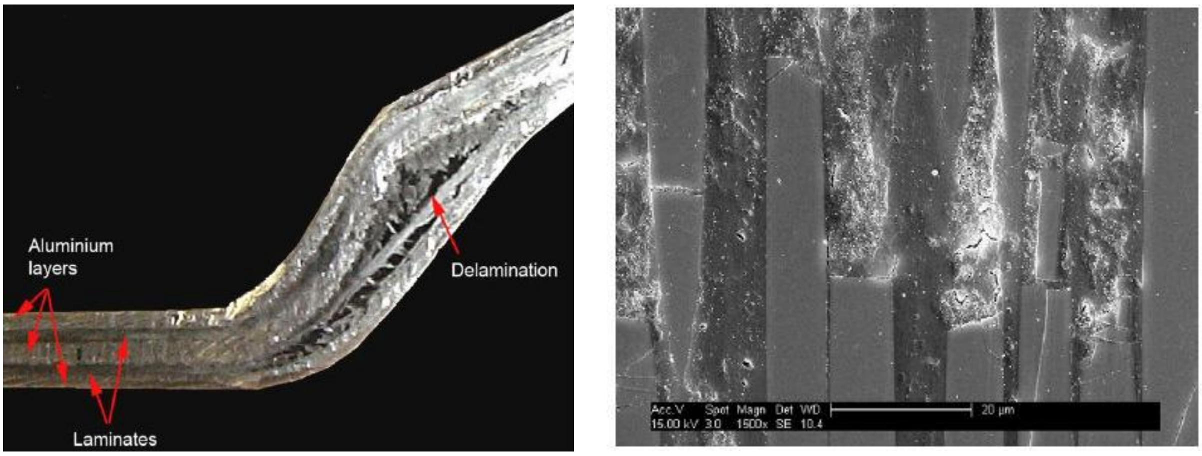

Figure 2.5.4: Images depicting the (a) fibre fracture matrix cracking and delamination at the clamping boundary of the panels [4] and the (b) fibre fracture and matrix cracking in the glass layers of the low velocity impact specimens [116].

Quadrangular plates were blasted by uniform loading using 3 to 14g of PE-4 explosive, at a stand-off distance of 200mm. The mid-point deflection was measured with each blast and was found to increase proportionally with increasing charge mass. The deflection to plate thickness ratio was plotted against the dimensionless impulse derived from the blast tests as seen in Figure 2.5.5. The blast response of mild steel plates was plotted on the same axes for comparison to GLARE. GLARE exhibited a lower displacement to thickness ratio for an equivalent impulse. GLARE could therefore be considered the only competitor for steel with regards to blast resistance in the case of uniform blast loading; however further testing is required to validate this statement [4].

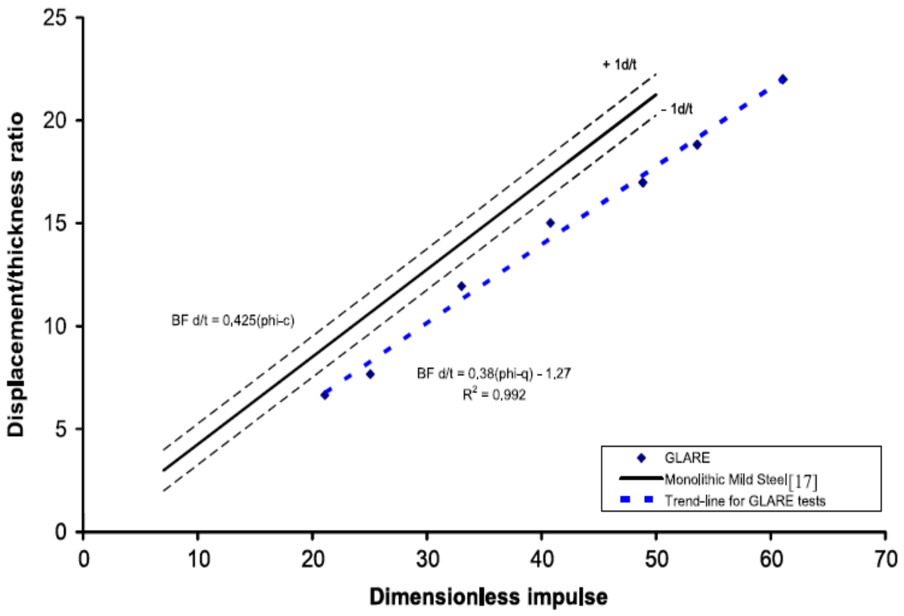

Figure 2.5.5: Graphs representing the experimental results of GLARE's blast resistance compared to monolithic mild steel [4]

2.5.2. BLAST RESPONSE OF WOVEN AND UNIDIRECTIONAL GLASS FIBRE

GLARE is manufactured using unidirectional prepreg layers with a 0°/90° or 0°/90°/90°/0° cross-ply lay-up to achieve homogeneous reinforcement. Several studies [5, 7, 6, 117, 112, 118] have shown that woven structures have mechanical benefits over UD cross-ply FRP’s with regards to impact and blast performance. This suggests that a GLARE variant with a woven fabric structure could have a superior blast resistance to that of the cross-ply lay-up.

Kim et al [5] investigated the impact and delamination behaviour of woven CFRP composites in comparison to UD laminates using low velocity impact tests. C-scan ultrasonic images were used to quantify the damage tolerance and delamination shown in Figure 2.5.6 (a) and (b). The damage in the warp and weft directions of the woven composites were similar as the orthogonal and interlinked yarns did not allow the cone shaped delamination zone seen in Figure 2.5.6(b), hence the star-shaped damage. The weave structure inherently limited the propagation of the in-ply cracks [119]. The cross-ply laminates showed slightly less damage on the proximal face, but the distal face delaminated readily as there was no restraint to this.

Thermoplastic FMLs shown in Figure 2.5.6(c) and (d) were exposed to air blasts by Langdon et al [7] and displayed similar damage behaviour as those tested at low velocities impact: the woven fabric FMLs exhibited a similar star or diamond shaped damage, where the cross-ply laminate did not exhibit a distinct pattern of damage.

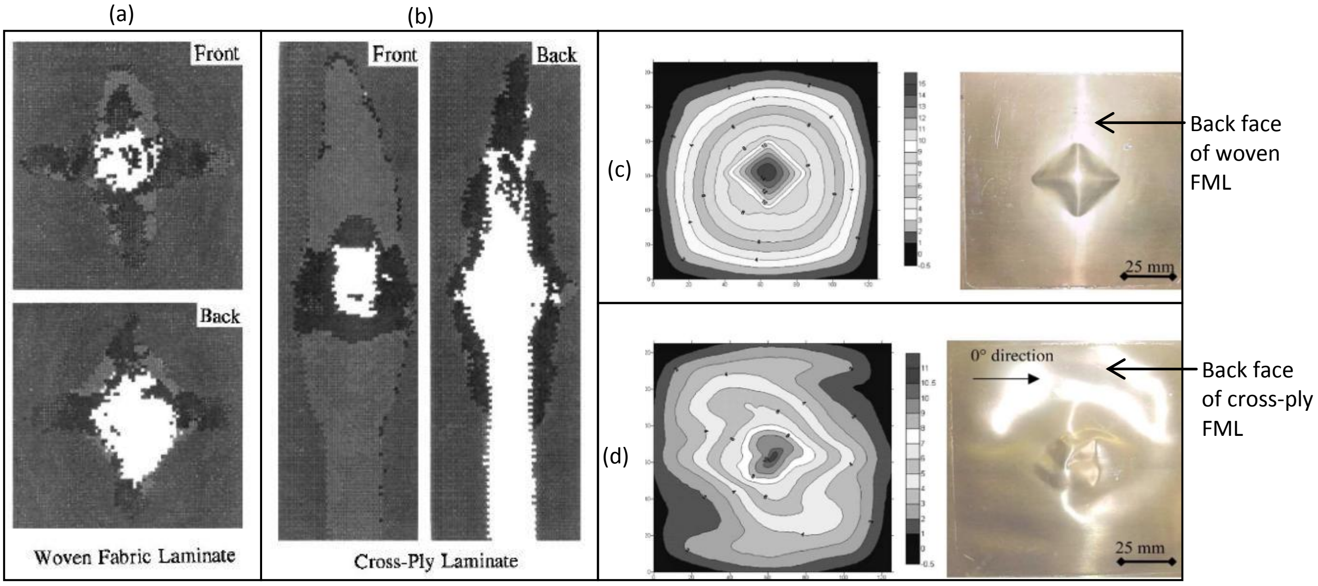

Figure 2.5.6: Response of (a) woven and (b) unidirectional composites to impact [5] and the response of (c) woven and (d) unidirectional FMLs to blast loading [7]

The interstices at the inflection of the warp and weft yarns and the regular undulating pattern of woven fabrics result in resin rich interlaminar areas. These resin rich areas, shown in Figure 2.5.7, are plastic yield zones which contribute to the delamination resistance of woven fabric laminates. It has been suggested that a large delamination or crack-tip deformation zone reduces the stress at the crack tip reducing the crack propagation [120]. Unidirectional fibres are straight, stiff and densely packed with a narrow bond-line thickness which reduces this plastic zone.

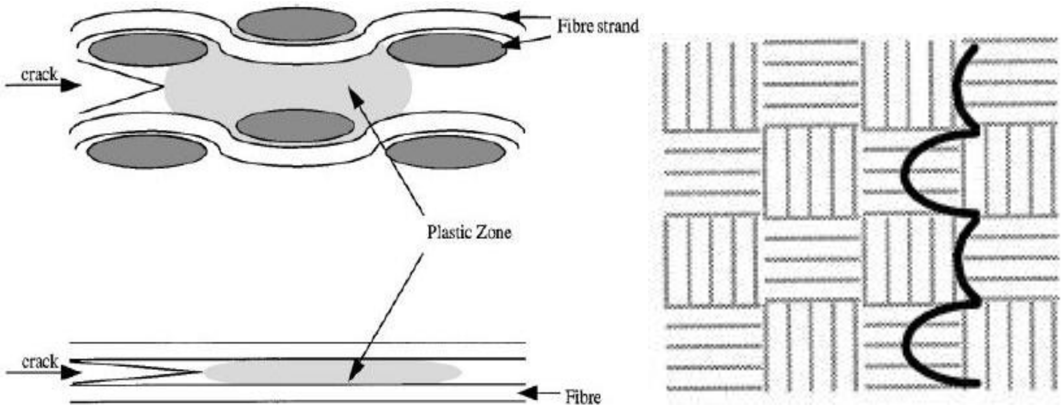

Figure 2.5.7: Woven glass fibre reinforced polymers and its (a) plastic zone [6] and (b) undulating weave [6]

The undulating pattern of the yarns increases the macroscopic roughness of the fabric surface which also improves bonding [118]. The yarn orientation also restricts the propagation of a crack when the fibre direction is perpendicular to that of the crack tip. The inherent roughness of the fabric, the plastic yield zones and crack bridging all have shown to contribute to a higher mode I interlaminar fracture toughness [6]. Woven fabrics also have a higher mode II interlaminar fracture toughness determined by the plasticity and fracture toughness of the matrix material and the fibre/matrix interfacial strength. Woven fabric laminates also have shown a higher Compression After Impact (CAI) strength as the CAI was dependent on the size of existing damage rather than the rate of interlaminar delamination [117]

CHAPTER 3: MANUFACTURING TECHNIQUES

This chapter describes the manufacturing methods used to produce all the specimens required for this study. The products were described and differences between them were clarified. The selection of aluminium surface preparation techniques were discussed and described individually. The manufacturing techniques and processes used to produce FML specimens for Single Leg Bend tests and impact tests were also included. The surface treated aluminium was inspected to establish whether the surface treatments were effective. Tests were performed to determine which manufacturing technique produced composites with the best fibre to resin ratio.

3.1. MATERIALS

3.1.1. GLASS FIBRE

Three varieties of E-glass fibre (GF) were used in this study: woven, unidirectional and Injectex. E-glass was used due to its availability and low cost. The woven GF fabric with an areal weight of 395g.m^{-2}, depicted in Figure 3.1.1(a), had a plain weave where the warp and weft could not be distinguished from each other. The unidirectional glass fibre had almost all its yarns running in one direction. In Figure 3.1.1(b) several isolated, thin, non-load bearing yarns were seen running in the weft direction which held the unidirectional yarns in place. The Injectex glass fibre fabric had a twill weave structure shown in Figure 3.1.1(c) and was characterized by weft yarns that were highly twisted to enhance resin flow in one direction, and are depicted in Figure 3.1.2. The configuration of the Injectex fabric was designed specifically for resin transfer by infusion.

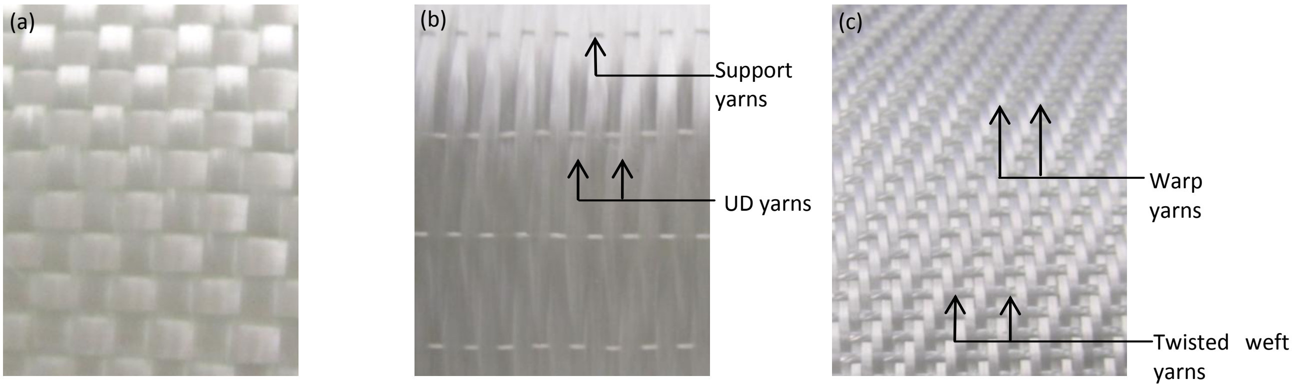

Figure 3.1.1: (a) Woven glass fibre, (b) Unidirectional and (c) Injectex glass fibre fabrics that were used to manufacture specimens.

Figure 3.1.2 Injectex twisted weft yarn

3.1.2. PREPREG

The Gurit SE 84 LV prepreg is a hot-melt epoxy prepreg with excellent mechanical properties and high compressive strength [121]. The glass fibre fabric had been pre-impregnated with SE 84 LV resin and had a resin content of 39% (±3%). The plain woven E-glass fibre fabric had an areal density of 295g.m^{-2}. The SE 84 LV prepreg roll was stored at -18°C. The SE 84 LV resin had a versatile curing temperature range between 80°C and 120°C, therefore the temperature profile depicted in Figure 3.1.3 was followed. A lower maximum temperature was selected to minimize the thermal expansion of the aluminium.

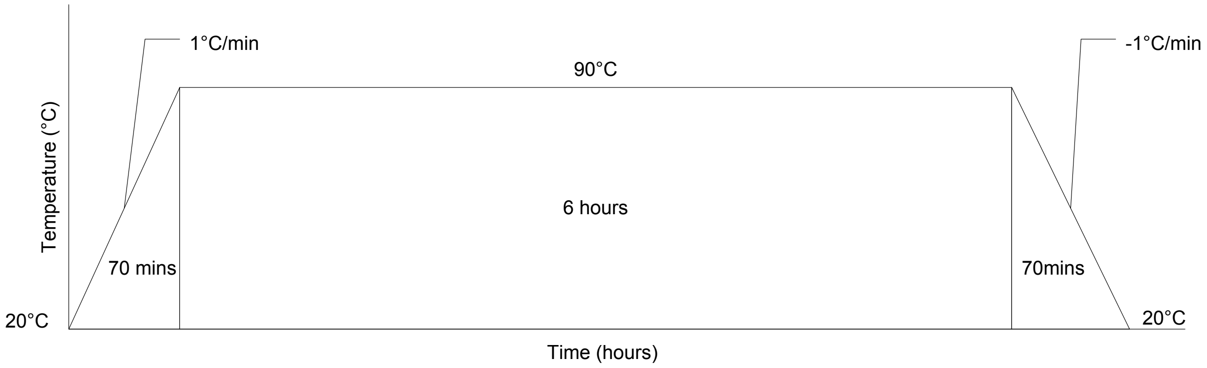

Figure 3.1.3 Curing cycle of SE 84 LV resin [121]

3.1.3. PRIME 20 LV RESIN

Prime 20 LV was an epoxy resin with a very low viscosity which made it ideal for resin transfer by infusion [122]. Prime 20 LV epoxy resin was used in conjunction with a slow, low viscosity (LV) hardener, which ensured that the curing reaction was slow enough allowing the glass fibre to be fully wet-out before the viscosity increased as the curing reaction occurred.

The resin and the hardener were mixed in a 100:26 ratio by weight. Post infusion or wet lay-up, the resin was allowed to cure for 24 hours at room temperature in the mould after which the specimen was post-cured in an oven. The temperature profile of the post-curing cycle was represented in Figure 3.1.4.

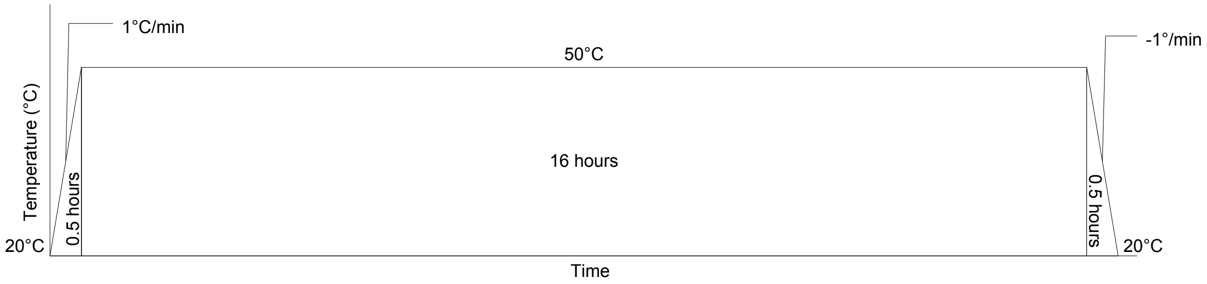

Figure 3.1.4 Graph illustrating the post-curing cycle of Prime 20 LV resin [122]

3.1.4. REDUX 609 FILM ADHESIVE

The Redux 609 was a modified epoxy film adhesive designed specifically for Aluminium bonding and sandwich structures [123]. The film adhesive had an areal density of 300g.m^{-2}. The film was supported by a cotton scrim for easy handling and a consistent glue-line thickness. Similar to a prepreg material, a protective silicon coated backing paper and a polyethylene release paper protected the film during storage, as depicted in Figure 3.1.5. The film was cut to shape prior to the removal of the protective coverings and required very little handling. The film was tacky at room temperature in its uncured state and was cured according to the temperature program represented in Figure 3.1.6. The film was stored at -18°C.

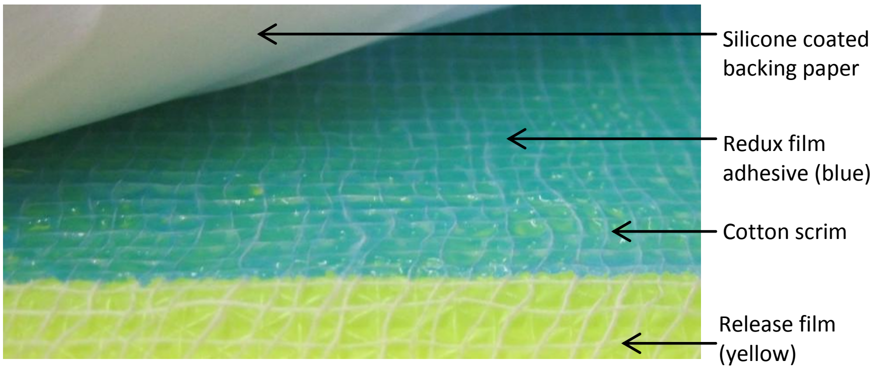

Figure 3.1.5: Photograph of uncured Redux 609 with protective backing paper and release film

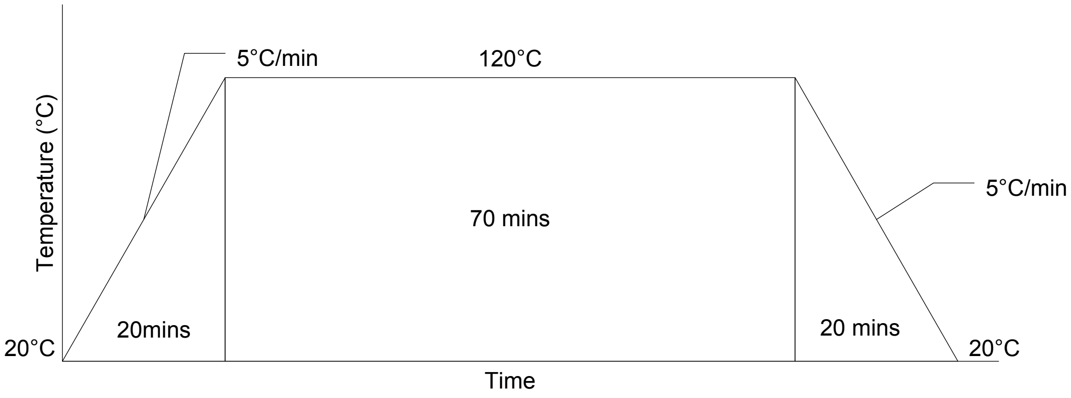

Figure 3.1.6: Curing cycle of Redux 609 film adhesive

3.1.5. ALUMINIUM ALLOY

Aluminium alloys were used to produce both the Single Leg Bend (SLB) test specimens and FMLs for impact loading. Aluminium alloy 1005 was used to produce the SLB specimens due to its low cost and availability. The alloy sheets were 2mm thick and laser cut in to 110mm x 500mm sheets. Aluminium alloy 2024-T3 was purchased from AirCraftMaterialsUK Ltd to produce the fibre metal laminates. The sheets were 0.46mm thick and were laser cut in to 300mm x 300mm sheets. The alloy composition was tested by Kaiser Aluminium in the United Kingdom according to the ASTM E1251 standard. The results from the 2024-T3 alloy composition determination is represented in Table 2.1.

Table 3.1.1: Elemental composition of 2024-T3 Aluminium alloy as determined by Kaiser Aluminium

Element	**Al**	**Si**	**Fe**	**Cu**	**Mn**	**Mg**	**Cr**	**Zn**	**Ti**	**V**	**Zr**	**Other**
Percentage weight occurrence	93.18	0.09	0.20	4.5	0.55	1.3	0.01	0.12	0.01	0.01	0.01	0.03

3.2. ALUMINIUM SURFACE PREPARATION TECHNIQUES

3.2.1. DEGREASING

The aluminium surface was degreased prior to each surface technique and repeated before the application of resin for bonding. The adherent surfaces were degreased by the solvent wipe method. Acetone was the solvent used and lint-free tissue paper was the medium. The tissue paper was doused with acetone and the surface was wiped until clean. The adherent surface was regarded clean when there were no wipe marks and clean tissue paper did not show any dirt after the surface was wiped.

3.2.2. GRIT-BLASTING

Grit-blasting was performed to achieve a macro-roughened aluminium surface and all sheets were grit-blasted until they had a nominally uniform roughness. The nozzle was held at a constant distance of 50mm from the aluminium surface. The duration of the bead-blasting increased with the size of the aluminium sheets, but remained constant for a certain size. The grit-blasting was performed using a bead-blaster which was connected to a high pressure air line with a pressure of 7 bar. The beads used were 100-500µm silicon dioxide particles. The obtained surface roughness and surface profiles are shown in section 3.4.

3.2.3. ETCHING AND ANODIZING

The etching and anodizing processes were outsourced due to the difficulty in producing a high enough current necessary to produce a thick oxide layer due to the large area of the aluminium sheets [124]. There were also health and safety concerns about using and storing the very strong acids and bases required.

The etching and anodizing was outsourced to Cape Anodizing Pty Ltd. The etching was performed in an alkaline bath. The anodising bath contained sulphuric acid rather than chromic acid. The company was unwilling to disclose any more details regarding their processes. The surface roughness and surface profiles obtained by the etching and anodising process are shown in section 3.4.

3.2.4. GPS SILANE TREATMENT

The silane treatment used was based on the method used by Fedel [83] and follows three stages namely the hydrolysis of γ-GlycidyloxyPropyl (trimethoxySilane) (GPS), immersion of the aluminium in the GPS solution and then the drying and curing stage. This section describes all the steps in the process and includes all corresponding observations to elucidate the chemical processes as best as possible.

The hydrolysis reaction occurs in acidic medium therefore an acetic acid solution was prepared as a reaction medium. The solution had a desired pH level of 5. The process of hydrolysis was:

(a) 18.34mL Glacial acid (acetic acid in its pure form) was measured and added to a 1L volumetric flask

(b) The volumetric flask was filled to 1L with deionised water to obtain an acetic acid solution of pH 5. The pH was tested with a universal indicator.

(c) 10g of GPS was weighed off and added to an empty 1L volumetric flask and filled up with the acetic acid solution to obtain a 1% solution.

(d) The GPS and acetic acid solution did not coalesce and the GPS formed visible droplets which can be seen in Figure 3.2.1.

(e) The solution was stirred for 60 minutes at room temperature by a magnetic stirrer. After 60 minutes the droplets were no longer visible indicating that GPS had been hydrolysed and that the silane ions were present in the solution.

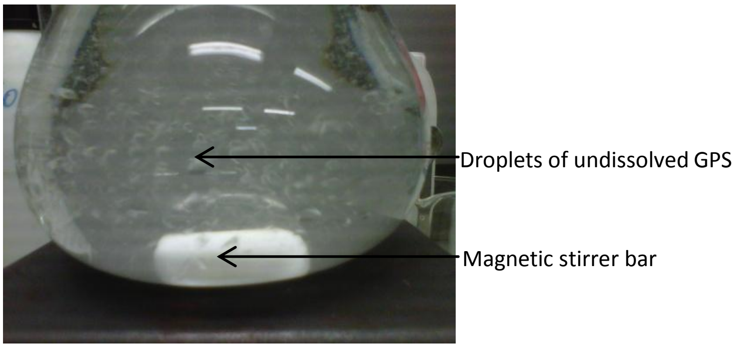

Figure 3.2.1: Experimental setup of the GPS aluminium treatment

The immersion of aluminium was a straightforward process in which the aluminium was submerged in the solution of hydrolysed GPS. Care was taken to ensure that the entire surface was submerged for 15 minutes. The aluminium was removed from the solution and air dried. The aluminium was placed in a vacuum oven for the temperature program represented in Figure 3.2.2.

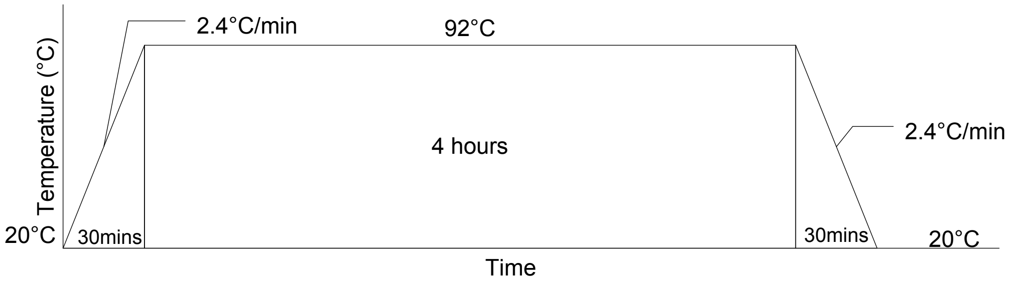

Figure 3.2.2 GPS curing temperature profile

3.2.5. ALODINING

The Alochrom 1000 finish was a chromate conversion coating or alodining process. Aluminium sheets were alodined in the United Kingdom by Runcorn Anodising Ltd. No further information about the process was disclosed.

3.2.6. REDUX 609

The film adhesive was regarded as a pre-treatment because it was applied to the aluminium and cured prior to the manufacture of the fibre metal laminate specimens. The film adhesive was applied to the aluminium under a vacuum for compaction in an oven according to the temperature program depicted in Figure 3.1.5. The lay-up for the application of the film adhesive is illustrated in Figure 3.2.3 and the lay-up sequence is outlined.

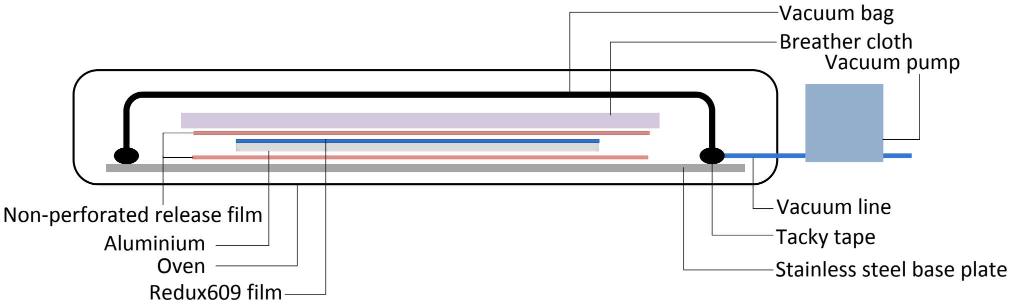

Figure 3.2.3: Configuration for the lay-up to bond Redux 609 lay-up to aluminium

(a) The Redux 609 film was cut to size with a utility knife while the protective layers were still attached.

(b) The stainless steel base plate was covered with non-porous release film.

(c) The aluminium was placed on the release film with the adherent surface facing upwards.

(d) The protective backing paper was removed and the film adhesive was placed onto the adherent surface. The polyethylene film was left on.

(e) A hand roller was used to ensure adequate contact between the film and the surface and to remove any air bubbles that would weaken the bond.

(f) The polyethylene release film was removed.

(g) A non-porous release film was placed over the lay-up followed by a breather cloth.

(h) The lay-up was covered with a vacuum bag which was sealed off with the tacky tape.

(i) The vacuum bag was shaped to include pleats that accommodated the three-dimensional shape of the lay-up.

(j) A vacuum line was connected to the vacuum bag via a vacuum breach unit and vacuum of -75kPa was applied. Figure 3.2.4 shows the lay-up once the air had been removed from the bag.

(k) The oven was set to follow the temperature program depicted in Figure 3.1.5.

Figure 3.2.4: Photograph of the lay-up for bond Redux 609 to aluminium

3.3. MANUFACTURE OF SPECIMENS

3.3.1. THREE POINT BENDING SPECIMENS

Glass Fibre Reinforced Polymer (GFRP) specimens were manufactured by different manufacturing methods to determine the influence of the method on the resin content of the GFRP. Burn-off tests were performed in which the resin was removed in an acid bath and the residual glass fibres are weighed to determine the weight fraction of glass fibre. Three Point Bend tests were performed to determine which process produced the strongest specimens which in turn indicated the specimens with best fibre to resin ratios. The results are reported in section 3.5.2 and were used to select the manufacturing process for further specimen production. The parameter variations and manufacturing methods are summarised in Table 3.3.1.

Table 3.3.1: Glass Fibre Reinforced Polymer specimens

Specimen	Method	Vacuum Pressure	Peel-Ply
WNS	Wet lay-up	-75kPa	No
WLS	Wet lay-up	-65kPa	No
WNP	Wet lay-up	-75kPa	Yes
WLP	Wet lay-up	-65kPa	Yes
IH	Infusion	-75kPa	-
IL	Infusion	-65kPa	-

3.3.2. GFRP SPECIMEN GEOMETRY

The D 7264-07 Standard Test Method for Flexural Properties of Polymer Matrix Composite Material was used as a guideline for the specimen geometry and testing parameters. The specimen geometry is shown in Figure 3.3.1. The standard thickness was 4mm, which was equivalent to the total thickness of the required SLB specimens. The D7264 standard required a span-to-thickness ratio of 32:1 therefore the support span of the supporting points on the test rig was 128mm. A 10% increase in length was recommended to allow the specimen to fit securely on the supports.

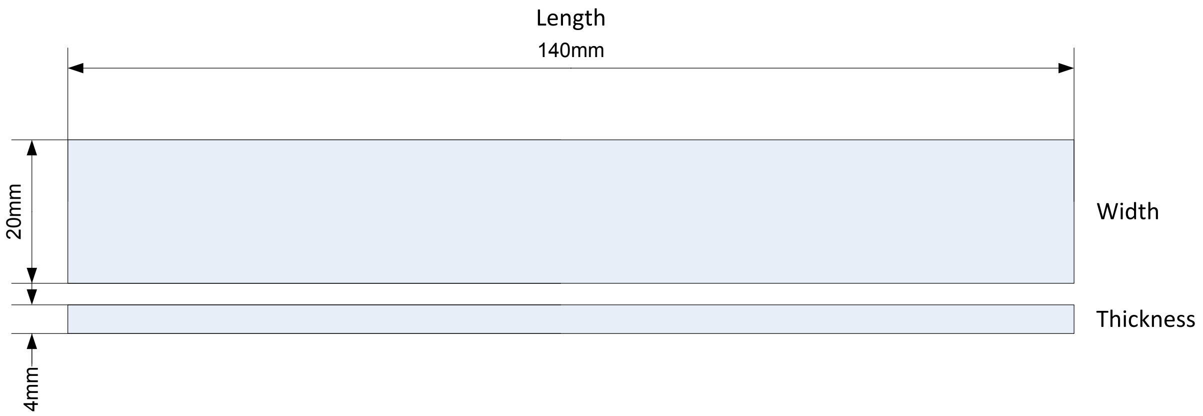

Figure 3.3.1: GFRP specimen dimensions for Three Point Bend testing

A large GFRP laminate panel was manufactured and multiple specimens were cut from it using a band saw. One specimen from each set was used to determine the fibre fraction from burn-off testing and the rest of the specimens were used to perform Three Point Bend tests. The Three Point Bend test and burn-off test results are reported in section 3.5.

3.3.3. GFRP LAMINATE PRODUCTION

The GFRPs laminates were all manufactured by consolidating 8 sheets of woven GF with Prime 20 LV resin, using either the Vacuum Assisted Resin Transfer Moulding or wet lay-up techniques. Changes were made to the vacuum pressure and lay-up configurations to determine whether the amount of resin drawn off could be reduced relative to the respective standard manufacturing methods. The different lay-up configurations are shown in Figures 3.3.2 and 3.3.3 respectively.

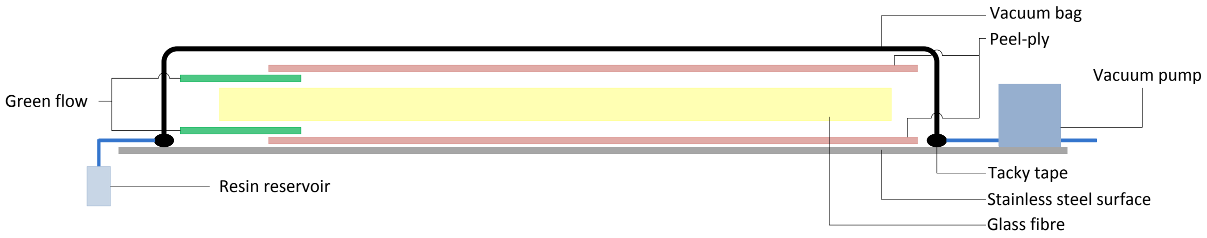

Figure 3.3.2:Vacuum Assisted Resin Transfer Moulding configuration of GFRP laminate

Four laminates were produced via the wet lay-up and manual consolidation method. The configuration depicted in Figure 3.3.3 was a variation of the standard configuration due to the inclusion of a peel-ply layer between the glass fibre and perforated release ply layers. A laminate was produced according to this configuration as well as with the standard lay-up configuration to determine whether the inclusion of the peel-ply would affect the resin content by reducing the amount of resin which was drawn off.

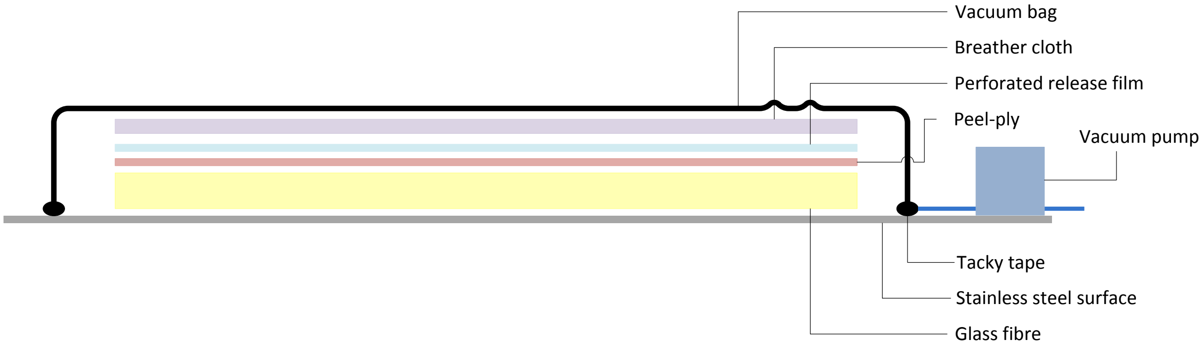

Figure 3.3.3:Wet lay-up configuration of GFRP laminate

3.3.4. SINGLE LEG BEND SPECIMENS

The Single Leg Bend test method was established to be the most suitable to determine mixed mode delamination [103]. The ASTM 7264 standard was used as a guideline for the manufacturing and testing as testing procedures for SLB tests have not yet been standardized. The geometry of individual specimens and the specific differences between the various specimens were described and summarised. The generic manufacturing method used was explained in detail.

SLB SPECIMEN GEOMETRY

The SLB test specimen was a bi-material strip of aluminium alloy bonded to a glass fibre reinforced epoxy resin laminate as illustrated in Figure 3.3.4. A non-perforated polyethylene release film was placed between the aluminium and composite pieces to produce a pre-existing crack or flaw. The non-perforated release film that was included had a 30µm thickness.

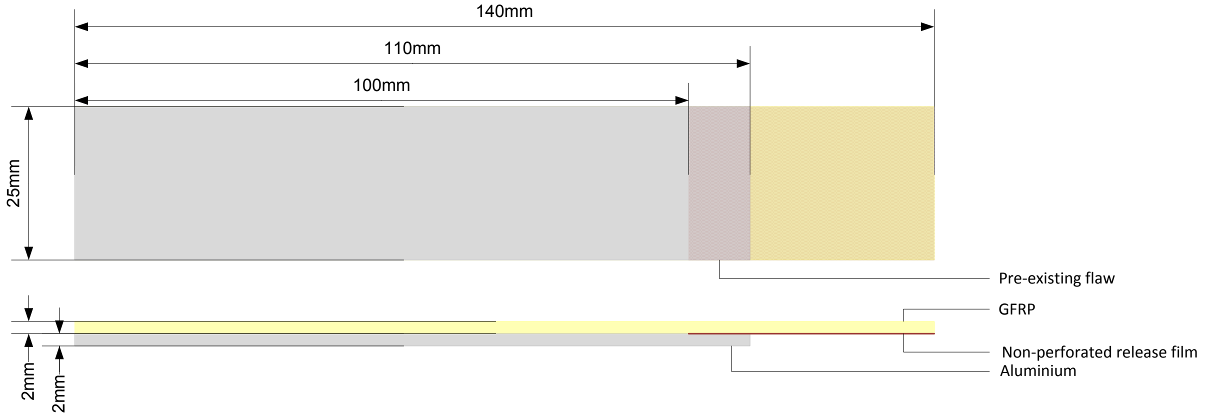

Figure 3.3.4:Single Leg Bend specimen geometry

SLB SPECIMEN DIFFERENTIATION

The purpose of the SLB tests was to quantify the ability of the aluminium-GFRP bond to resist crack growth. The crack growth was characterized by the nature of the aluminium-GFRP bond, which was influenced by the various surface preparation techniques of the aluminium and the resulting surface chemistry. The aluminium surfaces were treated prior to the SLB production, summarised in Table 3.3.2, where a cross indicates which treatment is used.

Table 3.3.2: Summary of all the Single Leg Bend Specimens manufactured for this study

Specimen Code:	Aluminium Alloy	Resin	Alodined	Bead-blasted	Etched	Anodized	GPS	Redux
PG	1005	Prime 20 LV	-	**X**	-	-	-	-
PGE	1005	Prime 20 LV	-	**X**	**X**	-	-	-
PGEN	1005	Prime 20 LV	-	**X**	**X**	**X**	-	-
PGS	1005	Prime 20 LV	-	**X**	-	-	**X**	-
PGES	1005	Prime 20 LV	-	**X**	**X**	-	**X**	-
PEN	1005	Prime 20 LV	-	-	**X**	**X**	-	-
PL	2024-T3	Prime 20 LV	**X**	-	-	-	-	-
SL	2024-T3	SE 84 LVLV	**X**	-	-	-	-	-
PLR	2024-T3	Prime 20 LV	**X**	-	-	-	-	**X**
SLR	2024-T3	SE 84 LVLV	**X**	-	-	-	-	**X**
SGR	1005	SE 84 LVLV	-	**X**	-	-	-	**X**
PGR	1005	SE 84 LVLV	-	**X**	**X**	**X**	-	**X**

The order in which surface treatments were performed for a specific specimen is the order in which the treatments are indicated by a cross from left to right, for example, bead-blasting would have occurred prior to etching. The experimental procedure for the tabulated surface treatments were specified in section 3.2. Most of the specimens were made using 1005 aluminium alloy, except the alodined specimens for which 2024-T3 aluminium alloy was used.

GENERIC SLB MANUFACTURING TECHNIQUE:

The parent SLB panel was manufactured using the wet lay-up or prepreg techniques and individual specimens were cut from it using a band saw. The configuration of both techniques is depicted in Figure 3.3.5 and Figure 3.3.6.

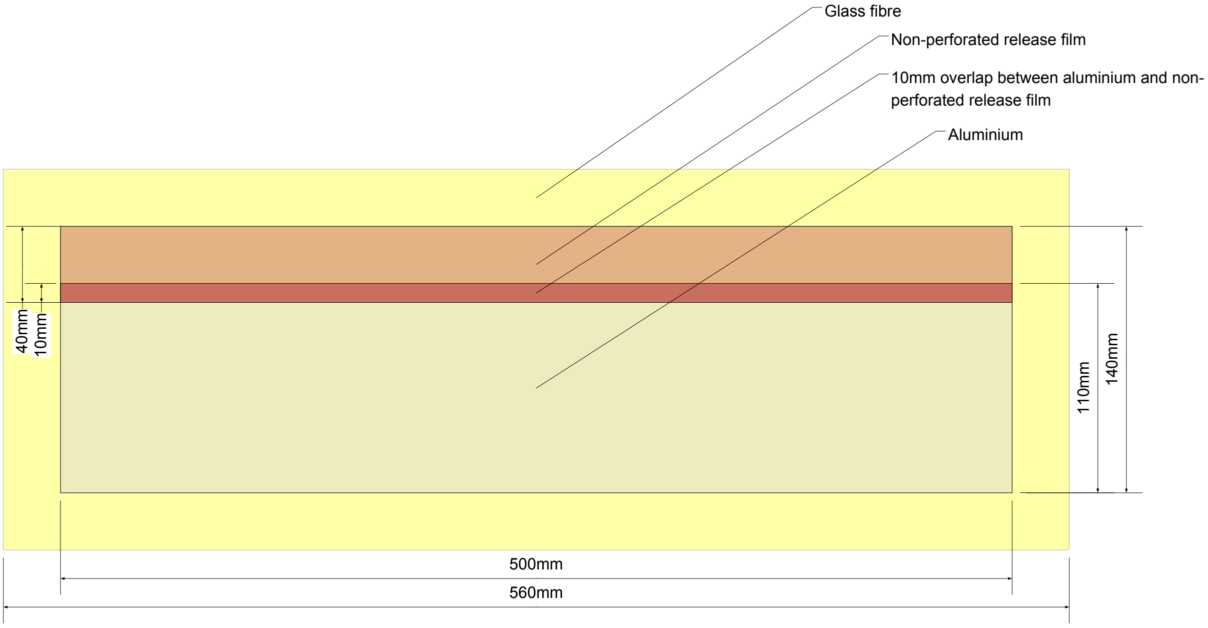

Figure 3.3.5:Configuration of the SLB specimen lay-up

WET LAY-UP OF SLB PANEL

(a) The stainless steel table top surface on which the wet lay-up was executed was waxed using Ram wax release agent prior to manufacturing to prevent the finished FML from sticking to the surface. The surface was coated with a layer of Prime 20 LV epoxy resin that had been pre-mixed with its hardener.

(b) 7 sheets of woven GF were sequentially impregnated with resin by means of a paint brush

(c) The seventh layer of GF was marked to ensure that the overlap between the aluminium and non-perforated release film was consistent.

(d) The non-perforated release film was placed in the allotted area depicted in Figure 3.3.5.

(e) The aluminium bonding surface was coated with a layer of Prime 20 LV. The aluminium was placed on top of the GF and the non-perforared release film such that there was a 10mm overlap between the aluminium and the release film as stipulated in Figure 3.3.5.

(f) A sheet of perforated release film was placed over the lay-up.

(g) A breather cloth layer was placed over the lay-up.

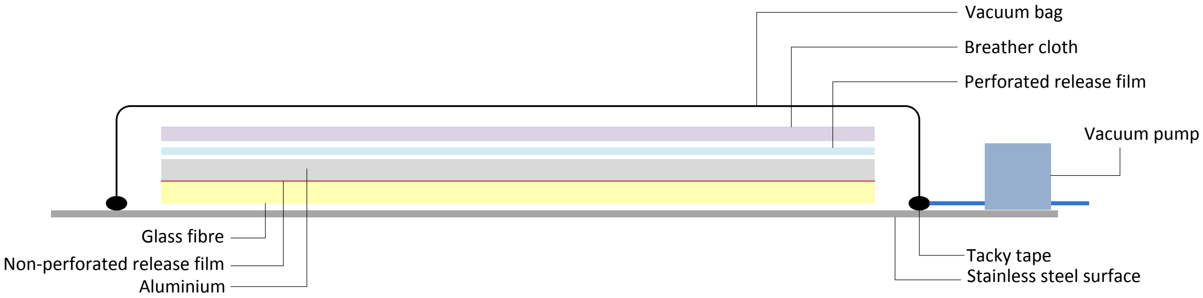

Figure 3.3.6: Sequence of parent SLB panel lay-up

(h) The surface surrounding the lay-up was cleaned of any resin and the lay-up was outlined with tacky tape. The lay-up was covered with a vacuum bag of which the edges were adhered to the stainless surface with tacky tape to seal it off. The vacuum bag was shaped to include pleats that accomodated the three-dimensional shape of the lay-up. A vacuum line was connected to the vacuum bag and a vacuum pressure of -75kPa was applied drawing excess resin into the breather cloth and removed any air resulting in a compression pressure on the lay-up.

(i) The lay-up was left under vacuum for 24 hours for the resin to cure.

(j) The vacuum bag, breather cloth, non-perforated release film and tacky tape were removed once the initial curing process had been completed.

(k) The parent SLB panel was removed from the surface and placed in an oven which was progammed to the temperature profile for post-curing Prime 20 LV.

(l) The parent SLB panel was cut up with a band saw into a set of indivual specimens as shown in Figure 3.3.7.

(m) The cut edges were polished on polishing tables with number 80 grit paper.

(n) The specimen edge that would be visible during the experiment was coated with correction fluid to increase the visibility of the formed crack.

(o) The position of the pre-existing crack was marked to simplify crack measurements.

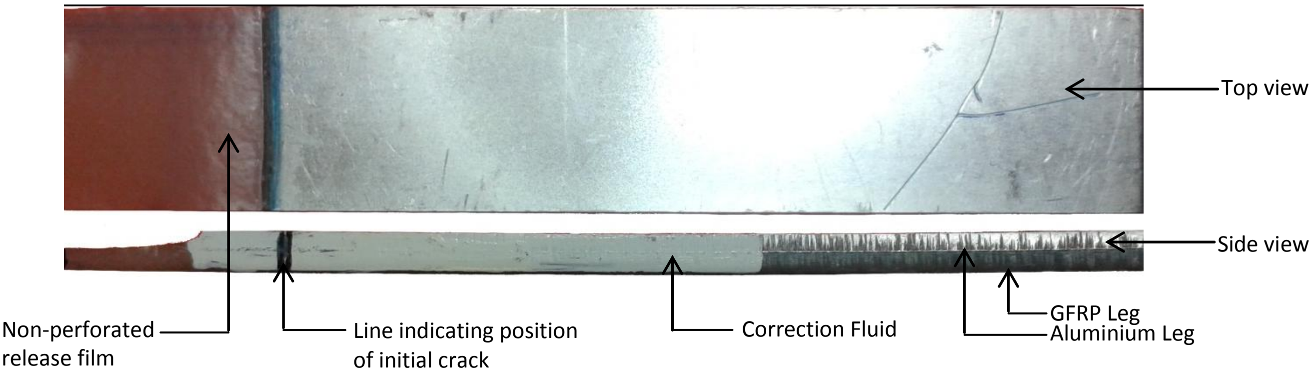

Figure 3.3.7: Finished SLB specimen

PREPREG LAY-UP OF PARENT SLB PANEL

The prepreg lay-up technique was limited to the parent SLB panels that were produced using prepreg. The process was similar to that of the Redux 609 surface treatment, as the prepreg sheets were laid-up on a base plate and cured under vacuum. Nine sheets of prepreg were used instead of seven sheets woven GF to achieve a GFRP panel of equivalent thickness. The prepreg sheets were sequentially consolidated by a stainless roller that also served to remove any air bubbles between layers. The non-perforated release film and aluminium was placed on top as in Figure 3.3.5. The curing cycle followed the temperature profile for the SE 84 LV resin.

3.3.5. FIBRE METAL LAMINATES

Fibre metal laminate specimens were produced for impact testing. The manufacturing technique that was employed was explained in detail. The material selection and relevant techniques for the individual tests were discussed separately in Chapter 5.

SPECIMEN GEOMETRY

The FML specimen dimensions were determined by the dimensions of their testing rig clamp frames which were 100mm x 100mm. The thicknesses of the specimens were not predetermined and were a result of the lay-up and manufacturing methods. The clamp frames utilized bolted systems to attach the specimens to the testing rigs, allowing for variable thicknesses.

FML MANUFACTURING METHODS

FMLs were made using the prepreg lay-up technique only. The aluminium was cut into 100mm x 100mm sheets prior to the production of the FMLs, which eliminated post-production machining of the FMLs. The aluminium 2024-T3 alloy was used to produce the specimens and the different surface treatments used were listed in Table 3.3.3.

Table 3.3.3: Summary of impact specimens manufactured for this study

Specimen	**Manufacturing Method**	**Surface Treatment**	**GF type**	**Resin**
ISG	Prepreg lay-up	GB	Woven	SE 84 LV
ISS	Prepreg lay-up	GB, Etched, GPS	Woven	SE 84 LV
ISA	Prepreg lay-up	GB, Etched, Anodised	Woven	SE 84 LV

PREPREG LAY-UP OF FMLS

The prepreg lay-up process was used to produce FMLs with prepreg sheets. The process will be explained in conjunction with the illustration of the lay-up configuration in Figure 3.3.8.

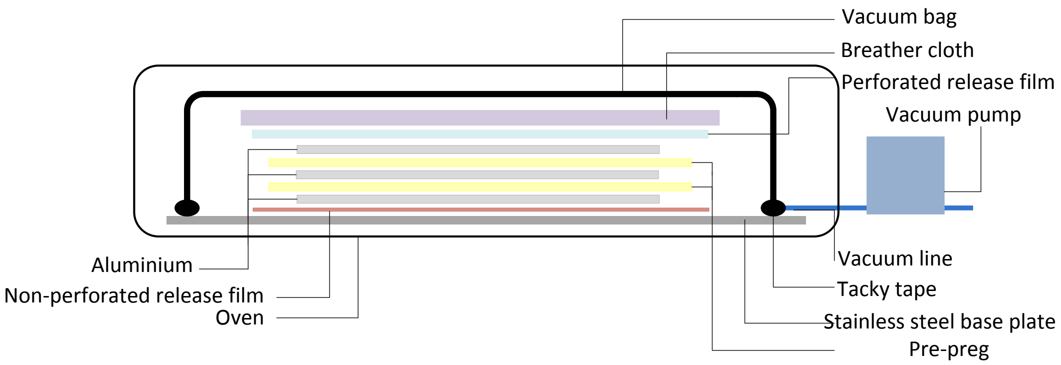

Figure 3.3.8:Prepreg lay-up of FML

(a) A non-perforated release film was placed on the stainless steel base plate on top of which the aluminium was placed with the Redux 609 side facing up.

(b) A sheet of prepreg was placed on top of the film adhesive layer with the top release film still attached. A roller was used to improve contact between the prepreg sheet and the aluminium and to remove trapped air bubbles.

(c) The top release film was removed from the prepreg. Two more sheets of prepreg were sequentially placed on top repeating step (b) and (c) each time.

(d) The sheet of aluminium with Redux 609 bonded on both sides was placed on top of the prepreg. The prepreg and the aluminium were cut to size therefore the aluminium sheets lined up.

(e) Three more sheets of prepreg were placed over the aluminium sequentially and consolidated as in step (b) and (c).

(f) The final aluminium sheet was placed with the Redux 609 side down.

(g) Perforated release film was placed over the lay-up followed by a breather cloth.

(h) The lay-up was outlined with tacky tape. The lay up was covered with a vacuum bag and sealed off with the tacky tape. The vacuum bag was shaped to include tabs or pleats that accomodated the three-dimensional shape of the lay-up. A vacuum line was connected to the vacuum bag via a vacuum breach unit. A vacuum pressure of -75kPa was applied removing any air and applied compression pressure on the lay-up. The lay-up was subjected to the temperature profile in Figure 3.1.3 while under vacuum.

3.4. TESTING OF SURFACE PREPARATION TECHNIQUES

The resultant roughness and topography of different surfaces were investigated to establish the effect of various mechanical and chemical surface treatments. An elemental analysis was performed on the surfaces of these specimens to establish the effect of the surface treatments on the surface chemistry.

3.4.1. SURFACE ROUGHNESS

The surface roughness was investigated as it has been established that the roughness has a large effect on the adhesion properties of the surface. The surface roughness of the bead-blasted, etched and anodised surfaces was measured to determine the effect of the different surface treatments on the aluminium surface. The surface was analysed with a WYKO optical profilometer. The WYKO instrument used a laser to profile the surface morphology by detecting phase changes. The roughness was measured as the departure in micrometers from a centre line. A typical surface profile of a 2.0mm by 2.0mm area obtained from the WYCO is represented in Figure 3.4.1 and the roughness measurements of bead-blasted, etched and anodised aluminium are listed in Table 3.4.1.

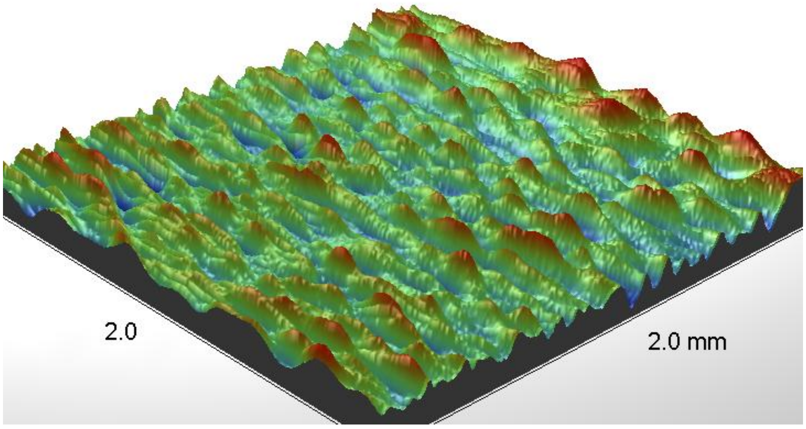

Figure 3.4.1: Typical 2.0mm x 2.0mmm surface profile obtained from a WYCO scan

Table 3.4.1: Roughness values obtained from WYCO for different surface treatments

		Bead-blasted	**Etched**	**Anodised**
R_a	Arithmetic mean roughness	6.68µm	4.97 µm	6.94 µm
R_q	Quadratic mean roughness	8.41µm	6.20 µm	8.70 µm
R_z	Mean peak to valley height	53.08 µm	40.04 µm	56.58 µm
R_t	Max peak to valley height	62.10 µm	46.52 µm	67.06 µm

3.4.2. SURFACE TOPOGRAPHY

The surface topography was inspected with a Scanning Electron Microscope to identify the shape and distribution of features on the surface of the treated aluminium. The surface topographies of the bead-blasted, etched and anodised surfaces were investigated and the images that were obtained are shown in Figures 3.4.2, 3.4.3 and 3.4.4.

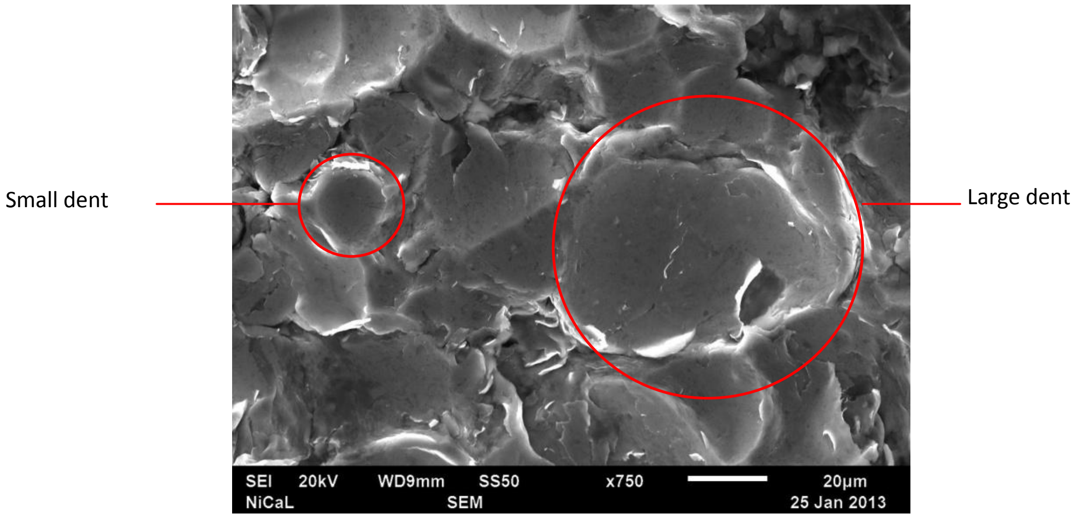

Figure 3.4.2: SEM image of a bead-blasted surface

Dents are evident in the SEM image of the bead-blasted surface in Figure 3.4.2. The effect of a large range of bead-particle diameters (100-500µm) was evident on the surface as the size of the dents that the bead particles had created on the surface varied substantially.

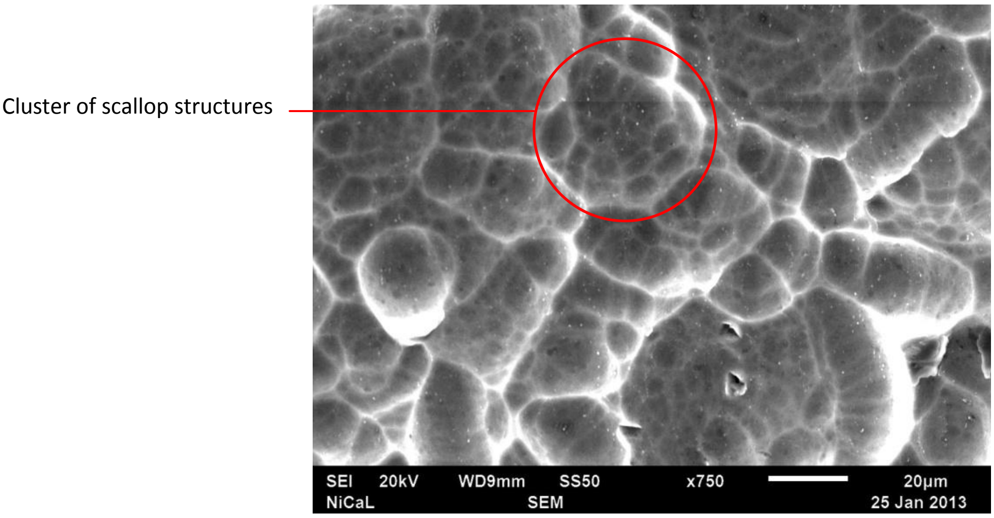

Figure 3.4.3: SEM image of a bead-blasted and etched surface

The etched surface in Figure 3.4.3 shows a typical scalloped appearance, but it was not clear whether the scallop structures were concave or convex. The scalloped structures seemed to be grouped together in clusters and it was speculated that the micro-roughness achieved from the etching was superimposed on the macro-roughness obtained from the bead-blasting.

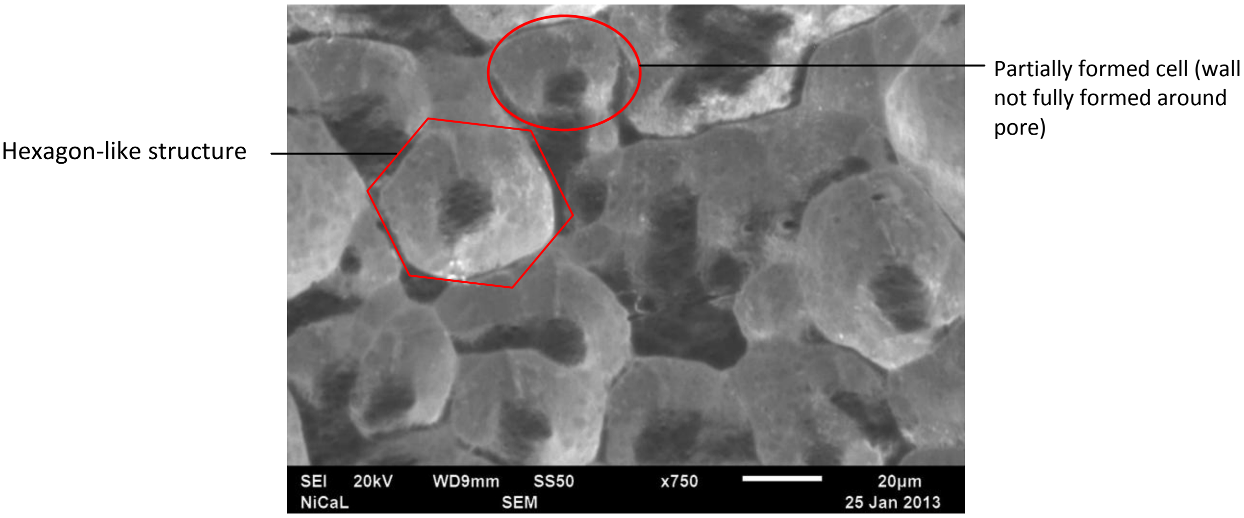

Figure 3.4.4: SEM image of a bead-blasted, etched and anodised surface

The anodised surfaces shown in Figure 3.4.4, exhibited hexagon-like structures that resembled the hexagonal cells described in Section 2.3.2. The porous stucture was evidence of the formation of a surface oxide. The cell shapes were not very consistent as some cells were only partially formed, but this could have resulted from the spatial confinement imposed by the macro-roughness.

‘AnalyzingDigitalImages’ freeware package was used to determine the diameter of the pores, the diameter of the cells and the inter-pore distance. The inter-pore distance was measured from the circumference of a selected pore to the circumference of a pore of an adjacent cell. The results are reported in Table 3.4.2. A significant variation in the cell diameter and inter-pore distance was observed, whereas the pore diameter and cell diameter appeared to be more consistent.

Table 3.4.2: The pore diameter, cell diameter and inter-pore distances of the anodised surface oxide

	Pore Diameter (μm)	**Cell Diameter (μm)**	**Inter-pore distance (μm)**
Average:	12.3	39.0	34.1
Standard deviation:	1.8	2.9	8.8

3.4.3. SURFACE ELEMENTAL COMPOSITION:

An Energy Dispersive X-ray spectrometry (EDX) function was used with the SEM to determine the elemental composition on the surface of the surface treated aluminium. The magnitude of the peaks in the spectra in Figures 3.4.5, 3.4.6 and 3.4.7 indicated the relative quantity of the respective elements on the surface of the aluminium. The spectra all displayed large peaks at 0 keV which were known as zero loss peaks. Electrons did not interact with the specimens or were diffracted and therefore they exhibited a zero loss in energy, i.e. 0 eV [125].

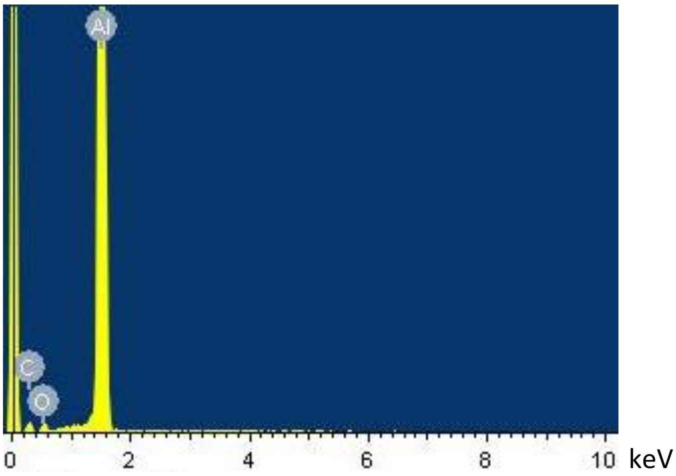

Figure 3.4.5: The elemental composition of a bead-blasted surface

The element with the highest percentage occurrence on the surface of the bead-blasted aluminium alloy was Aluminium. The spectrum in Figure 3.4.5 only showed small quantities of oxygen and carbon. The carbon was indicative of trace amounts of impurities on the surface. The small amount of oxygen indicated small amounts of hydroxide and oxide groups available on the surface

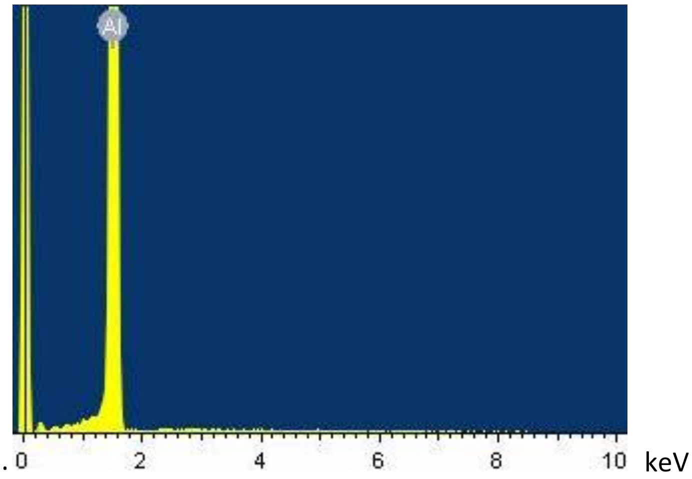

Figure 3.4.6: The elemental composition of an etched surface

Aluminium was the only element that was present in a significant quantity on the surface of the bead-blasted and then etched aluminium specimen represented by the spectrum in Figure 3.4.6. The occurrence of oxygen and carbon were negligible compared to the bead-blasted aluminium surface.

This was indicative of the successful removal of the unstable aluminium oxides and any residual contaminants on the surface of the aluminium.

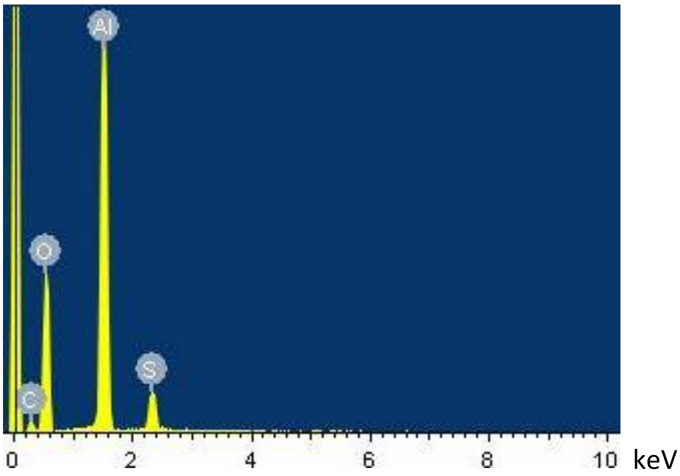

Figure 3.4.7: The elemental composition of an anodised aluminium sample

The spectrum of the anodised specimens in Figure 3.4.7 exhibited an increase in oxygen, sulphur and carbon over that of the etched specimens. The increase in the oxygen and the sulphur was indicative of the formation of the surface oxide with the sulphur from the sulphuric acid anodising bath being incorporated into the oxide structure. The carbon could be as a result of an unknown compound added to the anodising electrolyte or could be due to contaminants as a result of handling the specimen.

3.5. TESTING OF COMPOSITE MANUFACTURING TECHNIQUES

Preliminary tests were performed to determine the influence of the manufacturing method on the SLB specimens. It was observed that the glass fibre sheets did not display the typical transparency which was expected from the adequate wetting of GF by resin. An investigation was done to determine whether there was indeed a lack of resin and any possible causes. Six sets of GFRP specimens were produced to submit for burn-off tests that determine the fibre fraction. Three Point Bend tests were also performed to determine the specimens' peak flexure stress as their load bearing ability was an indication of the extent of fibre wetting and subsequent load transfer.

Inadequate wetting could be ascribed to a shortage of resin relative to the glass fibre and/or the ineffective impregnation of the fibres due to the manufacturing method. The GFRP specimens were made by varying the manufacturing techniques and parameters which are summarised in Table 3.3.1. Specimens were made by the wet lay-up and infusion techniques to determine its effect on the resin content and/or the fibre impregnation. The vacuum pressure was altered for both manufacturing techniques to determine the influence of the pressure on the resin content by drawing off too much/little resin. Peel-ply was used in addition to the perforated release film and breather cloth to determine whether it would retard resin flow and affect the resin content.

3.5.1. BURN-OFF TESTS

The burn-off tests were performed to determine the exact fibre to resin ratios of the GFRP specimens. The testing was outsourced to Durban University of Technology. The volume fraction and mass fraction were determined and are displayed in Figure 3.5.1.

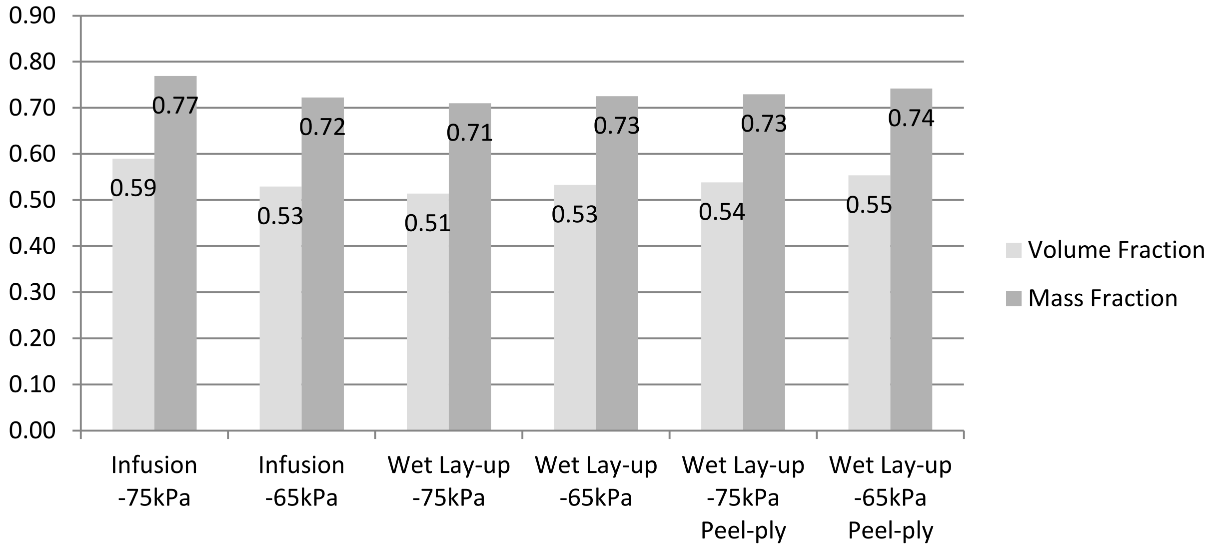

Figure 3.5.1: The resultant glass fibre volume and mass fractions of different manufacturing methods determined by burn-off tests

The infusion and wet lay-up techniques executed at a lower pressure of -65kPa resulted in lower GF volume and mass fractions compared to the respective techniques executed at -75kPa, indicating that less resin was drawn from the GFRP at -65kPa. The wet-lay-up processes modified with the inclusion of the peel-ply layer had higher GF fractions than the wet lay-up processes executed without the peel-ply layers. This was contrary to expectation as the purpose of the peel-ply was to reduce the resin flow from the GFRP. The peel-ply layer could have absorbed some of the resin which would reduce the resin content fraction, but this effect would be minimal.

3.5.2. THREE POINT BEND TESTS

Three Point Bend (TPB) tests were performed to determine the flexural strength of the GFRP as the flexural strength was a good measure of the matrix / reinforcement interaction and therefore of the fibre impregnation and fibre wetting.

The tests were performed on a Three Point Bend test rig which was set up on a Zwick 1484 Roell quasi-static test machine as represented in Figure 3.5.2. The support span was set at 128mm. The cross head speed was set at 1mm.min^{-1} according to the D 7264-07 standard test procedures. The force-deflection data was recorded and exported by the testXpert V10.11 software.

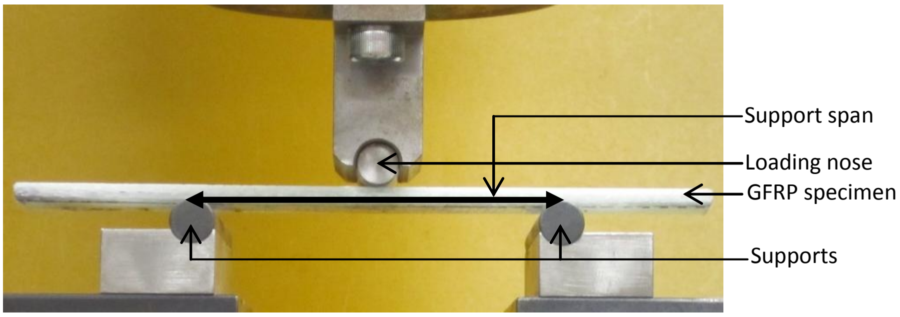

Figure 3.5.2: Three Point Bend test rig setup up on the Zwick

Each test was completed once an outer surface of the specimen failed. All the specimens failed by compression on the upper surface at the loading nose and local buckling manifesting as fibre micro-buckling.

The recorded force-deflection data was used to calculate the stress and strain for each specimen. The stress was linearly proportional to the strain up to the point of failure therefore Equation 3.1 could be used to determine the flexural stress from the applied force, *P* (N), the support span, *L* (mm), width of the beam, *b* (mm), and the beam thickness, *h* (mm) [126].

$$\sigma = \frac{3PL}{2bh^2} \tag{3.1}$$

THREE POINT BEND TEST RESULTS

The average peak stress obtained for each specimen type is shown in Figure 3.5.3. The infusion and wet lay-up techniques executed at a lower vacuum pressure of -65kPa showed higher peak stresses compared to the respective techniques performed at -75kPa.

The GFRPs produced via the wet lay-up technique at -75kPa had a significantly lower fibre content than the GFRP's produced with infusion at -75kPa as well as a lower peak failure stress. This suggested that the higher fibre content of the infused GFRPs contributed to their higher peak failure stress. The infused GFRPs manufactured at -65kPa had a higher peak failure stress than those manufactured at -75kPa suggesting that the specimens manufactured -65kPa had a more uniform resin distribution and better fibre wetting. At -65kPa vacuum pressure the resin content of the infusion and wet lay-up techniques were equivalent (0.53), but the wet lay-up technique produced GFRP specimens with higher peak stress suggesting the technique had promoted a better distribution of resin.

The GFRPs manufactured with the peel-ply showed an inverse dependence of peak stress to vacuum pressure despite having a high resin content. It was speculated that the peel-ply reduced the amount of resin drawn off, but affected the distribution of resin within the GFRP which would decrease its peak stress.

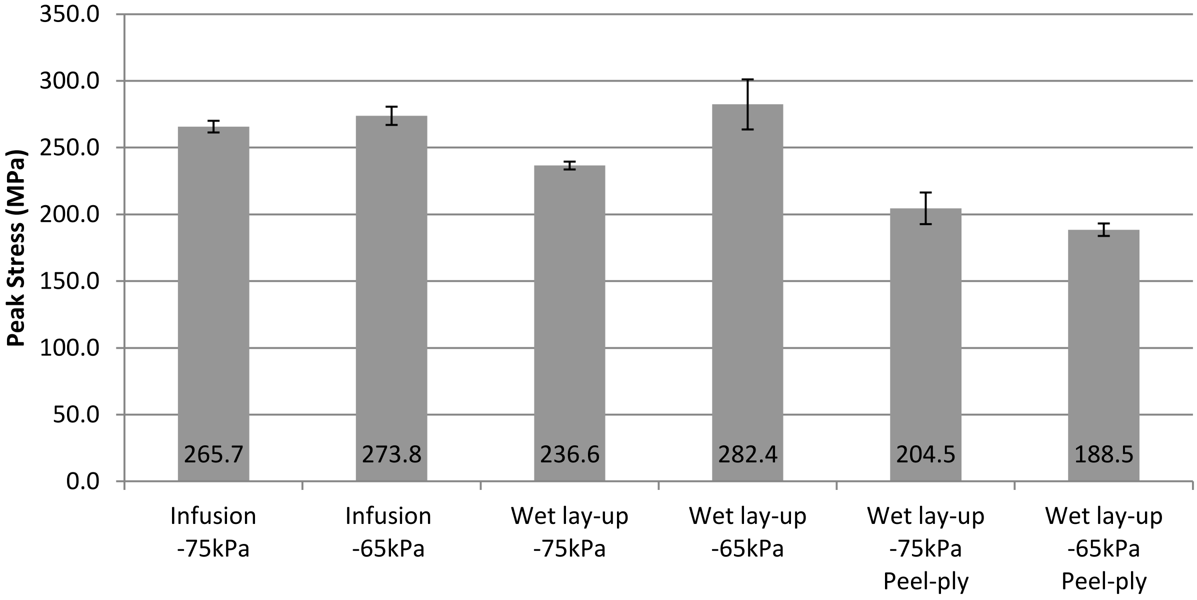

Figure 3.5.3: The peak failure stress from the Three Point Bend tests of GFRP specimens manufactured with different techniques

3.6. SUMMARY OF TEST RESULTS

The surface roughness, SEM and elemental analyses were performed to determine the effect of the surface treatments on the aluminium surface topography and chemistry which would ultimately affect the adhesion properties of those surfaces.

- The anodised specimens and bead-blasted specimens exhibited a similar surface roughness, with the anodised specimens having a higher surface roughness. The etched surface had the lowest surface roughness.
- The bead-blasted surface had a dented surface, the etched surface was scalloped and the anodized surface was porous.
- The bead-blasted surface contained oxide groups and carbon contaminants. The etched surface was almost purely aluminium with the occurrence of other elements being negligible. The anodised specimens exhibited a high occurrence of sulphur and oxygen which was associated to the formation of the porous surface oxide.

Burn-off tests and Three Point Bend tests were performed to determine the manufacturing technique that provided the best fibre fractions and the best fibre wetting.

- The infusion technique produced GFRPs with higher fibre volume fraction and the specimens produced at-75kPa vacuum pressure had the highest fibre volume content.
- The techniques performed at -65kPa vacuum pressure produced GFRPs with higher peak failure stresses.
- The wet lay-up technique performed at -65kPa vacuum pressure produced GFRPs with the highest peak failure stress and therefore the best fibre wetting and most uniform resin distribution.
- Incorporating peel-ply into the wet lay-up technique produced GFRPs with higher resin content, but with lower peak stresses.

3.7. DISCUSSION

3.7.1. MANUFACTURING MATERIALS:

The FM 94 resin with which the GLARE GFs were impregnated were also commercially available in film adhesive form. The adhesion properties of the FM 94 (Cytec) and Redux 609 (Hexcel) were compared based on results provided by their respective datasheets, reported in Table 3.7.1 [123, 127]. The FM 94 film was supported by a polyester knit and the Redux 609 film was supported by a cotton scrim. Similar tensile test results suggested that the two film adhesives had similar mechanical properties. The single lap shear strength and the peel strength of the FM 94 film was superior.

Table 3.7.1: Comparison of Redux 609 and FM 94 film adhesives

	Temperature (°C)	Areal Weight	Single Lap shear strength (MPa)	Flatwise Tensile test (MPa)	Floating Roller Peel strength
			ASTM D1002	ASTM C297	ASTM D3167
FM 94	24	293g.m^{-2}	46	8.2	12.9 N.mm^{-1}
Redux 609	22	300g.m^{-2}	33	7	3.0 N.mm^{-1}*

*Bell peel strength of 76N/25mm reported, Bell peel and Roller Peel test equivalent [128]

The adhesive properties of the SE 84 LV resin were not available independently of the prepreg product and only the matrix properties of the Prime 20 LV were reported therefore comparisons could not be made.

3.7.2. SURFACE PRE-TREATMENT METHODS

The bead-blasted aluminium produced for this study exhibited a higher surface roughness than the bead-blasted and then etched aluminium. The elemental surface analysis in section 3.4.3 showed that the etched specimens had lower oxygen and carbon content compared to the bead-blasted specimens. This indicated that the decrease in surface roughness could be attributed to the removal of unstable surface oxides on the bead-blasted surface. The surface roughness values obtained in this study were compared to surface roughness values found in literature in Table 3.7.2. The surface roughness values obtained for the bead-blasted specimens in this study were comparable to those obtained by Johnsen [84], but were significantly higher than those found by Liu [63] and Rider [62]. The roughness of the etched specimens was significantly higher (approximately ten times) than those reported in literature. The surface roughness has been shown to both increase [129] and decrease [66] with the etch duration and temperature, therefore the difference in roughness could not be attributed to a specific parameter in this case as the etching conditions were not disclosed by Cape Anodising Pty.

Table 3.7.2: Comparison of surface roughness values obtained in this study to those published in literature

	Present Study		**Johnsen [84]**		**Liu [63]**	**Rider [62]**	**Park [60]**
	Ra (μm)	Rt (μm)	Ra (μm)	Rt (μm)	Ra(μm)	Ra(μm)	Ra(μm)
Bead-blasting	6.68	62.10	4.44	35.95	1.78	1.6	-
Alkaline Etch	4.97	46.52	0.60	5.36	-	-	0.58
Anodising	6.23	59.10	0.98	10.33	-	-	-

Ra – arithmetic mean of the deviation from the surface profile
Rt – maximum height of profile

The bead-blasted specimens and the anodised specimens had a similar surface roughness, both greater than the etched aluminium specimens. The elemental analysis of the anodized specimen indicated a higher oxygen and sulphur content compared to both the bead-blasted and etched specimens suggesting a stable surface oxide built up during the sulphuric acid anodising process. The stable oxide layer had distinctive pores as described in section 2.3.2 to which the increase in peak to valley distance (R_t) could be attributed. The surface roughness of the anodised specimens produced in this study was also significantly higher (approximately 6 times) to those found in literature, however the oxide morphology, including the pore depth, was highly dependent on the operating conditions [64]. The texture of the etched surface also transfers to the anodised surface [48] which could substantiate the higher surface roughness of the anodised specimens compared to those of Johnsen [84].

SEM images in Figure 3.7.1(a) revealed the amorphous surface morphology of the anodised aluminium surfaces where hexagonal structures were identified with a central pore. Neither the shape nor the distribution of the oxide cells was consistent, but the pore size remained relatively constant at approximately 12μm. These pore sizes were, however, three orders of magnitude larger compared to the reported 25nm for Chromic Acid Anodising (CAA) [48], 19-26nm for Sulphuric Acid Anodising (SAA) [130] and 32nm for Phosphoric Acid Anodising (PAA) [64]. The highly ordered nano-porous structure in Figure 3.7.1(c) was achieved in a sulphuric acid bath [130] therefore the anodising voltage and temperature were more likely to have affected the pore size and distribution than the electrolyte composition. The pore diameters of the SAA treated aluminium produced in the present study were large enough to permit pore penetration by the primer or resin, however the low pore density resulted in substantially lower effective surface area over which bonds could form compared to the higher density porous oxides.

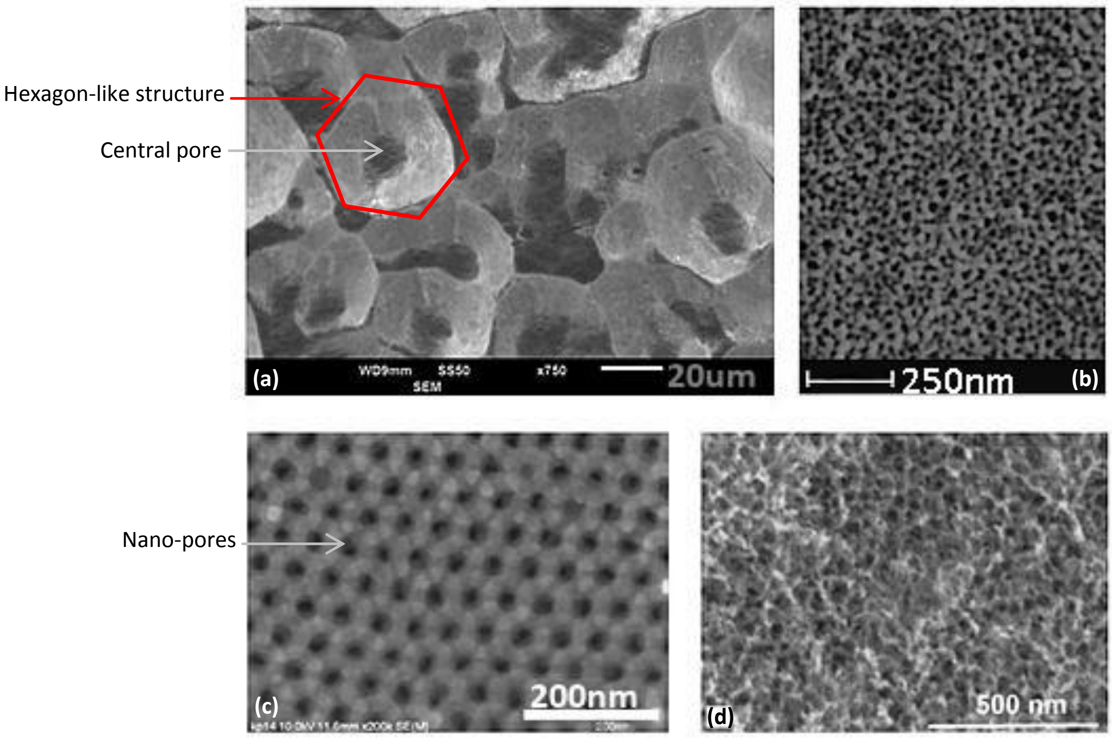

Figure 3.7.1: SEM images of (a) the sulphuric acid anodised aluminium surface in this study, (b) porous structure produced by CAA [48] (c) the surface of well-ordered nano-pores created by optimised sulphuric acid anodising [130] and (d) the surface of FPL etched and PAA anodised aluminium [75].

3.7.3. MANUFACTURING TECHNIQUES:

Three Point Bend tests and burn-off tests reported in section 3.5 determined that the wet lay-up technique produced GFRPs with a higher peak failure stress under flexural loading compared to GFRPs produced via infusion technique. This suggested that the impregnation of the woven GF fabric by the resin was more uniform or that the presence of fibre-fibre contacts or voids was lower when the wet lay-up technique was employed. The advancing resin front which was visible during the infusion of GFRPs was obscured by the outer aluminium skins in the case of FML manufacture. There was uncertainty about the effect of the aluminium skins on the infusion process and how it affected the consistency of the advancing resin front across the width of the FMLs. The SLB and FML specimens were therefore produced via the wet lay-up technique or by the consolidation of prepreg sheets.

The preliminary FMLs specimens were manufactured as large sheets described in Appendix B. This required machining of the sheets into 100mm x 100mm specimens. The machining created flaws at the edges of the specimens, which facilitated debonding upon impact. The manufacturing of the FML impact specimens described in section 3.4 was a revised technique that limited machining to the drilling necessary for clamp frame screws.

The Redux 609 film adhesive and the GFRPs were cured in separate curing processes. This means that the film adhesive was subjected to its own curing cycle and then the curing cycle of either the Prime 20 LV resin or the prepreg. The time lapse between the initial Redux 609 curing cycle and the final curing cycle varied for the different resins as the prepreg resin was already partially cured and only required a short curing cycle whereas the Prime 20 LV resin had to harden at room temperature for 24 hours prior to an additional post-curing cycle. Any effect of the subsequent curing on the mechanical and bonding properties of the film adhesive was not immediately obvious from the results in this study. These effects were not investigated as this was beyond the scope of the project, but it should be noted and considered for future testing.

CHAPTER 4: SINGLE LEG BEND TESTS

The purpose of this chapter was to identify the most promising surface treatments under quasi-static conditions to be used for the manufacture of impact specimens. The performance of the different surface treatments and adhesive interfaces was determined by means of Single Leg Bend (SLB) tests. The SLB test measured the interfacial fracture toughness of the adhesive interface, namely the Energy Release Rate (G_{I-II}), by determining its resistance to debonding or crack growth. This chapter explains the experimental details and will report the results of the different surface treatments.

4.1. SLB EXPERIMENTAL DETAILS

4.1.1. EXPERIMENTAL PROCEDURE

The SLB experimental procedure, proposed by Yoon and Hong [131], was based on a modified Three Point Bend setup. The SLB test setup included a 2mm thick spacer, depicted in Figure 4.1.1, ensuring that the GFRP laminate was level on the supports by compensating for the specimen geometry. The specimen geometry and manufacture was specified in section 3.3. The rig was set up on a Zwick 1484 Roell testing machine with the support span set to 80mm. The software used to capture and export the results was the testXpert V10.11 program.

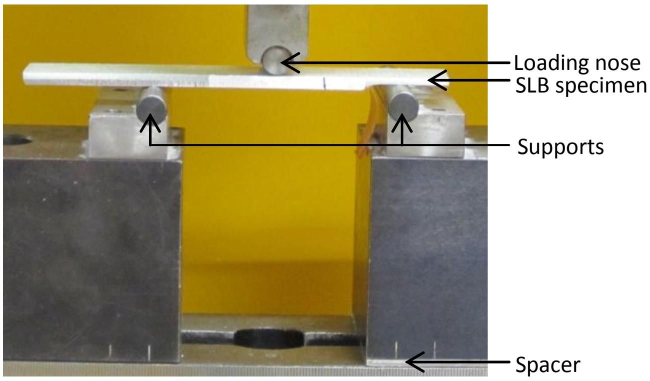

Figure.4.1.1: The Single Leg Bend test setup on the Three Point Bend test rig

The SLB test had two parts: a compliance calibration to account for flexure of the GFRP and a crack propagation test. The compliance was calibrated as a function of crack length, which was the distance from the tip of the pre-existing flaw (marked with a line in Figure 4.1.2(a)) to the centre of the support. The crack length was varied by adjusting the position of the specimen relative to the bottom supports. The crosshead speed was set to 1mm.min^{-1}, with an upper force limit of 50N. The force and displacement data were captured and collected for five different crack lengths, each at a given specimen position. The results were discarded if any crack growth occurred during the compliance test.

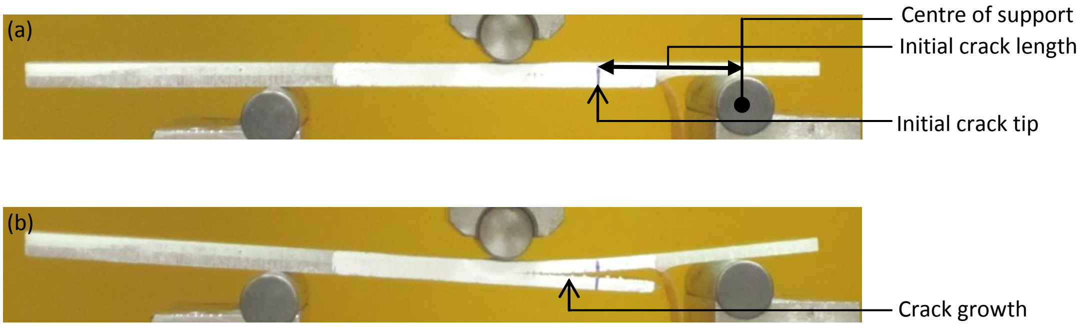

Figure.4.1.2: The SLB test specimen setup, indicating (a) the initial crack length and (b) the crack growth

The crack propagation rate was determined from images that captured the crack tip progression as a function of the time. A timer function on a Canon IXUS 100 IS digital camera was used to capture images at time intervals of nominally 3 seconds, the first of which was taken at t = 0 seconds. The time at which each image was captured was obtained from the digital time stamp of each image. The SLB specimen was positioned on the supports as seen in Figure 4.1.2(a) and the initial crack length was measured. The specimen edge extended at least 20mm past the support to prevent the specimen from falling through the supports when flexed. The crosshead moved at a speed of 1mm.min^{-1} and upon flexure of the GFRP, the aluminium cantilever would separate from the GFRP producing crack growth as shown in Figure 4.1.2(b). The test was terminated when the crack reached the loading nose. Force, deflection and time data was captured and used to calculate the energy release rate.

4.1.2. DATA PROCESSING

The results from the compliance calibration and the crack progression tests were used in conjunction with the Equation 4.1 [103] to determine the energy release rate ($G_{I\text{-}II}$) from the Force, P (N), specimen width, b (mm), compliance, C (mm.N^{-1}) and crack length, a (mm). The calculations were performed using MATLAB software:

$$G_{I-II} = \frac{P^2}{2b} . \frac{\partial C}{\partial a} \tag{4.1}$$

The compliance calibration produced a linear force versus displacement curve for each crack length, with a gradient (stiffness) decreasing with increasing crack length. The compliance at each crack length was obtained from the inverse of the respective gradient. The compliance was plotted as a function of crack length which was modelled by a third order polynomial and was designated:

$$C(a) = c_3 a^3 + c_2 a^2 + c_1 a + c_0 \tag{4.2}$$

The derivative of this polynomial was then equated to the change in compliance as a function of crack length which was used to calculate the energy release rate.

$$\frac{\partial C}{\partial a} = C'(a) = 3c_3 a^2 + 2c_2 a + c_1 \tag{4.3}$$

The digital photographs were used to measure the crack growth from the position of the initial crack to the position of the progressing crack tip. The image processing module in MATLAB was utilized to identify the crack tip position for each time step. The crack length, a, was obtained by the addition of the crack extension to the initial crack length. The force, P, was obtained from the force data that was captured by the Zwick.

4.2. SLB TEST RESULTS

The adhesive performance of individual and combined surface treatments was tested. The tests were grouped and compared to determine the influence of the mechanical surface treatments, chemical surface treatments, resin, and film adhesive on the adhesive ability of an aluminium surface. Table 4.2.1 contains a summary of all the surface treatments used to manufacture the different SLB specimens.

Table 4.2.1: Summary of the SLB specimens and their respective surface treatments

Specimen:	**Resin**	**Surface Treatment**	**Glass Fibre**
PG	Prime 20 LV	Bead-blasted (GB)	Plain weave 400g.m^{-2}
PGE	Prime 20 LV	GB, etched	Plain weave 400g.m^{-2}
PGEN	Prime 20 LV	GB, etched, anodised	Plain weave 400g.m^{-2}
PGES	Prime 20 LV	GB, etched, silane	Plain weave 400g.m^{-2}
PGS	Prime 20 LV	GB, silane	Plain weave 400g.m^{-2}
PEN	Prime 20 LV	Etched, anodised	Plain weave 400g.m^{-2}
PL	Prime 20 LV	Alodined	Plain weave 400g.m^{-2}
PGR	Prime 20 LV	GB, Redux 609	Plain weave 400g.m^{-2}
PLR	Prime 20 LV	Alodined, Redux 609	Plain weave 400g.m^{-2}
SL	SE 84 LV (prepreg)	Alodined	Plain weave Prepreg
SGR	SE 84 LV (prepreg)	GB, Redux 609	Plain weave Prepreg
SLR	SE 84 LV (prepreg)	Alodined, Redux 609	Plain weave Prepreg

The predominant failure mode was debonding that occurred between the GFRP and the aluminium surface. A microscope image is shown of the aluminium surface after a typical SLB experiment in Figure 4.2.1. The aluminium was bare except for a few isolated patches of resin. The adhesive bond between the epoxy resin and the glass fibre was stronger than the bond between the resin and the aluminium as the resin remained attached to the glass fibre. The glass fibre bonding therefore had far less influence than the bond between the resin and the aluminium and the type of glass fibre was not considered a factor of the adhesive strength.

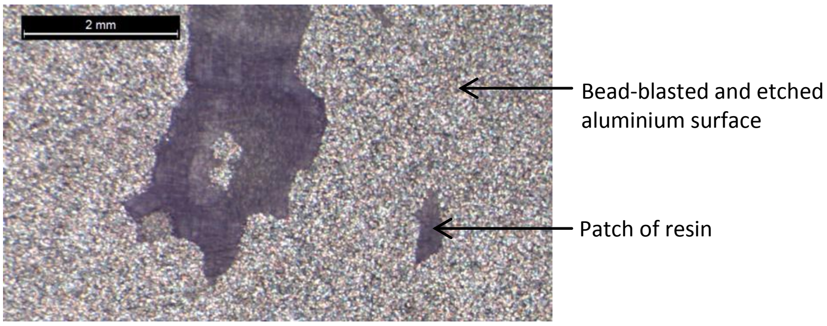

Figure 4.2.1: Microscope image of the aluminium surface after a SLB test (PEN series)

4.2.1. SLB SPECIMEN RESULTS

Typical force and crack extension data, plotted as a function of time for a single specimen, is shown in Figure 4.2.2. The force increased linearly until a peak force was reached, then decreased gradually. The force curve indicates crack growth at t=60s although according to the crack extension data crack growth only starts at t=70s. The crack propagation between t=60s and t=70s was not observable or visible, where the arrow indicates the beginning of observable crack growth. The force value that coincided with the observed start of crack propagation was the Crack Initiation Force (F_{CI}) as determined from the photographs and the peak force (F_{max}) was the maximum force recorded for the duration of the experiment.

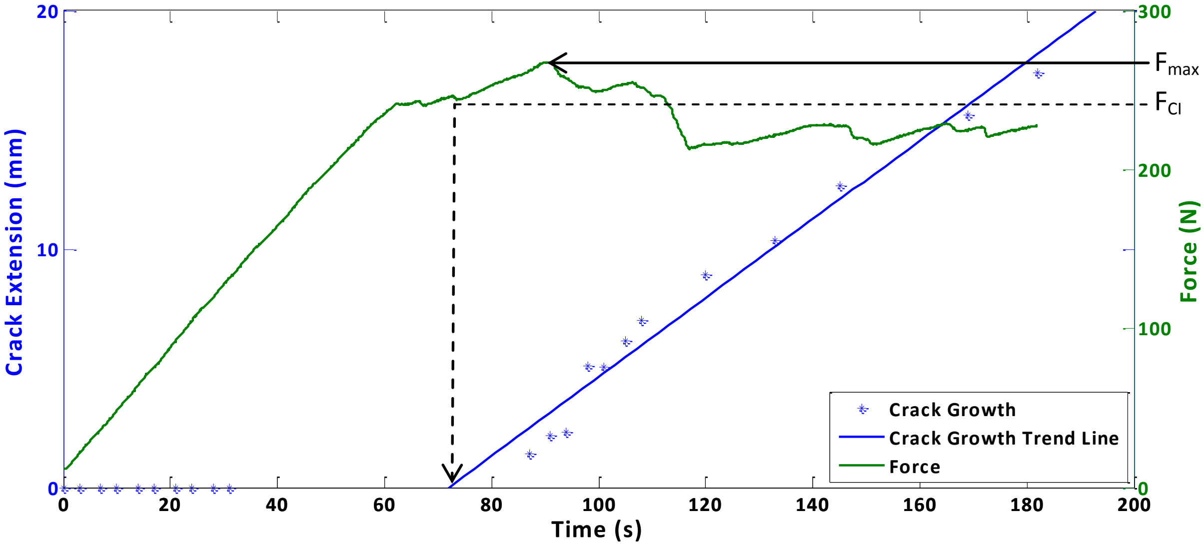

Figure 4.2.2: Graph of the force and crack extension data as a function of time

The crack extension rate was relatively constant and increased linearly with time from the point of crack initiation, as described by the solid blue trend line in Figure 4.2.2. The slope of this trend line represented the magnitude of the Crack Growth Rate (*CGR*) in mm.s^{-1}.

The force and the energy release rate are plotted as a function of crack extension (c_{ext}) in Figure 4.2.3. The force curve did not show any significant fluctuation for the duration of the crack propagation. Prior to crack extension (at $c_{ext} = 0$) the energy release rate increased until the point of crack initiation (G_{CI}). The specimens typically exhibited a relatively linear increase in the energy release rate as a function of crack extension.

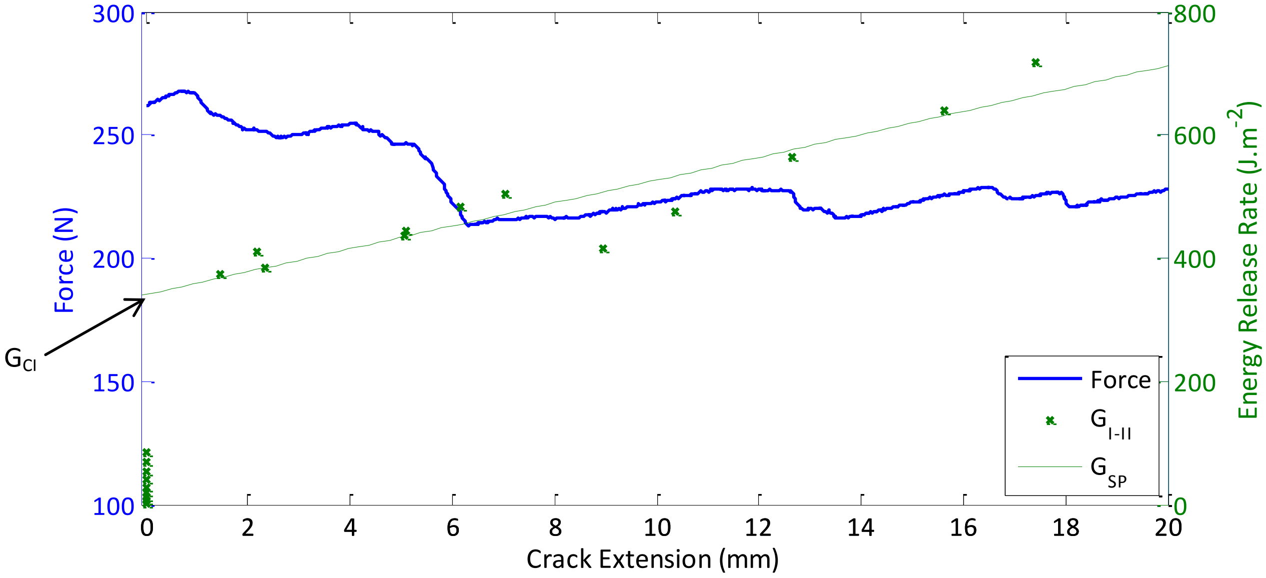

Figure 4.2.3: Graph of the force and energy release rate as a function of crack extension

In isolated cases, a specimen demonstrated an initial steep rise in the energy release rate after the point of crack initiation followed by a decrease in G_{I-II}, as seen in Figure 4.2.4. The steep rise could be ascribed to an increase in force that was required to initiate crack growth, followed by a drop in force once the crack had been initiated. This could be due to a flaw in the manufactured pre-existing crack. G_{I-II} then stabilized within the first 2mm of crack growth. In these cases, the stable propagation energy release rate (G_{SP}) trend was determined from the point of stabilization, whereas it was normally determined from the point of crack initiation.

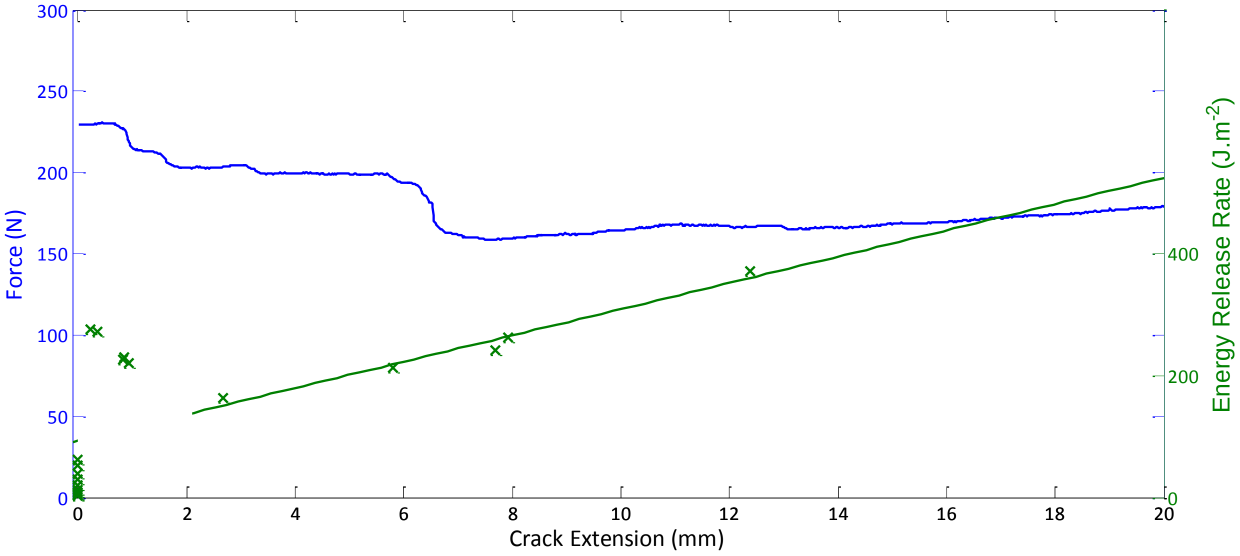

Figure 4.2.4: Graph of the force and energy release rate as a function of crack extension, for a specimen with a high crack initiation force

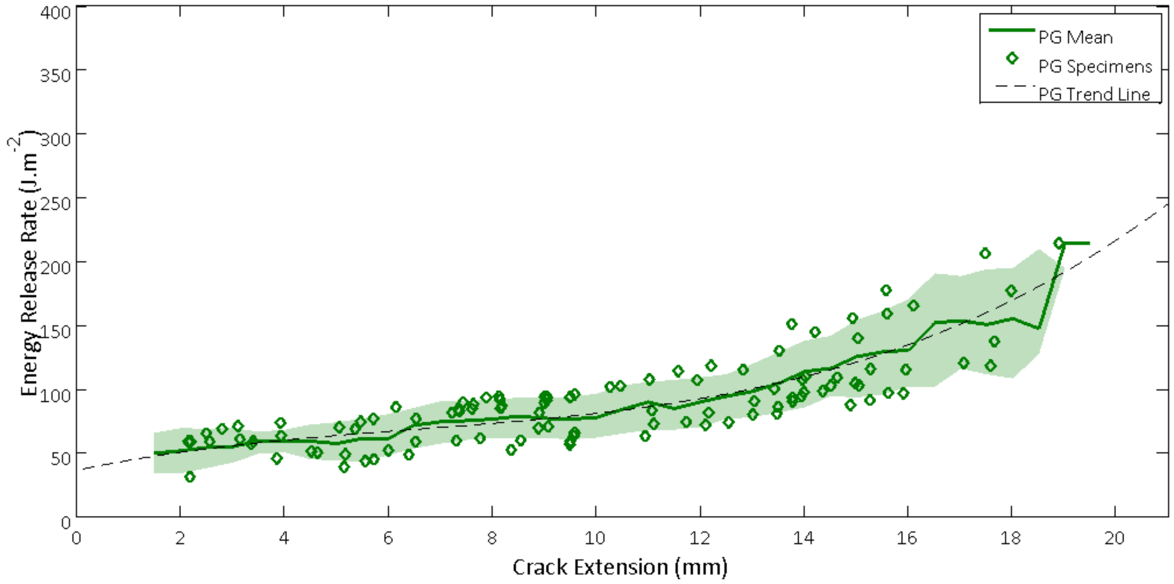

Figure 4.2.5: The stable propagation energy release rate of all the PG specimens

A graph of the energy release rates versus their crack extensions is shown for the Prime 20 LV and bead-blasted (PG) series of specimens in Figure 4.2.5. The $G_{I\text{-}II}$ average for all the specimens was modelled by a third order polynomial, depicted by the trend line in the figure, as opposed to the linear $G_{I\text{-}II}$ curves of the individual specimens. The mean was determined from the average energy release rate for each given interval of crack extension. The shaded area representing the standard deviation was low for the majority of the crack propagation, but from 14mm of crack extension the variation increased for most specimens. The increase in variation could have been from a decrease in the number of data points towards the end of crack extension. For this reason, the energy release rate results were only considered up to 14mm crack extension.

There was considerable scatter present in the individual tests which was expected due to the nature of the test methodology. Some scatter could be attributed to variation in the thickness of the upper leg [103]. Variation in the initial crack length may also have contributed to the scatter as it was difficult to place the specimens at the exact position with high accuracy. Scatter at higher force ranges was compounded because the force value was squared in the calculation of the energy release rate.

The maximum force, force at crack initiation, energy release rate at crack initiation and the crack growth rate of all the specimen series are listed in Table 4.2.2. A high force and energy release rate at crack initiation was indicative of a stronger adhesive interface and a low crack growth rate was indicative of a strong adhesive interface and a high resistance to crack growth. The highest energy release rate at crack initiation was the bead-blasted specimen with SE 84 LV resin and the Redux 609 film adhesive (SGR), while the lowest energy release rate at crack initiation were the alodined specimens produced with SE 84 LV resin (SL). The SGR specimens had the lowest crack growth rate, where the etched and anodised specimens produced with Prime 20 LV had the highest crack growth rate. The treatments were listed in order of decreasing energy release rate.

Table 4.2.2: Summary of the results from all the specimen series

	Max Force(N)		**Crack Initiation Force** (N)		**Energy Release Rate** (J.m^{-2})		**Crack Growth Rate**(mm.min^{-1})	
	Mean	**Standard deviation**	**Mean**	**Standard deviation**	**Mean**	**Standard deviation**	**Mean**	**Standard deviation**
PGS	256.8	31.5	102.8	9.8	361.6	84.7	13.8	4.8
PGES	302.7	47.6	96.0	9.1	306.9	159.0	9.3	3.6
SGR	389.5	68.2	90.9	7.8	896.0	308.3	5.2	1.7
SLR	124.9	8.8	90.2	3.9	93.8	24.5	25.9	11.4
PLR	289.1	37. 7	87.7	8.4	98.7	43.4	13.1	2.9
PGR	97.8	7.3	81.4	8.9	79.0	8.4	20.7	3.7
PGEN	151.6	23.8	78.0	14.8	97.1	36.5	17.8	4.6
PGE	143.6	21.1	71.4	15.4	60.7	35.6	17.1	4.3
SL	76.0	18.6	66.7	26.4	29.1	10.0	31.2	6.3
PEN	91.1	14.3	66.1	13.4	38.5	5.2	32.0	10.2
PG	85.0	14.0	55.7	4.3	46.5	19.2	18.9	4.8

4.2.2. THE EFFECT OF MECHANICAL SURFACE TREATMENTS

Results of SLB tests for alodined (PL), Bead-blasted (PG), etched and anodised (PEN) and bead-blasted, etched and anodised (PGEN) adhesive surfaces were compared to determine the influence of micro- and macro-roughness on adhesive performance. Figure 4.2.6 is a plot of the mean $G_{I\text{-}II}$ values of the PG, PEN and PGEN specimens as a function of their crack lengths, with their standard deviations represented by the shaded areas. The PG specimens were macro-roughened (bead-blasted); the PEN specimens were micro-roughened (etched and anodised) and the PGEN specimens were both micro- and macro-roughened. The PL specimens were simply alodined and not roughened at all. These specimens did not provide adequate adhesion as the specimens failed during compliance testing and were therefore not shown in the figure.

The PG, PEN and PGEN mean energy release rate slopes increased with crack extension. PG and PEN exhibited a narrow initial standard deviation which widened towards the end of crack growth. The PGEN series had a broader standard deviation from the mean which narrowed towards the end of crack propagation.

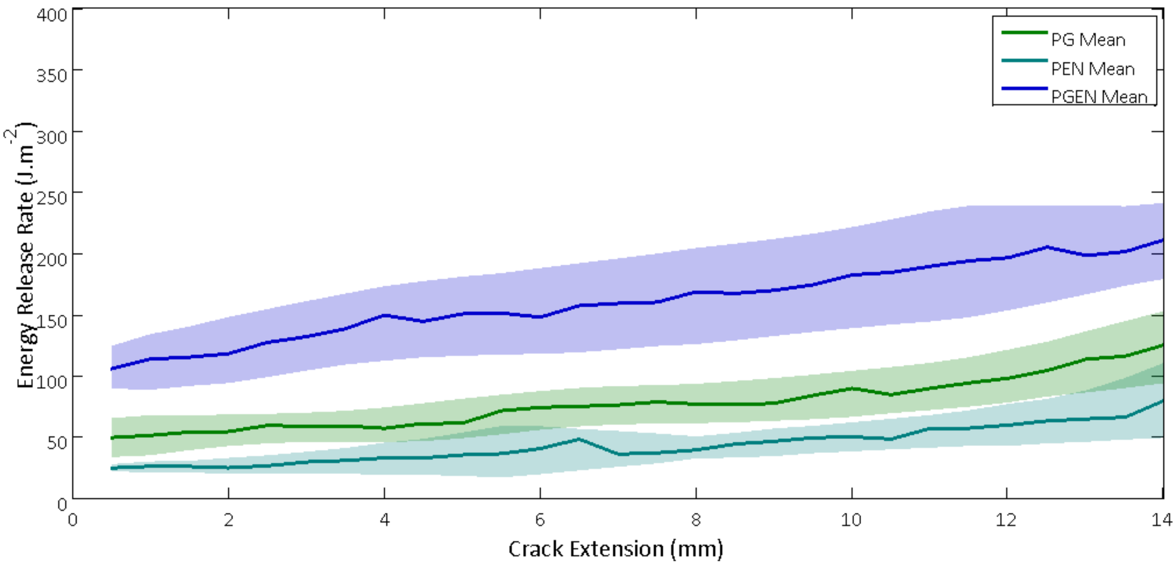

Figure 4.2.6: The stable propagation energy release rates of specimens with different surface morphologies

Figure 4.2.6 demonstrated that the PGEN specimens had a significantly higher stable propagation energy release rate than both the PEN and PG specimens. This was supported by a significantly higher peak force, force at crack initiation and energy release rate at crack initiation as listed in Table 4.2.2. The crack growth rates of the PG and PGEN were comparable and significantly lower than that of the PEN specimens. The macro-roughened specimens (PG and PGEN) had lower crack growth rates, suggesting that the micro-roughness contributed to a higher force at crack initiation in conjunction with the chemical surface treatment. Superior adhesion was achieved when micro and macro abrasion were combined.

4.2.3. THE EFFECT OF CHEMICAL SURFACE TREATMENTS

Bead-blasted (PG), bead-blasted and etched (PGE) and bead-blasted, etched and anodised (PGEN) SLB specimens were tested and compared to experimental silane surface treatments which were bead-blasted and silane treated specimens (PGS) as well as bead-blasted, etched and silane treated specimens (PGES). The stable propagation energy release rate results of the different chemical surface treatments are plotted as a function of crack growth in Figure 4.2.7.

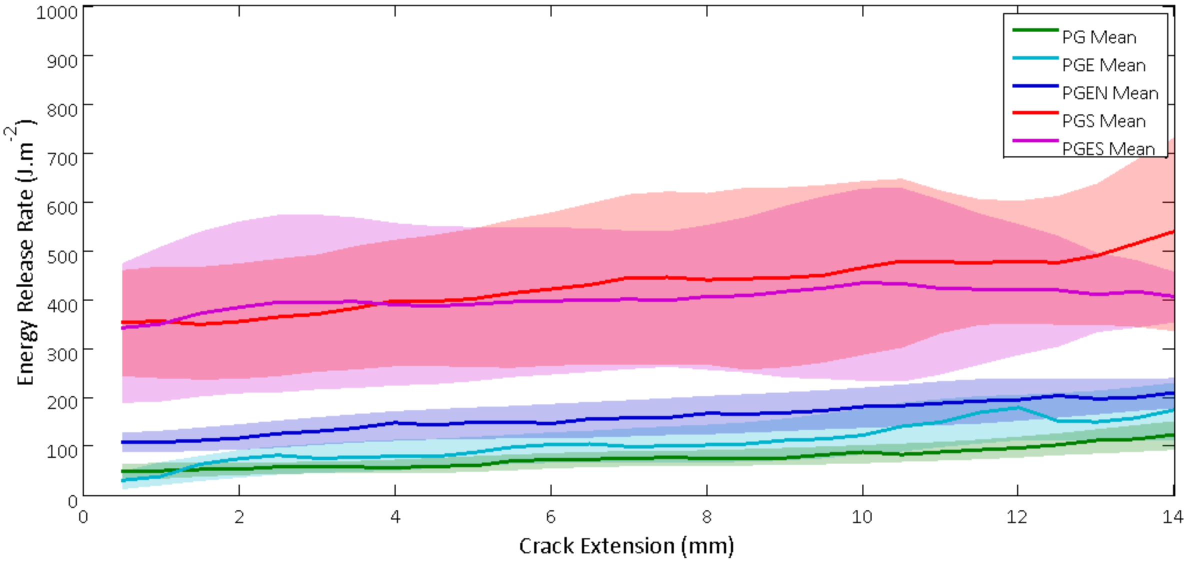

Figure 4.2.7: The stable propagation energy release rate of specimens treated with different chemical surface treatments.

The PG specimens were not chemically treated and therefore were included as the control. The PG series demonstrated the lowest stable propagation energy release rate and the highest crack growth rate and could therefore be regarded as the weakest in this comparison.

There was significant scatter and overlap between the PGE and PGEN specimens and between the PGS and PGES specimens. The silane specimens (PGS and PGES) however, clearly performed better than the specimens with the standard aluminium surface treatments (PGE and PGEN). Both PGS and PGES had large standard deviations from the mean, narrowing towards the end of the crack propagation. The PGES series had a lower crack growth rate; whereas the PGS series had a more pronounced and relatively linear increase in the G_{I-II} mean. The PGS specimens demonstrated a better adhesive performance than those of PGES.

Graphs of the energy release rates versus crack extension, for the PGE and PGEN specimens were shown on a smaller scale in Figure 4.2.8. The energy release rate of PGE and PGEN both increased relatively linearly with crack extension, however the PGE curve exhibited an inconsistency which could be ascribed to the averaging process. The stable propagation G_{I-II} of PGE, however, had a marginally higher increase in G_{I-II} as a function of crack growth as the mean could be seen to approach that of PGEN. The overlap of the shaded areas increased with crack extension, but the mean curves did not intersect The PGEN specimens maintained a higher stable propagation energy release rate and the PGEN provided better adhesion performance than PGE.

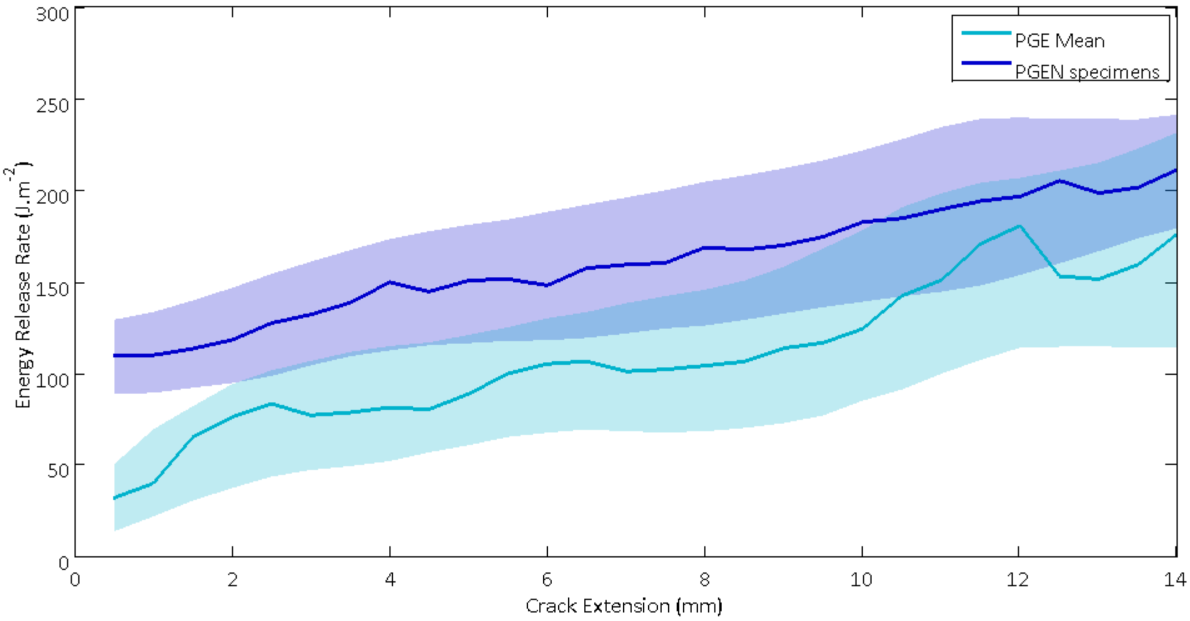

Figure 4.2.8: The stable propagation energy release rate of etched (PGE) and anodised (PGEN) specimens.

The chemical surface treatments were tested and compared. It was observed that the silane treatments performed substantially better than the standard surface treatments, with the bead-blasted and silane treated specimens (PGS) performing the best. The standard surface treatments performed as expected with the bead-blasted specimens (PG) having the weakest adhesion and the anodised specimens (PGEN) the highest.

4.2.4. RESIN PERFORMANCE

The adhesive performance of the Prime 20 LV resin was compared to that of the SE 84 LV resin with which the prepreg sheets were impregnated. The stable propagation $G_{I\text{-}II}$ of alodined specimens manufactured with Prime 20 LV (PL) and SE 84 LV (SL) were presented in Figure 4.2.9. Results were only obtained from four SL specimens exhibiting considerable scatter therefore each specimen was represented by an individual trend line as opposed to a single line representing the mean. The alodined, Prime 20 LV (PL) specimens did not produce results because the specimens failed during compliance testing; therefore the prepreg specimens performed better by default, regardless of the scatter.

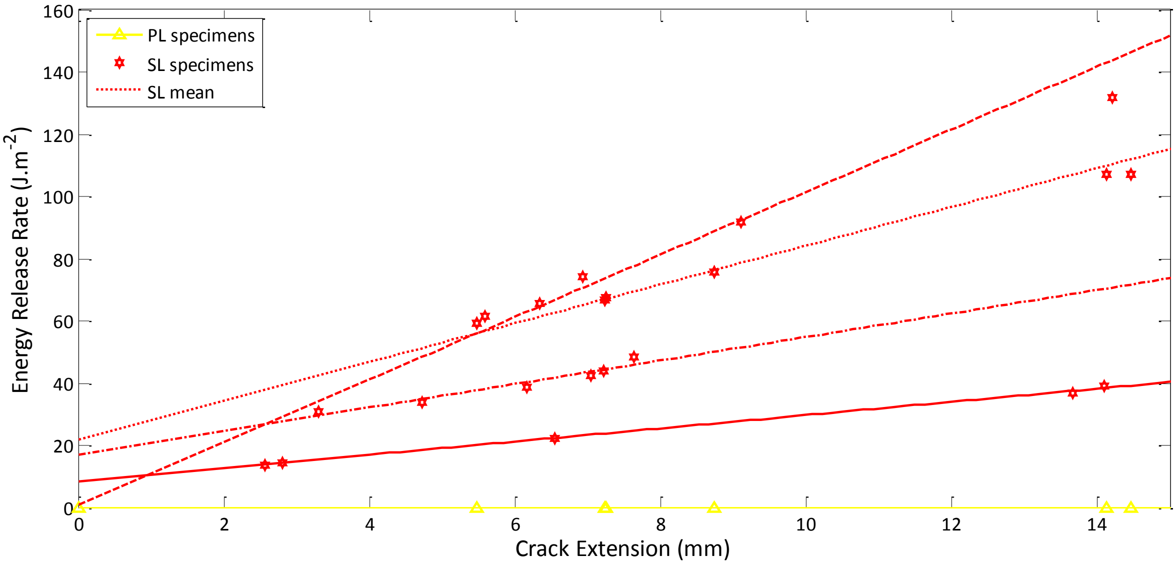

Figure 4.2.9: The stable propagation energy release rates of alodined specimens bonded with Prime 20 LV resins (PL) and with SE 84 LV resin (SL)

The adhesion and stable propagation energy release rates of Prime 20 LV (PGR) and SE 84 LV (SGR) resins bonded to bead-blasted and film-adhered surfaces were compared in Figure 4.2.10. The SGR specimens exhibited an energy release rate that was an order of magnitude higher than those of the PGR specimens. The SGR series had a considerable amount of scatter; however the specimens on the lower bound still outperformed those of PGR by a large margin. The PGR specimens had some scatter, but the standard deviation was not visible on this scale. The SGR specimens had a very high initial energy release value and a very low crack growth rate compared to PGR, both of which are documented in Table 4.2.2.

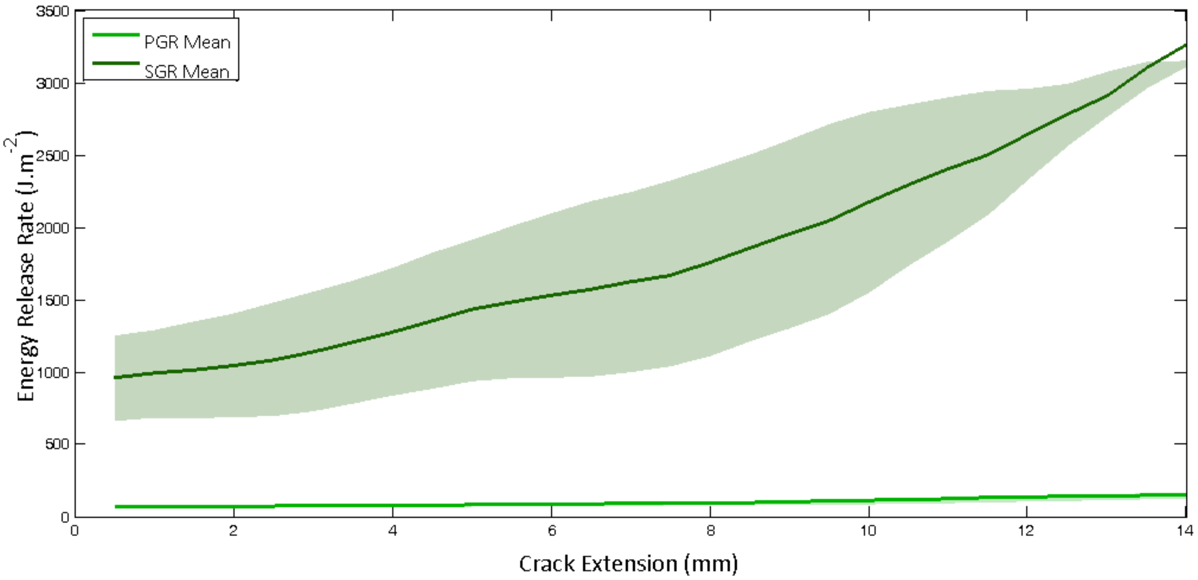

Figure 4.2.10: The stable propagation energy release rate of bead-blasted specimens bonded with Prime 20 LV (PGR) and SE 84 LV resin (SGR), both including a film adhesive

The aluminium failure surfaces of PGR and SGR specimens are shown in Figure 4.2.11(a) and (b) respectively. The film adhesive was still attached to aluminium surface of the PGR specimen and trace amounts of film adhesive remained on the aluminium surface of the SGR specimen. The Redux 609 / Prime 20 LV bond therefore failed before the Redux 609 / aluminium bond, whereas the Redux 609 / SE 84 LV bond of the SGR specimens outperformed the Redux 609 / aluminium bond. This verified that the performance of the SE 84 LV resin with the Redux 609 film adhesive was superior to that of the Prime 20 LV resin. The GFRP bonding surface of a SGR specimen is shown in Figure 4.2.11(c) which indicated that the film adhesive remained bonded to the GFRP, but also exhibited aluminium oxide on the film adhesive surface. This indicated that the SE 84 LV-Redux 609 and Redux 609-bead-blasted surface bond strengths exceeded that between the aluminium alloy and the aluminium oxides on the surface.

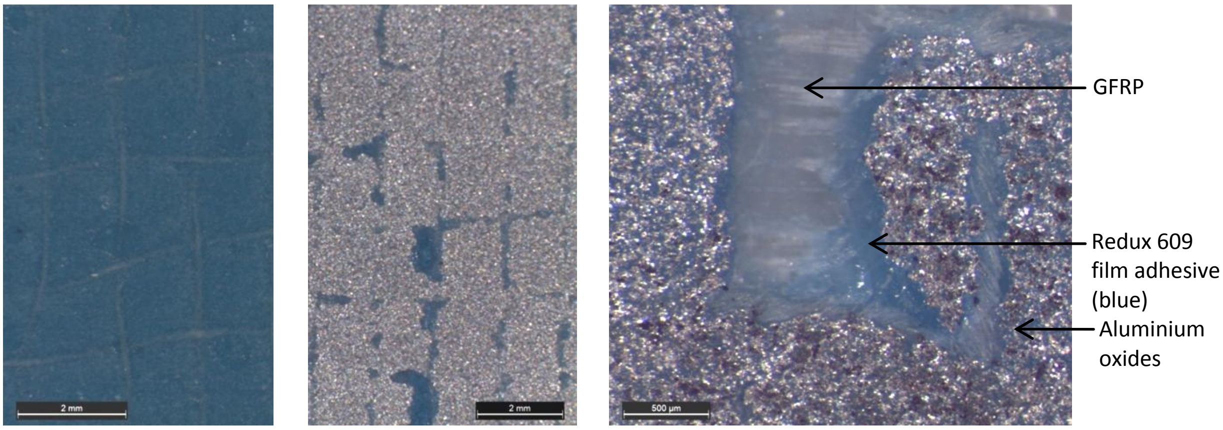

Figure 4.2.11: Microscopic images of the aluminium surfaces of (a) PGR specimens and (b) SGR specimens and the (c) GFRP bonding surface of a SGR specimen

The performance of Redux 609 / alodined specimens bonded with Prime 20 LV and the SE 84 LV resins are compared in Figure 4.2.12. The energy release rate of the specimens bonded with Prime 20 LV (PLR) increased significantly more with crack extension than those bonded with SE 84 LV (SLR), which was contradictory to expectations. Upon investigation of the adhesive interfaces, both specimens failed between the Redux 609 film adhesive and the aluminium. This suggested that the bond between the film adhesive and the alodined surface was weaker than the bond between the film adhesive and either resin, which consequently meant that the curves should have lain on top of each other. Considering that both the PLR and SLR specimens failed between the alodined aluminium and the Redux 609 film adhesive, it is expected that the interfaces that were tested should have been of similar strength producing overlapping energy release rate curves.

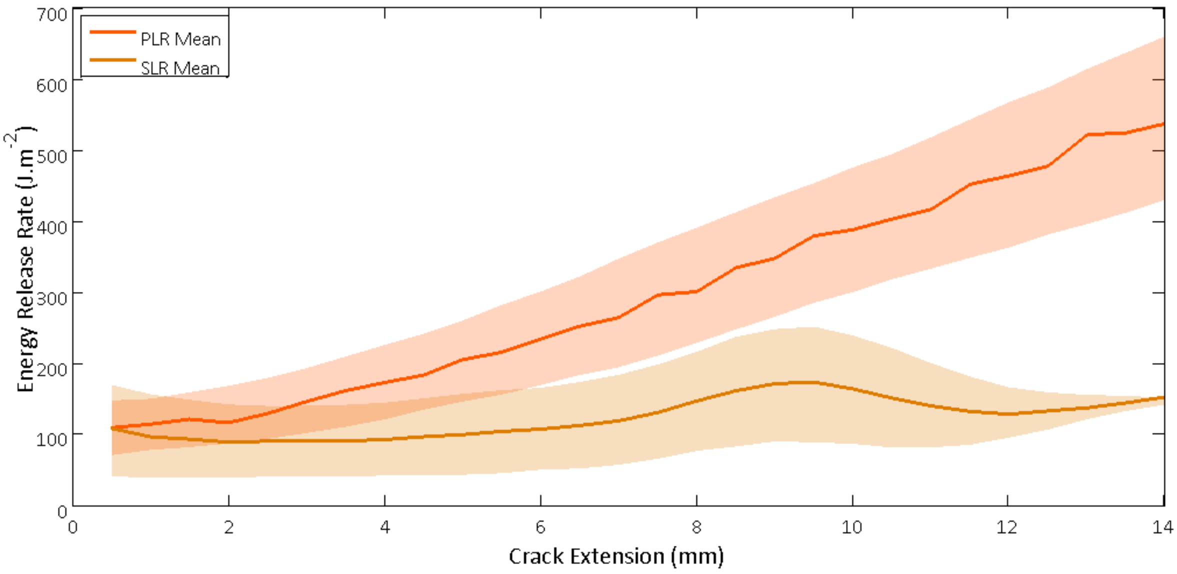

Figure 4.2.12: The stable propagation energy release rate of alodined specimens that were adhered with Prime 20 LV (PLR) and SE 84 LV resin (SLR), both including a film adhesive

The alodined aluminium surfaces of a SE 84 LV specimen and a Prime 20 LV specimen were shown in Figure 4.2.13 (a) and (b) respectively. The pre-existing flaws were indicated where non-porous release films were inserted between the film adhesive and the GFRP and where the film adhesive remained bonded to the aluminium for both the PLR and SLR specimens. At the edge of the pre-existing flaw, which was also the tip of the initial crack, the SLR specimen exhibited a distinct break in the film adhesive, where the film adhesive was then bonded to the GFRP. The supportive scrim within the film adhesive of the PLR specimen remained anchored to the aluminium by the film adhesive within the pre-existing flaw, but from the tip of the initial crack the scrim and film adhesive were bonded to the GFRP which is shown in Figure 4.2.13(c). Upon inspection it was suspected that additional failure occurred within the film adhesive of the PLR specimens as some of the resin remained bonded to the aluminium and some bonded to the GFRP. This additional mode of failure could explain the higher energy release rate of the PLR specimens compared to the SLR specimens.

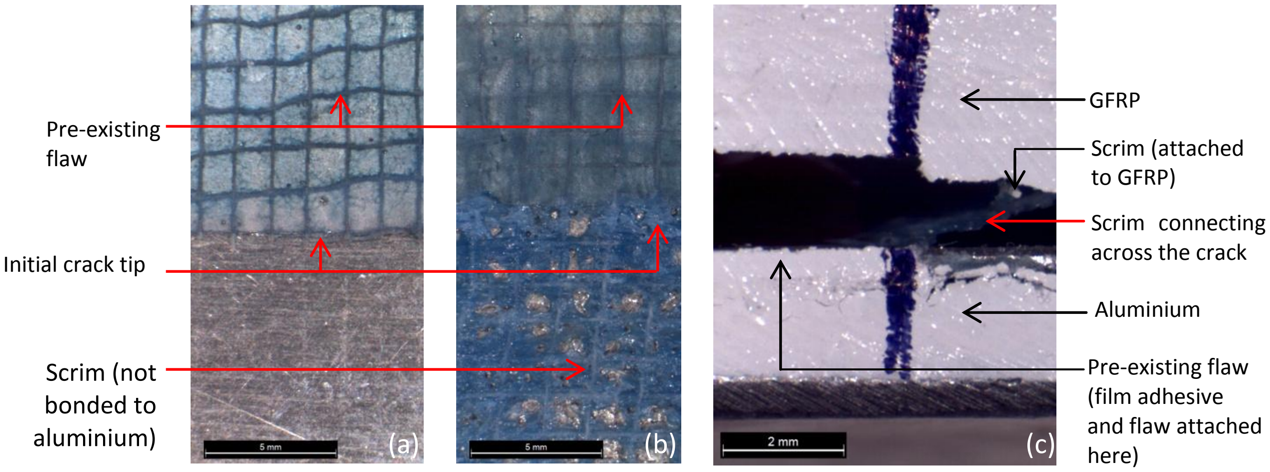

Figure 4.2.13: The alodined aluminium interfaces of the (a) SLR and (b) PLR specimens and (c) the scrim between the aluminium and GFRP interfaces

Prime 20 LV has shown adequate adhesion as all specimens (excluding PL) have shown constant crack growth, but when directly compared to SE 84 LV, the SE 84 LV resin maintained a significantly higher energy release at crack initiation and throughout crack extension. The PLR specimens appeared to be an exception with an unusually high energy release rate, but this was suspected to be due to failure within the film adhesive.

4.2.5. FILM ADHESIVE PERFORMANCE

The adhesive performance of thermoset film adhesives were evaluated by comparing the performance of bead-blasted (PG) and alodined (PL) surfaces to the respective surfaces enhanced by a Redux 609 film adhesive (PGR and PLR). The comparison based on the energy release rates are plotted in Figure 4.2.14. The inclusion of a film adhesive increased the number of adhesive interfaces at which the crack growth could occur. The pre-existing crack was inserted between the film adhesive and the GFRP, however in general the weakest adhesive interface would fail.

The alodined specimens with the film adhesive performed better than those without the film adhesive, as the PL specimens failed during compliance testing and are represented as $G_{I\text{-}II} = 0$. The energy release rate of the bead-blasted specimens increased with crack extension. The PGR specimens maintained a slightly higher $G_{I\text{-}II}$ for the duration of crack extension and therefore demonstrated that the film adhesive improved the adhesion performance of the bead-blasted specimens.

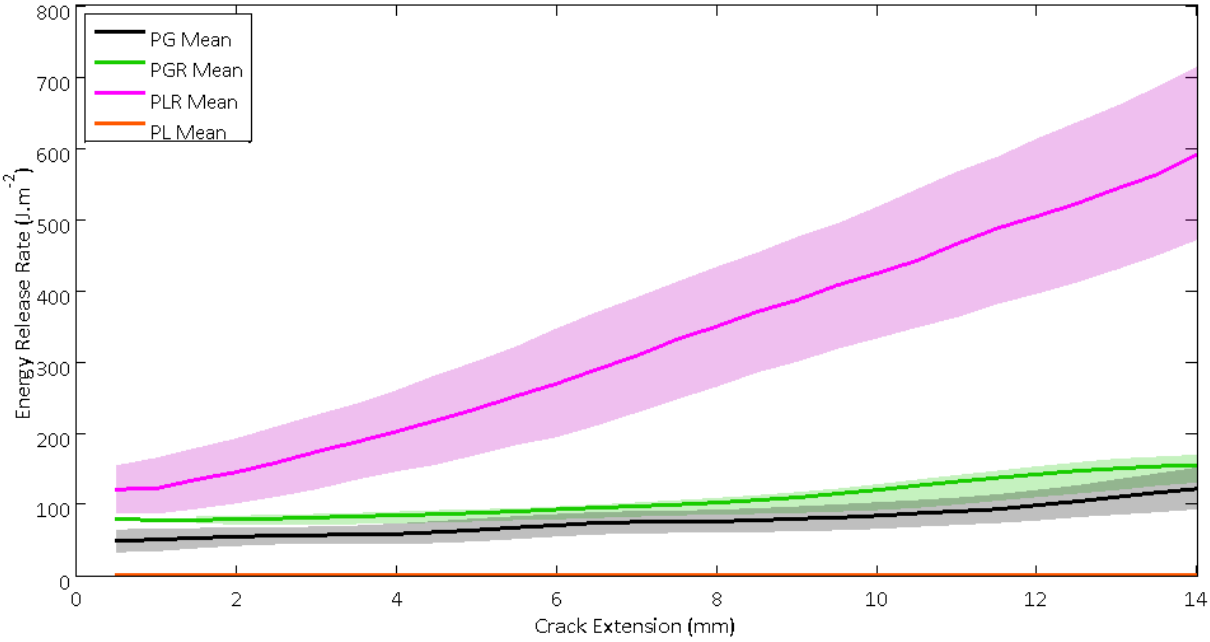

Figure 4.2.14: The stable propagation energy release rate of SLB specimens bonded with a film adhesive (PGR and PLR) and without film adhesives (PG and PL).

The alodined specimens provided a weaker adhesive interface than the bead-blasted specimens, however the alodined specimens with the film adhesive performed significantly better than the bead-blasted specimens with the film adhesive. These differences could be ascribed to the specimens failing at different adhesive interfaces. The aluminium and GFRP adhesive surfaces of the SLB specimens were inspected under a microscope and the images are shown in Figure 4.2.15.

Debonding in the PLR specimen occurred between the alodined aluminium and the film adhesive as the film adhesive remained attached to the glass fibre. The high energy release rates of the PLR specimens have been attributed to failure within the film adhesive as discussed in the previous section. The PGR specimens exhibited debonding between the film adhesive and the GFRP as the film adhesive remained bonded to the bead-blasted aluminium. The reason for this was not known, but it did contribute to the deduction that the Prime 20 LV was a weaker resin than the SE 84 LV.

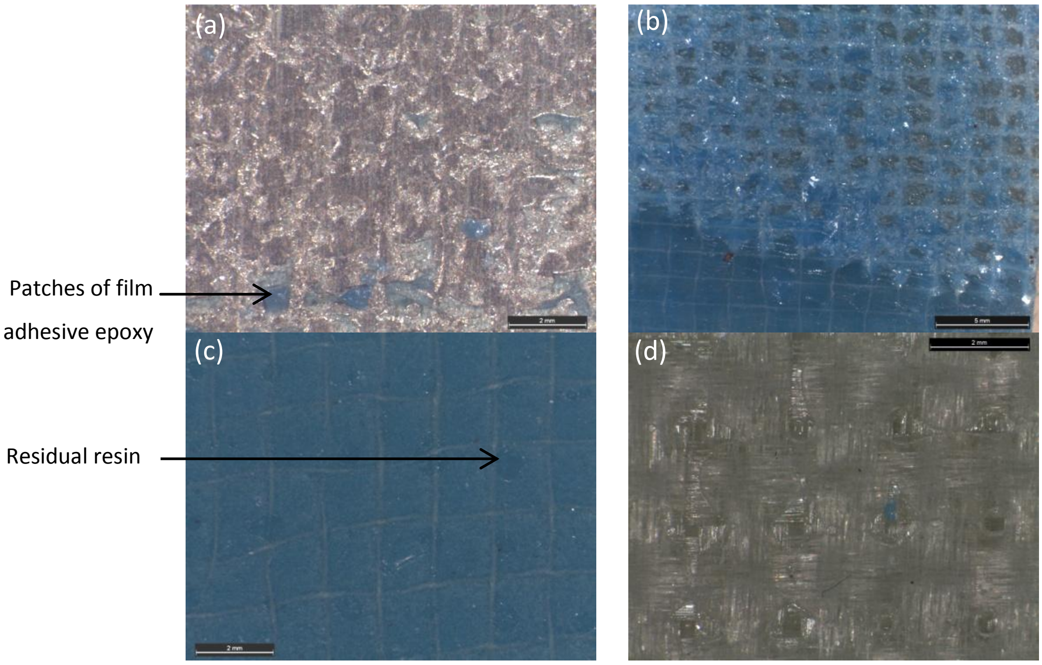

Figure 4.2.15: The adhesive interfaces of SLB specimens: (a) the aluminium surface of PLR, (b) the GFRP interface of PLR, (c) the aluminium surface of PGR, and (d) the GFRP surface of PGR

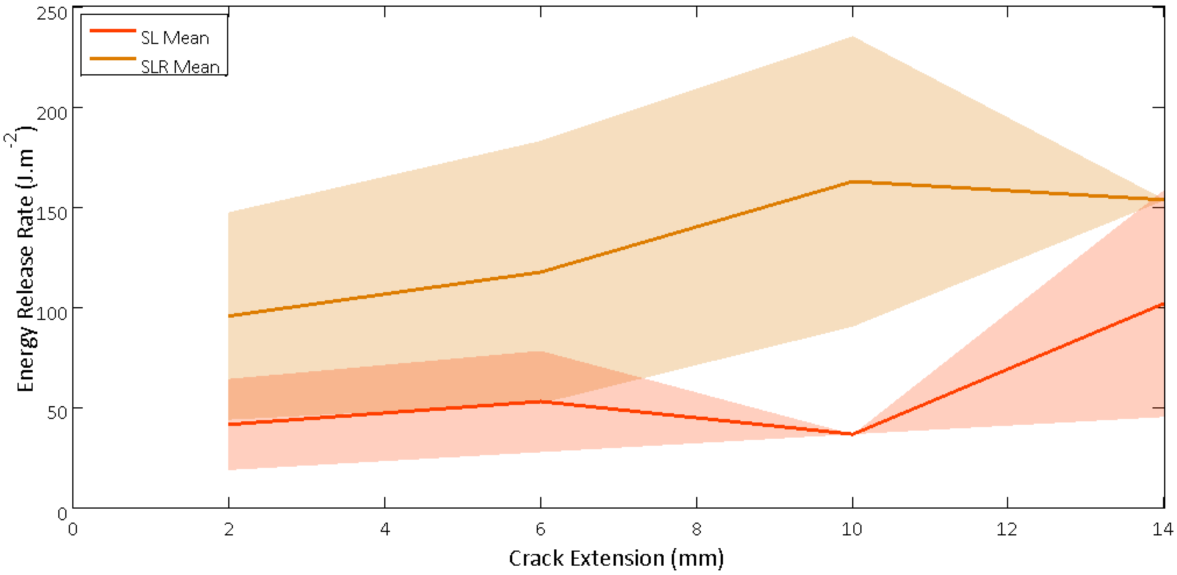

Figure 4.2.16: The stable propagation energy release rates of prepreg specimens with (SLR) and without (SL) a film adhesive.

The energy release rate of an alodined surface (SL) is compared to an alodined surface modified with a film adhesive (SLR) in Figure 4.2.16. The SLR series exhibited a significantly larger standard deviation than the SL series, and overlapped with the standard deviation of the SL series in isolated cases. It should be noted that small quantities of data could mean that a comparison of standard deviations could be misleading, for example the standard deviation of the SL series was zero at c_{ext}=10mm as there was a single data point in that interval of crack extension. The SLR specimens consistently performed better than those of the SL series as demonstrated by a higher energy release rate, a higher initial energy release rate at crack initiation and a lower crack growth rate. Both mean curves appeared to deviate from the typical linear increase in the energy release rate, but the deviations may have been caused by the low number of data points in some regions. The linear increase in the energy release rate of the individual specimens is shown in Figure A.1.2 in Appendix A.1.

The specimens that were modified with the Redux 609 film adhesive (PGR, PLR and SLR) all performed better than their counterparts without the film adhesive (PG, PL and SL). The use of a film adhesive therefore improved the adhesion of the metal surface to thermoset resins.

4.3. SUMMARY OF TEST RESULTS

The adhesive performance of several adhesive interfaces was evaluated using the data obtained from Single Leg Bend tests. The SLB tests produced viable results for most cases with stable crack growth at relatively constant forces which is summarised in Table 4.3.1. The results obtained from the series comparisons were:

- Adhesive surfaces that were both micro- and macro- roughened produced better adhesive surfaces than those that were only micro-, or macro-roughened or not roughened at all.
- The bead-blasting and silane treatment combination produced the strongest adhesive bonds of all the chemical surface treatments with an energy release rate of 361.6J.m^{-2} and a force of 102.8N at crack initiation. Throughout crack propagation the specimens maintained the highest stable propagation energy release rate.
- The SE 84 LV prepreg resin demonstrated better adhesion than the Prime 20 LV resin, having an energy release rate an order of magnitude higher.
- The inclusion of the Redux 609 film adhesive improved the performance of all adhesive interfaces.

Table 4.3.1: Summary of the results of all the specimen series

	Crack Initiation Force (N)		**Energy Release Rate** (J.m^{-2})		**Crack Growth Rate**(mm.min^{-1})		**Ranking**
	Mean	**Standard deviation**	**Mean**	**Standard deviation**	**Mean**	**Standard deviation**	
SGR	90.9	7.8	896.0	308.3	5.2	1.7	1
PGS	102.8	9.8	361.6	84.7	13.8	4.8	2
PGES	96.0	9.1	306.9	159.0	9.3	3.6	3
PLR	87.7	8.4	98.8	43.4	13.1	2.9	4
PGEN	78.0	14.8	97.1	36.5	17.8	4.6	
SLR	90.2	3.9	93.8	24.5	25.9	11.4	
PGR	81.4	8.9	79.0	8.4	20.7	3.7	
PGE	71.4	15.4	60.7	35.6	17.1	4.3	
PG	55.7	4.3	46.5	19.2	18.9	4.8	
PEN	66.1	13.4	38.5	5.2	32.0	10.2	
SL	66.7	26.4	29.1	10.0	31.2	6.3	

The best adhesive interface that was achieved was the bead-blasted aluminium bonded with the Redux 609 film adhesive and the SE 84 LV prepreg resin (SGR). The SGR specimens had the highest energy release rate, the highest energy release rate at crack initiation and the lowest crack growth rate by a significant margin. The mode of failure at the interface was especially significant as debonding did not occur, but rather failure occurred between the aluminium alloy and the aluminium surface oxides, which can be seen in Figure 4.3.1(c). The next best adhesive interface was the bead-blasted and silane treated aluminium bonded to the GFRP with Prime 20 LV (GPS). The energy release rates of the SGR and the PGS series are plotted in Figure 4.3.1, which emphasizes the significantly superior performance of the SGR series.

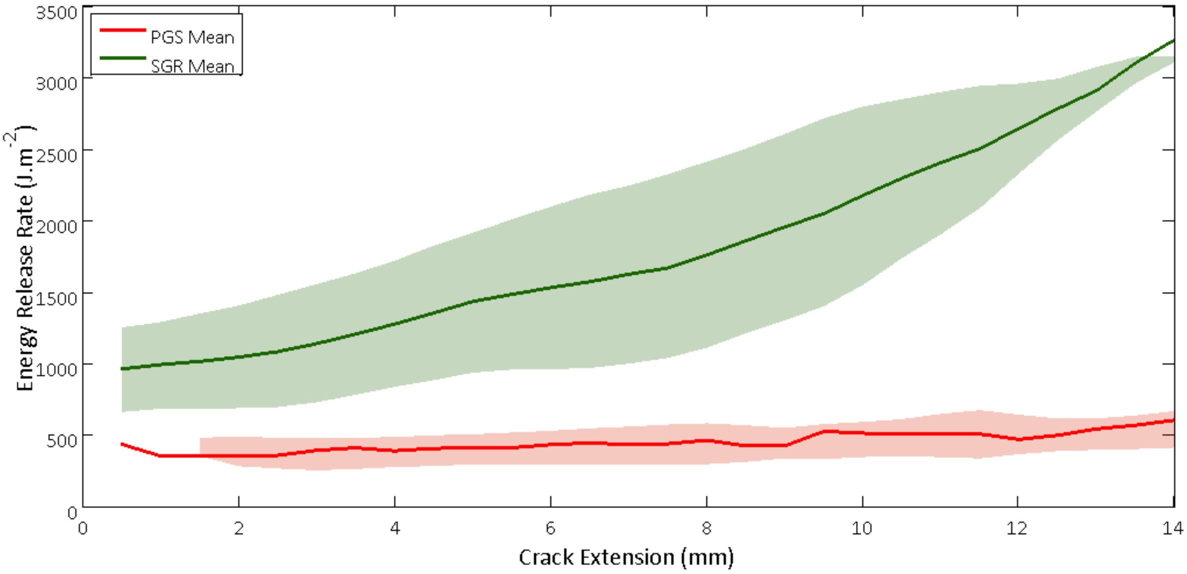

Figure 4.3.1: A comparison of the best (SGR) and the second best (PGS) performing adhesive interfaces

4.4. DISCUSSION

4.4.1. COMPARISON OF BEAD-BLASTING AND ETCHING PRIOR TO SILANE TREATING

The bead-blasted and then etched SLB specimens provided higher fracture toughness than the SLB specimens of which the aluminium was bead-blasted only. It was proposed that etching the aluminium prior to bead-blasting would improve the adhesive performance of the silane coupling agent by increasing the number of available metal hydroxides on the surface [83]. ADCB wedge tests performed by Liu et al [63] supported this. The SLB specimens that were only bead-blasted prior to the silane treatment (PGS) however had a higher energy release rate at crack initiation and throughout crack propagation compared to those that were bead-blasted and etched (PGES) before being silane treated, which was contrary to expectation.

ADCB [63] and RDCB [84] wedge test results reported that bead-blasted and silane treated surfaces had higher fracture toughness than surfaces that were only etched (and not bead-blasted) prior to the silane treatment. This correlated to the macro-roughened (PG) specimens providing better fracture resistance than the micro-roughened specimens (PEN) in the SLB tests. However, the etched surfaces provided a higher threshold (initiation) energy release rate than the bead-blasted specimens despite the bead-blasting generating a rougher surface [63]. It was speculated that the higher fracture toughness of the PGS specimens in this study could have been ascribed to the SLB test method being more sensitive to surface roughness (mixed mode -G_{II}/G_{tot} ratio 0.4 [64]) compared to the wedge tests (Mode I).

4.4.2. COMPARISON OF SILANE TREATMENTS TO ANODISING

The anodising technique that was utilised in this study was sulphuric acid anodising, which was comparable to CAA/PAA in adhesive strength, but had a reduced corrosion resistance [75]. As corrosion resistance was not considered in the present study, the sulphuric acid anodising served as a suitable measure for comparison. The fracture toughness of the bead-blasted and then silane treated specimens was significantly higher than that of the anodised SLB specimens with a G_{CI} value four times that of the anodised (PGEN) specimens. Results in literature have typically shown anodised and silane treated surfaces to perform within a closer range [64]. The surface morphology and low pore density described in Section 6.2.1 may have been the reason for the less than typical fracture toughness of the anodised specimens.

4.4.3. REDUX 609 PERFORMANCE

The combination of bead-blasting, Redux 609 film adhesive and the SE 84 LV prepreg resin (SGR) produced the toughest SLB adhesive interface with an energy release rate at crack initiation of 896J.m^{-2}. The only energy release rate reported for GLARE is 1100J.m^{-2} which was used in a numerical study [132]. The energy release rate of the SGR exceeded that of GLARE during crack growth suggesting that the performance of this combination of resin and surface treatments approaches the performance of the metal-epoxy adhesive interface in GLARE.

4.4.4. GENERAL OBSERVATIONS

The energy release rate was seen to increase steadily with crack extension in each experiment. No plastic deformation of the specimens was observed. The utilisation of compliance calibrations should have accounted for any variations due to compliance. The cause for this increase is unknown, however has been observed in other work [103].

CHAPTER 5: IMPACT LOADING

The impact resistance of FMLs with different aluminium surface treatments was investigated by considering the failure of the different metal-GFRP interfaces within impact tested FMLs. Three different surface treatments were considered based on the SLB test results presented in Chapter 4. It was determined in Chapter 4 that bead-blasted aluminium bonded to the SE 84 LV resin prepreg with a Redux 609 film adhesive provided the best adhesive interface. The anodised and silane treatments performed better than the bead-blasted surface when bonded to Prime 20 LV, therefore anodised and silane-treated aluminium surfaces combined with the film adhesive had the potential to exceed the fracture toughness of the SGR specimens. In this chapter, FMLs manufactured with these aluminium surface preparations, film adhesive and prepreg were tested under impact loading conditions. The silane surface treatment was of particular interest due to the energy dissipation potential of the silane network in combination with chemical etching which was suggested to contribute to the adhesive ability. The surface treatments are summarised in Table 5.1.1.

Table 5.1: Summary of the surface treatments used for FML impact specimens

Code	Surface Treatments	Film Adhesive	Resin	Equivalent SLB Test code
ISG	Bead-blasted	Redux 609	SE 84 LV	SGR
ISA	Bead-blasted, etched & anodised	Redux 609	SE 84 LV	SGENR*
ISS	Bead-blasted, etched & silane treated	Redux 609	SE 84 LV	SGESR*

*Hypothetical codes as equivalent SLB specimens were not manufactured

Low velocity drop tower impact tests were performed to evaluate which surface treatment exhibited the smallest extent of interfacial debonding. The failure by interfacial adhesion was considered in conjunction with the plastic deformation to determine which surface treatment was able to dissipate the largest amount of energy without debonding.

5.1. EXPERIMENTAL DETAILS

5.1.1. EXPERIMENTAL PROCEDURE

Low velocity impact tests were performed using a drop weight setup on an Instron Dynatup 9210. The tests were performed using a hemispherical indentor (tup) with a diameter of 10mm. The indentor was connected to a 15 kN load cell, as shown in Figure 5.1.1. The specimens were clamped in a square steel frame which was screwed on to a base platform. There were no devices that caught the indentor in the event of a rebound, but emergency stoppers as shown in Figure 5.1.1 prevented the tup and load cell from striking the base of the impact rig when passing through the specimen.

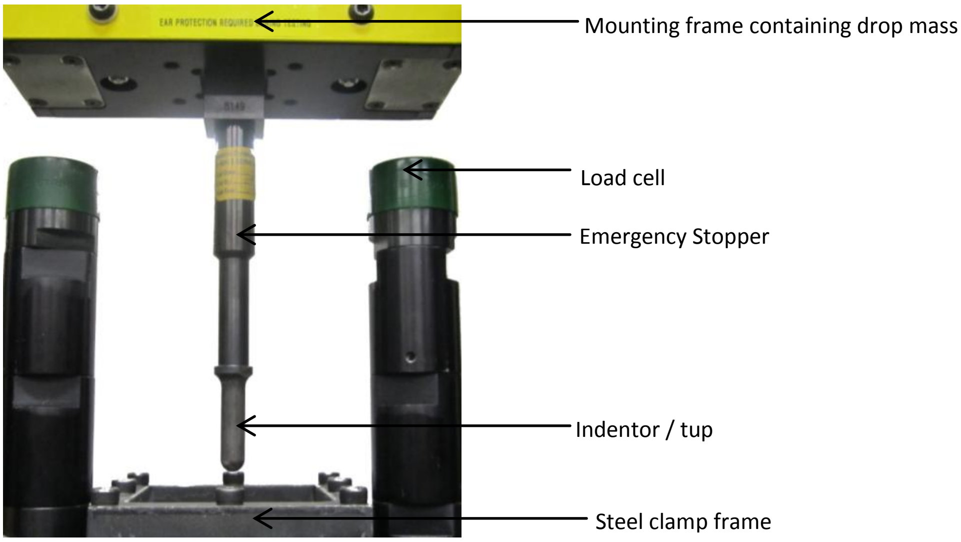

Figure 5.1.1: Low velocity drop weight setup

The drop weight mass was held constant for all tests at 6,076kg which included the mass of the tup, load cell and mounting frame. The drop height was varied over a range of 0.4 – 0.8 metres to obtain impact energies in the range of 20J – 40J. The mass was released by an automatic trigger and each specimen was subjected to a single impact event in which the indentor punctured all three aluminium layers of the specimen. A speed trap determined the impact velocity and Instron's "Impulse Acquisition" software was used for data capture and MATLAB for analysis.

5.1.2. DATA ANALYSIS

Ultrasonic inspection or C-scanning of FMLs was not a viable (non-destructive) technique to measure the internal damage of FMLs as the plastic deformed dent scatters the ultrasonic signal disrupting ultra-sonic measurements [103, 133]. The impedance mismatch at the interfaces between the layers is an inherent issue that limits the penetration depth of the C-scan technique [134]. The 3D scanning was used as a non-destructive method to analyse the deflection of the impact tested FML panels and to determine the internal damage within the FMLs.

3D SCANNING

The profiles of the impact tested FML panels were scanned in 3D using the Next Engine 3D desktop scanner. Figure 5.1.2a and 5.1.2.b display a photograph of the back face of an impacted specimen and the 3D scan of the same surface respectively, the latter having being generated in the "Next Engine ScanStudio HD" software.

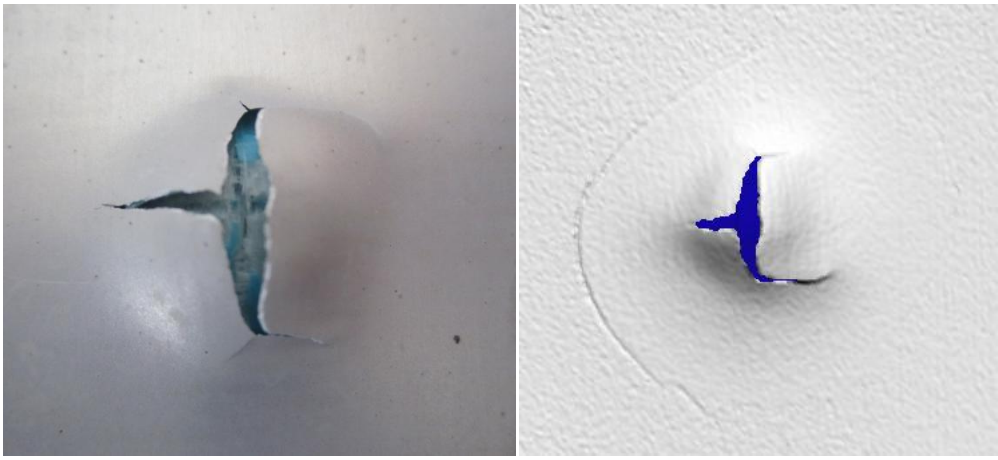

Figure 5.1.2: (a) A photograph of the distal face of an impact tested specimen ISA 6 and (b) a three-dimensional scan of the same specimen

Each scan generated x, y and z data points representing the 3D surface. Deflection profiles were created for each specimen by fitting a surface to the scanned data; a typical deflection plot is shown in Figure 5.1.3.

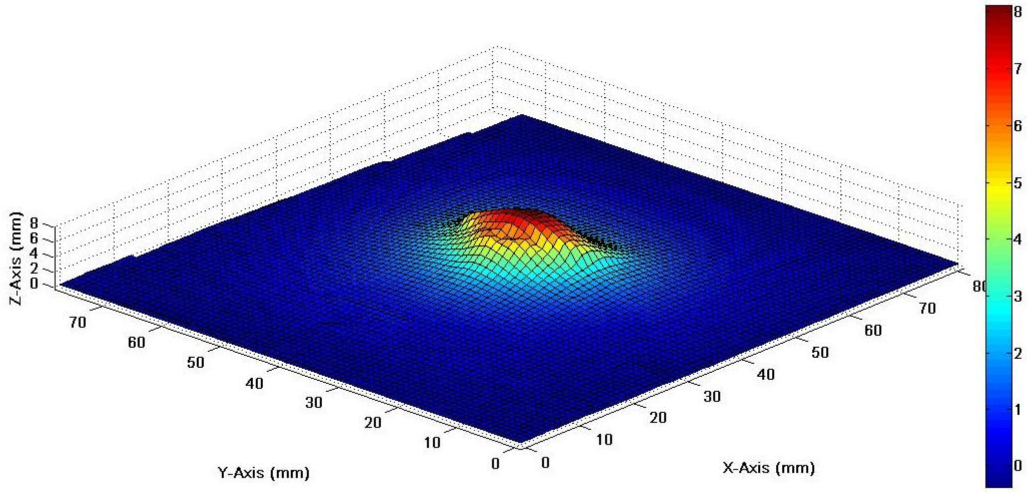

Figure 5.1.3: A typical surface deflection plot produced from 3D surface scan data

The separation zone was a representative measure of the separation that occurred between the distal and the proximal side of the FML. The separation zone was a measure of the total permanent internal damage that occurred between the outer skins including any interlaminar delamination, ply-splitting, fibre breakage, interfacial debonding, plastic deformation and rupture etc. Figure 5.1.4 shows the deflection of the impacted side (proximal face) in red and the side remote from impact (distal face) in blue. The difference between the distal and proximal deflection at each point was the magnitude of the separation at that point.

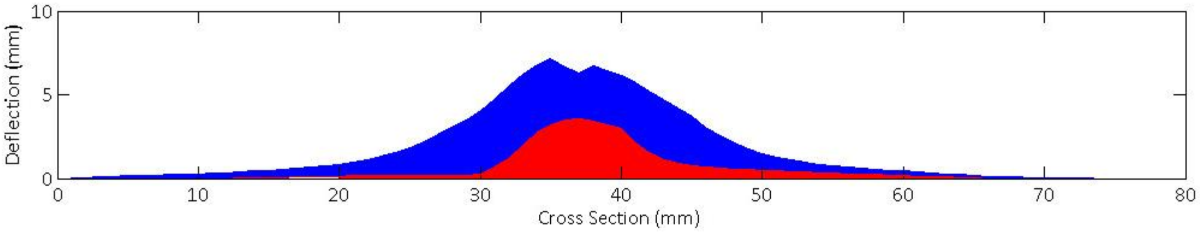

Figure 5.1.4: The deflection profiles of the proximal (red) and distal (blue) face

OPTICAL MICROSCOPY

Optical microscopy was utilized to inspect sectioned FMLs to identify the failure modes that occurred within the separation zone. A Leica MZ 8 microscope was used in conjunction with the Leica Application Suite V3.7.0 software.

5.1.3. DATA PROCESSING: DIMENSIONLESS COMPARISONS

Langdon et al [4] used non-dimensional impulse as a method to compare the blast resistance properties of GLARE to that of mild steel. The plate geometry, material properties and blast loading properties were accounted for, as described in section 2.5. The panel performance measure was defined as the mid-point permanent deflection to thickness ratio. Similar formulations have been used in impact testing to correct either the initial impact velocity or the impact mass in compensation for the response of strain-rate sensitive materials [135]. These scaling laws have been shown to accurately describe the elastic response of composite structures and fibre metal laminates, however dynamic events such as impact laws create scaling conflicts as material properties are time dependent [136]. For composite materials, permanent deflection may not be the most appropriate performance measure as delamination failure is often predominant. However it has also been suggested that in the scaling of damage, the relationship of the total imparted damage to the absorbed impact energy should be considered and not just the relationship of one type of failure (such as delamination area) [137].

Due to manufacturing and material variability the average thickness of each FML series varied. In order to compare the performance of specimens independently of their thickness, the impact energy was normalised with a scaling factor, λ, which is the ratio of the specimen thickness to that of the thickest FML specimen. The normalised FML deflection was calculated with Equation 5.1 [136], where the permanent deflection was divided by the scaling factor. The non-dimensional energy, χ, was calculated with Equation 5.2 [136] which divided the impact energy, E, by the stress, σ, and a characteristic scale length, d.

$$\delta = \frac{deflection}{\lambda} \tag{5.1}$$

$$\chi = \frac{E}{\sigma d^3} \tag{5.2}$$

The characteristic scale length was the diameter of the indentor, which was constant for all tests therefore d was set to 1. The stress value was the theoretical UTS which was dependent on the FML thickness and accounted for the different FML thicknesses. Considering that the best description of the FMLs' response to impact was the total damage, the separation zone was measured for each specimen. The separation zone was representative of the total damage within the FML and was normalised by the scaling factor of the plate thickness as in Equation 5.1. The magnitude of one non-dimensional unit of separation and one non-dimensional unit of deflection corresponded to one millimetre of separation or deflection.

5.2. RESULTS

Preliminary impact tests were performed on FMLs that were manufactured from alodined aluminium and the Redux 609 film adhesive. These different FML specimens were manufactured by prepreg lay-up, wet lay-up of woven and UD GF and by the infusion of Injectex GF. The FMLs had very poor structural adhesion as reported in Appendix D. These FMLs exhibited minor plastically deformed dents in the aluminium and near complete debonding between the aluminium and the GFRP layers. The structural integrity of these FMLs was compromised prior to puncture (or even significant fibre failure) therefore these results were not considered further.

The FML specimens that were surface treated by bead-blasting or by a combination of bead-blasting, etching and either anodising or a silane treatment all exhibited puncture failure but maintained their interfacial integrity. The FMLs prepared with these surface treatments were therefore able to absorb all the incident impact energy as the tup punctured the layers. Due to the normalization of the impact energies, specimens tested at the same drop height were not necessarily comparable. FML specimens from different series with similar non-dimensional energy values were selected for qualitative comparison and are listed in Table 5.2.1. The full quantitative results are reported in section 5.2.4.

Table 5.2.1: FML specimens with similar non-dimensional impact energies

Non- dimensional Energy	Specimen	Vs	Specimen
0.037χ	ISS 10	Vs	ISG 4
0.041χ	ISA 10	Vs	ISG 2
0.034χ	ISA 3	Vs	ISS 8

The separation zones of the impact tested FML specimens with the same non-dimensional impact energies were evaluated to assess the extent of total internal damage of the different surface treated specimens. The internal damage was inspected to determine whether interlaminar delamination of GFRP layers or interfacial debonding occurred and the extent to which the different surface treatments resisted delamination failure. The deflection of the FML specimens was investigated as the plastic deformation provided an indication of the impact energy transferred from the interfaces to the aluminium. The fibre and matrix failure could not be measured as the FML laminate structure obscured the GFRP and the removal of the aluminium layers would have inflicted additional unquantifiable damage.

5.2.1. FML SEPARATION ZONE

The separation zone was a measure of the separation between the proximal and distal face of the impact tested FMLs, i.e. the extent of damage between the skins. The vertical separation distance of selected FMLs is represented by the profiles in Figure 5.2.1. The separation within 5mm from the point of impact was ignored because the damage in the FML was caused by the indentor punching the FML.

The separation zone profiles of the bead-blasted and silane treated specimens overlapped substantially in Figure 5.2.1(a) and could not be differentiated. The separation zone profiles of the bead-blasted and anodised FMLs specimens in Figure 5.2.1(b) have different shapes, but the maximum separation at 5mm from the point of impact was equal. The silane treated FML exhibited a substantially smaller separation zone than the anodised specimen in Figure 5.2.1(c). From this it could be deduced that the magnitude of separation and therefore the internal damage of the silane treated FMLs was substantially lower than that of the anodised specimens. A conclusion with regards to the internal damage of the bead-blasted specimens relative to the anodised and silane treated specimens could not be drawn because their deflection profiles were very similar.

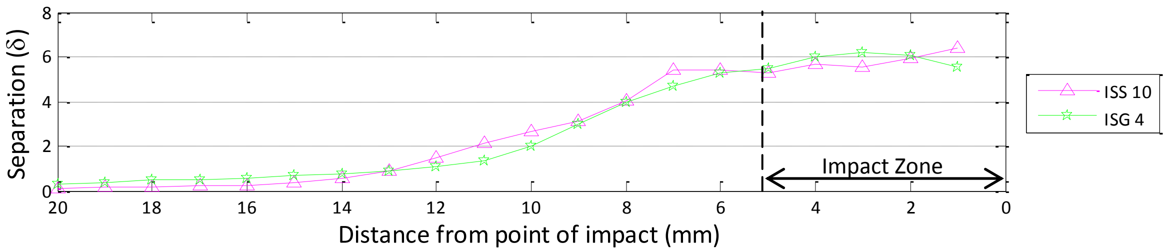

8

(a) The separation zone of a bead-blasted, etched and silane treated specimen (ISS 10) compared to a specimen that was bead-blasted only (ISG 4). Both were tested at a non-dimensional impact energy of 0.037.

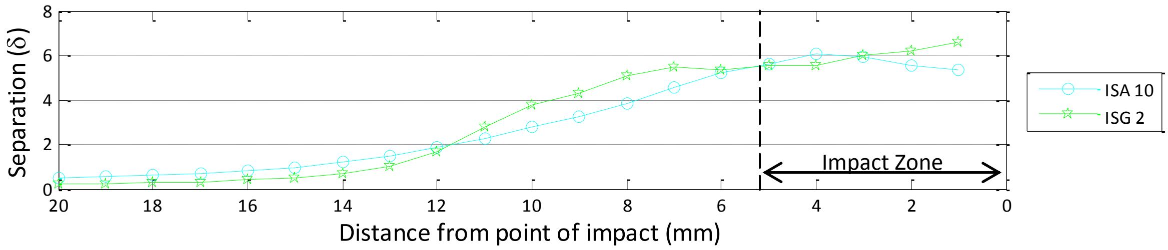

8

(b) Separation zone of a bead-blasted, etched and anodised FML specimen (ISA 10) compared to a FML specimen that was bead-blasted only. Both were tested at a non-dimensional impact energy of 0.041.

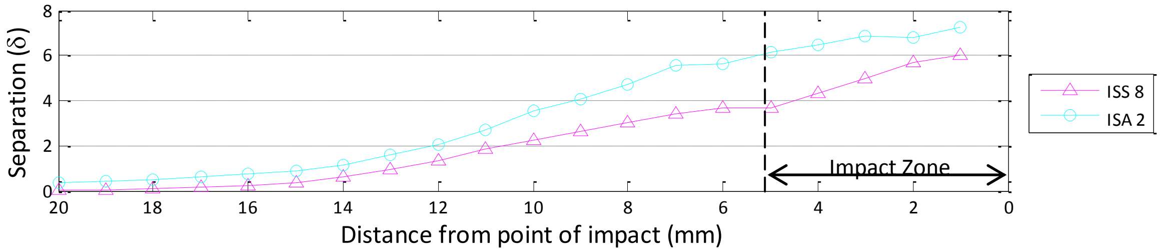

(c) The separation zone of a bead-blasted, etched and anodised FML specimen compared (ISA 2) to an FML specimen that was bead-blasted, etched and silane treated. Both were impact tested at a non-dimensional impact energy of 0.034.

Figure 5.2.1: The normalized separation zones of selected impact tested FML specimens

The 3D separation zones of the specimens are represented as contour plots in Figure 5.2.2, with the contour lines representing 1δ increments in vertical separation. The colours of the contour lines are representative of the magnitude of the separation which is indicated by the colour bar. The contour plots all exhibited localised areas with a high magnitude of separation resulting from rupturing and petalling which had occurred on the distal face of the FMLs and will be henceforth be referred to as the rupture zone. The rupture zone lay within the 2δ separation area and the vertical separation within the rupture zone included all damage such as petalling, fibre damage, matrix failure, interlaminar delamination and interfacial debonding.

The separated area of the contours at 1δ and 2δ of separation is recorded in Table 5.2.2 as a percentage of the total area exposed area in the clamp frame. The distance between the outer contour line representing 1δ of separation and the next contour line representing 2δ of separation was a good measure of the extent of separation or internal damage from the point of impact. The extent of separation is an indication of the separation gradient, such as the contour lines in the puncture zone that are close indicate a steeper gradient in the separation. The extent of separation is the difference between the 1δ and 2δ areas and is listed as Δδ in Table 5.2.2.

Table 5.2.2: The percentage area of the respective separation contours

Non-dimensional impact energy	**Specimen**	**Contour area (%)**			**Specimen**	**Contour area (%)**		
		1δ	**2δ**	**Δδ**		**1δ**	**2δ**	**Δδ**
0.034	**ISS 8**	6.70	5.46	1.25	**ISA 3**	11.78	6.45	5.30
0.041	**ISA10**	11.86	7.10	4.76	**ISG2**	8.56	6.58	1.99
0.037	**ISS10**	8.25	5.90	2.35	**ISG4**	9.28	6.06	3.22

From Figure 5.2.2, it was evident that the silane treated specimens (a and e) both exhibited smaller areas of separation when compared to their anodised (b) and bead-blasted (f) counterparts. The difference in the percentage areas at 1δ and 2δ separation of the silane specimens was very small (1.25% and 2.35%) therefore the extent of damage within silane specimens was very low. The anodised specimens (b and c) exhibited the largest areas of separation as well as the largest extent of internal damage. The bead-blasted specimens (d and f) had intermediate areas of separation and an intermediate difference between the 1δ and 2δ separation areas.

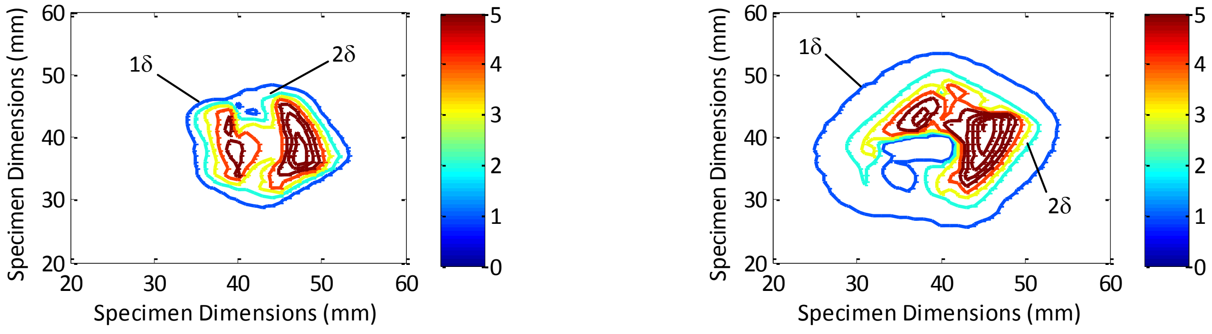

(a) Bead-blasted, etched and silane treated (ISS 8)

(b) Bead-blasted, etched and anodised (ISA 3)

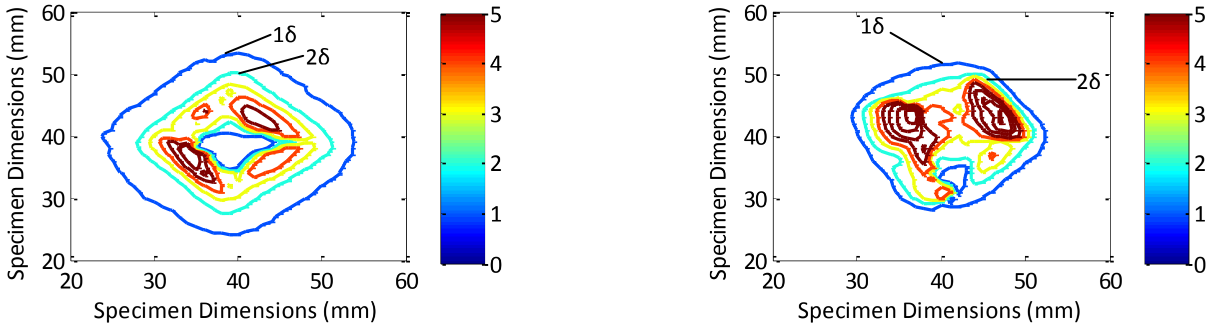

(c) Bead-blasted, etched and anodised (ISA 10)

(d) Bead-blasted (ISG 2)

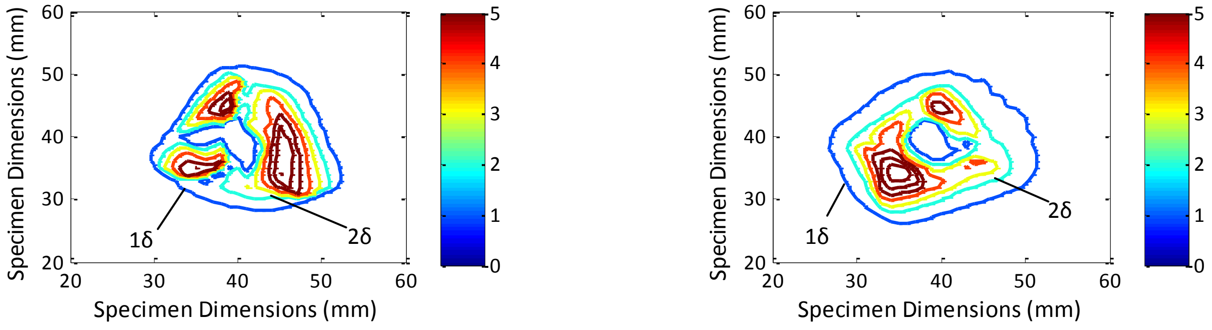

(e) Bead-blasted, etched and silane treated (ISS 10)

(f) Bead-blasted (ISG 4)

Figure 5.2.2: The separation zones of selected impact tested FMLs represented by contour plots.

The 1δ separation lines of the bead-blasted (d and f) and silane treated (a and e) specimens fitted the shapes of the rupture zone closely which illustrated that the internal damage did not extend far from the rupture zone. The anodised specimens (b and c) had the largest extent of lateral separation from the rupture zone, as they exhibited the highest magnitude of vertical and lateral separation. The silane specimens (a and e) had smaller 1δ separation areas and 2δ separation rupture zones compared to the bead-blasted specimens (d and f), but the magnitude of their vertical separation could not be distinguished from the profiles in Figure 5.2.1(a).

5.2.2. FML INTERNAL DAMAGE

The impacted FMLs were sectioned to characterize the internal damage by determining the extents and modes of separation within the separation zone. The specimens that were examined were all punctured; therefore all exhibited plastic deformation, fibre failure, matrix failure and debonding. No interlaminar delamination in the GFRP layers was observed that extended beyond the puncture zone where the indentor impacted the FMLs. The separation was primarily caused by interfacial debonding due to separation from the plastically deformed aluminium sheets.

The debonding occurred at the metal-GFRP interfaces and the different interfaces are depicted in Figure 5.2.3, where Interface 1 is against the distal face aluminium layer and Interface 4 is against the proximal face aluminium layer. These interfaces were inspected under magnification to determine the extent of the debonding and to determine whether the debonding occurred between the metal and the Redux 609 film adhesive or between the SE 84 LV resin and the film adhesive.

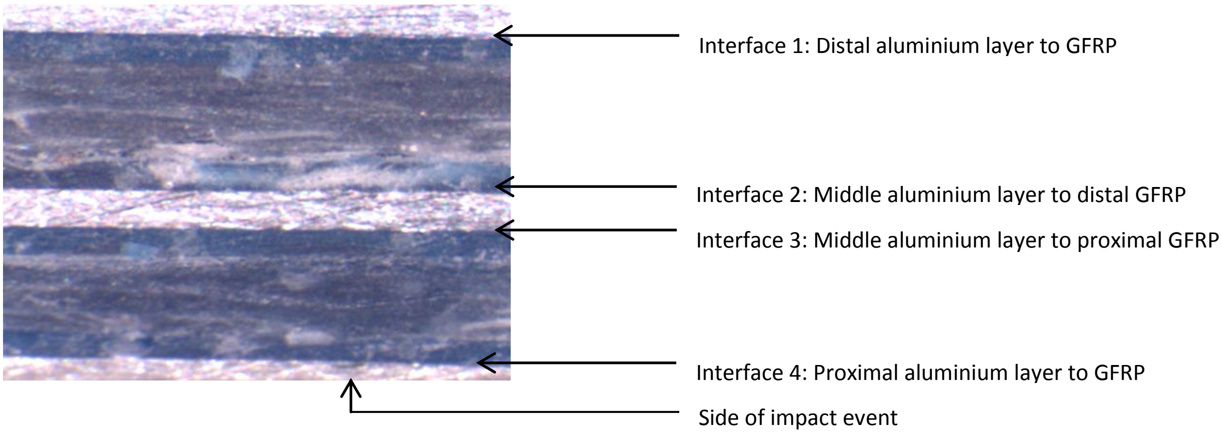

Figure 5.2.3: The adhesive interfaces of the FML specimens

5.2.2.1. EXTENT OF INTERFACIAL DEBONDING

The two sectioned FMLs depicted in Figure 5.2.4 were subjected to the same non-dimensional impact energy. The adhesive interfaces were investigated at 5mm steps from the point of impact to establish whether debonding had occurred at each step. In Figure 5.2.5 a marker indicates the prevalence of debonding in the specimen at the corresponding position and interface.

Figure 5.2.4: Photographs of FML cross-sections, ISS 8 (top) and ISA 3 (bottom), subjected to the same non-dimensional energy (0.034)

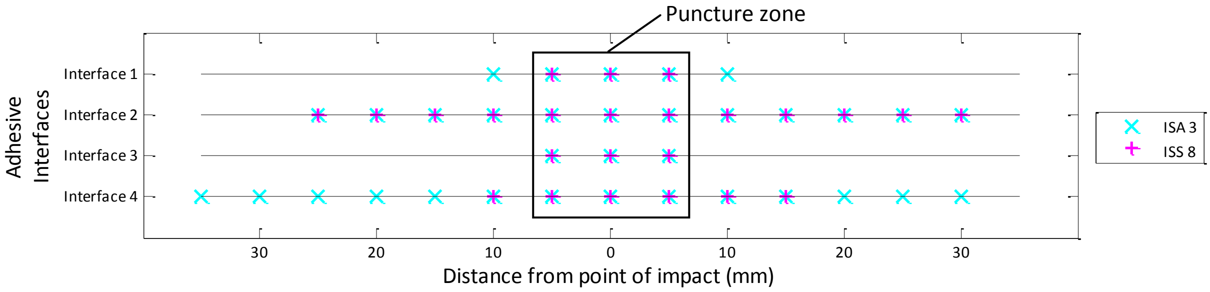

Figure 5.2.5: Comparison of the extent of interfacial debonding of two impact tested FMLs (ISA 3 vs ISS 8)

The anodised FML (ISA 3) displayed debonding beyond the puncture zone on Interface 1, but the silane treated FML (ISS 8) specimen did not. Both the ISS 8 and ISA 3 specimens displayed debonding of equal magnitude on both sides of the puncture zone on Interface 2. No debonding was recorded on Interface 3 to any side of the puncture zone. Both specimens debonded on Interface 4 to both sides of the puncture zone, but the magnitude of the debonding displayed by specimen ISA 3 was significantly larger extending to the edge of the specimen on the left side. The ISS 8 FML clearly showed a better resistance to debonding upon impact compared to the ISA 3 FML.

Figure 5.2.6: Photographs of FML cross-sections, ISG 2 (top) and ISA 10 (bottom), subjected to the same non-dimensional energy (0.041)

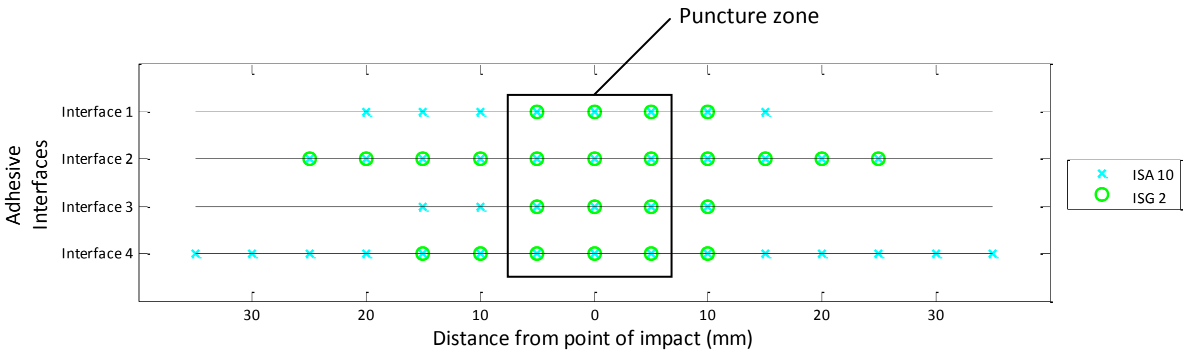

Figure 5.2.7: Comparison of the extent of the interfacial debonding of two impacted FMLs (ISA 10 vs ISG 2)

The anodised specimen (ISA 10) showed significant debonding on both sides of the puncture zone on Interface 1 in Figure 5.2.7, while the bead-blasted specimen (ISG 2) exhibited only a small amount to the right of the puncture zone. Both specimens had the same extent of debonding on Interface 2. The ISG 2 specimen displayed some debonding to the right of the puncture zone on Interface 3 which was due to more pronounced petalling at the point of impact, where specimen ISA 10 displayed debonding on both sides with significantly less petalling. Specimen ISG 2 debonded to both sides of the puncture zone, where specimen ISA 10 had debonded from the puncture zone to both edges of the specimen. The anodised specimen exhibited a significantly larger amount of debonding; therefore the bead-blasted specimens displayed the better impact response to debonding.

Figure 5.2.8: Photographs of FML cross-sections, ISS 10 (top) and ISG 4 (bottom), subjected to the same non-dimensional energy (0.037)

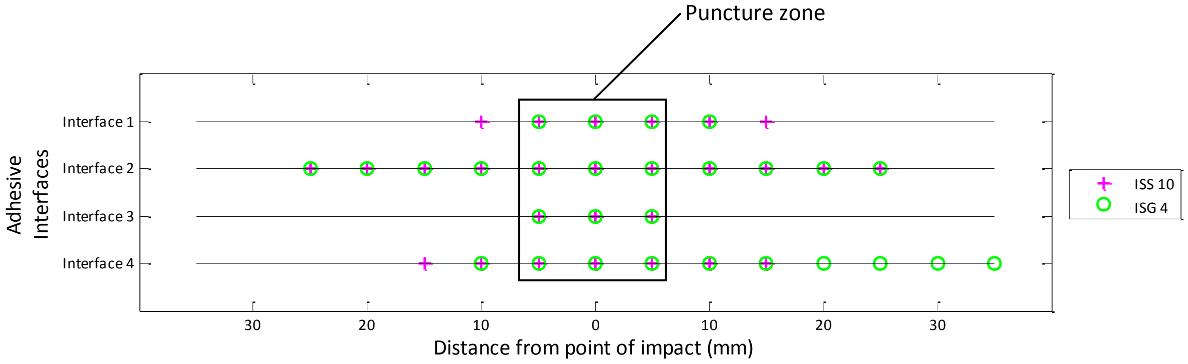

Figure 5.2.9: Comparison of the extent of interfacial debonding of two impacted FMLs (ISS 10 vs ISG 4)

The silane treated specimen (ISS 10) exhibited greater debonding to right of the puncture zone on Interface 1, which could have been ascribed to the nature of the petalling on the distal face. The ISS 10 specimen displayed debonding both sides of the puncture zone on Interface 4, where the debonding exhibited by the grit-blasted specimen (ISG 4) extended from the puncture zone to the edge of the specimen on the right hand side. The extent to which the ISG 4 specimen debonded, exceeded that of the ISS 10 specimen.

The largest extent of debonding occurred on Interfaces 2 and 4 which was the distal side of the outer and middle aluminium layers, however the anodised specimens exhibited debonding on interface 1 and 3 as well. The anodised FMLs exhibited the largest extent of debonding at the adhesive interfaces. The silane treated and bead-blasted specimens both performed significantly better than the anodised FMLs, but the bead-blasted specimens displayed marginally more debonding, therefore the silane treated surfaces performed slightly better.

5.2.2.2. NATURE OF INTERFACIAL DEBONDING

The nature of the debonding was investigated under optical magnification. The interface which failed and debonded was assumed to be the weaker interface in each case.

The interfacial debonding of the ISS 8 and ISA 3 specimens is shown in Figures 5.2.10(a) and 5.2.10(b) respectively. The debonding in the ISS 8 specimen occurred between the Redux 609 film adhesive and the GFRP as the blue film adhesive remained attached to the middle aluminium layer at Interface 2. The debonding occurred between the film adhesive and the aluminium at Interface 4 for specimen ISA 3 as the blue film could be seen attached to the GFRP. The silane-treated surface therefore provided better adhesion to the film adhesive compared to the anodised surface.

The anodised FML specimen (ISA 10) in Figure 5.2.10(c) exhibited debonding between the metal and the film adhesives on both Interfaces 2 and 4 as the film adhesive remained bonded to the GFRP. In the equivalent bead-blasted specimen (ISG 2) in Figure 5.2.10(d) the debonding occurred between the film adhesive and the GFRP. Hence the bead-blasted (ISG 2) surface performed better under impact as the film adhesive remained bonded to it after impact.

The silane treated (ISS 8) and bead-blasted (ISG 4) specimens in Figures 5.2.10(e) and (f) respectively, both exhibited debonding between the Redux 609 film adhesive and the GFRP, therefore the bonds between the film adhesive and the aluminium remained intact throughout the impact event.

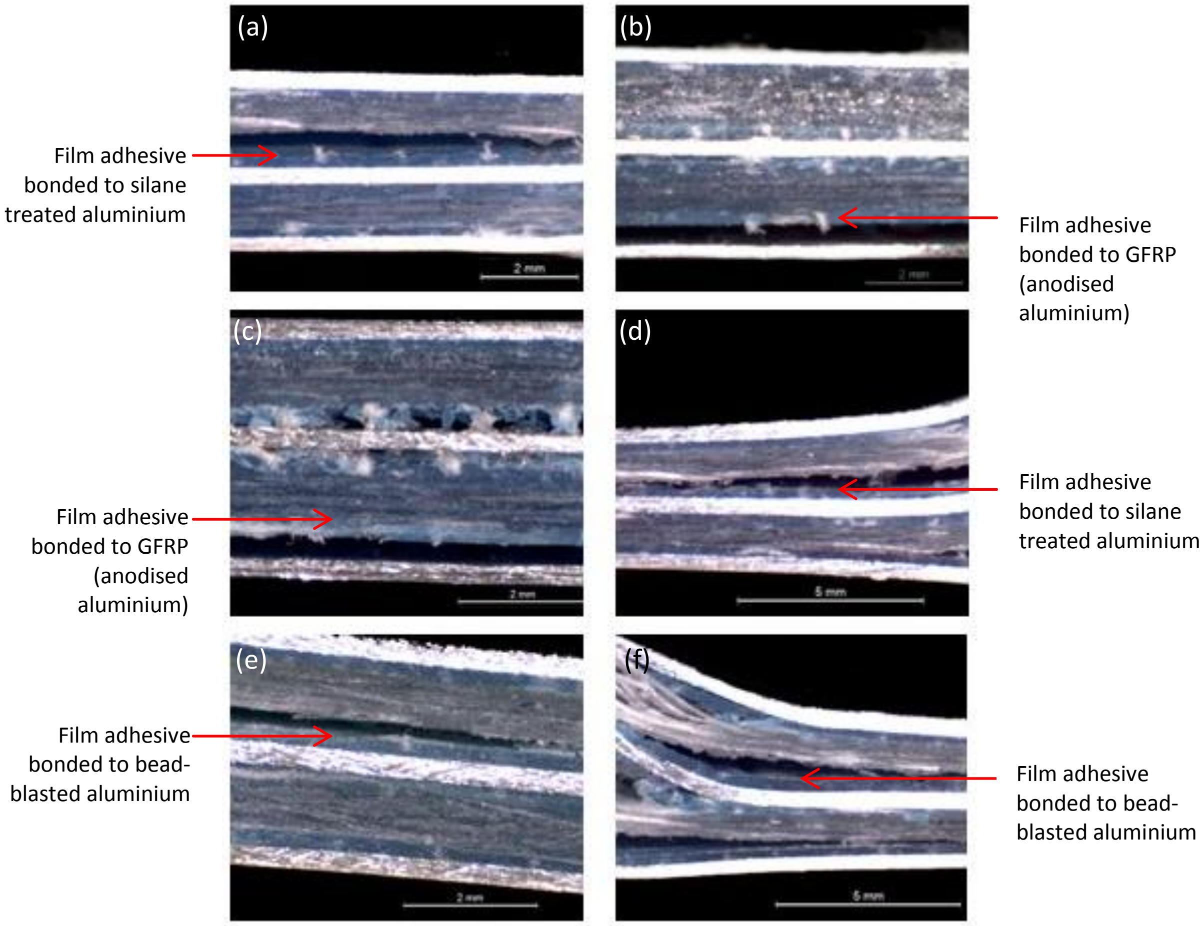

Figure 5.2.10: The adhesive interfaces of impact tested FMLs: (a) ISS 8, (b) ISA 3, (c) ISA 10, (d) ISG 2, (e) ISS 10 and (f) ISG 4.

The anodised FMLs debonded between the Redux 609 film adhesive and the aluminium therefore the anodised surface provided inferior adhesion to the film adhesive. The bead-blasted and silane treated surfaces both provided good adhesion as the bonds between the aluminium and film adhesive remained intact and the debonding occurred at the interface between the film adhesive and the GFRP.

5.2.3. PLASTIC DEFORMATION

The plastic deformation of the FMLs was evaluated to determine the amount of impact energy absorbed by this mode of failure. The low velocity impact tests produced puncture damage on the proximal and distal faces shown in Figure 5.2.11. The puncture diameter was a function of the indentor size and did not vary with FML type or impact energy.

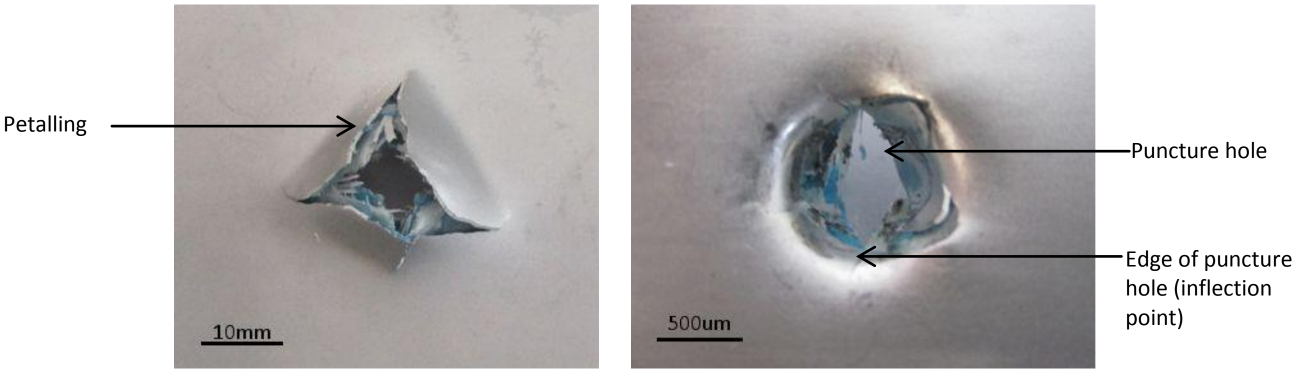

Figure 5.2.11: Impact damage on the (a) distal face and (b) proximal face of the impact tested ISA10 FML specimen

The deflection profiles measured on the proximal faces of three types of impact tested FMLs are shown in Figure 5.2.12. The profile curves displayed an inflection point at approximately 5-7mm from the point of impact where the deflection increased significantly. The inflection point was indicative of the edge of the puncture caused by the indentor, which had a diameter of 10mm. The magnitude was less than 1δ for all specimens from the edge of the specimen to about 8mm radially from the point of impact. The silane specimens exhibited deflections that were marginally higher than the bead-blasted and anodised specimens. The bead-blasted FML specimens exhibited the lowest deflection.

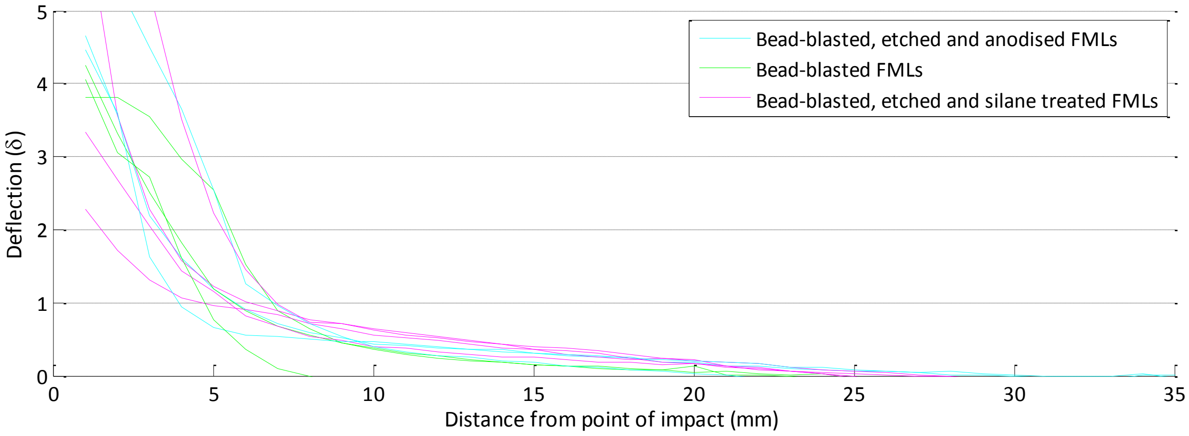

Figure 5.2.12: Deflection measured on the proximal face of the impact tested FMLs

The maximum permanent deflection of the distal faces of the impact tested FMLs were not considered as a measure for plastic deformation in this section as this value was obscured by the puncture failure and the shape of petalling. The deflection profiles of the distal face of the impact tested FMLs are represented as contour plots in Figure 5.2.13. The contour lines represent 1δ increments in the magnitude of deflection and the colour of the contour lines represents the magnitude of deflection as indicated by the colour bar

.

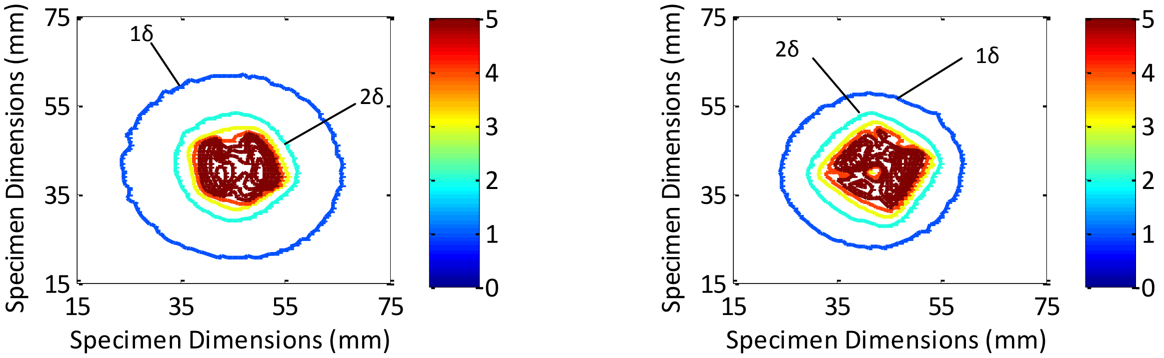

(a) Bead-blasted, etched and silane treated (ISS 8)

(b) Bead-blasted, etched and anodised (ISA 3)

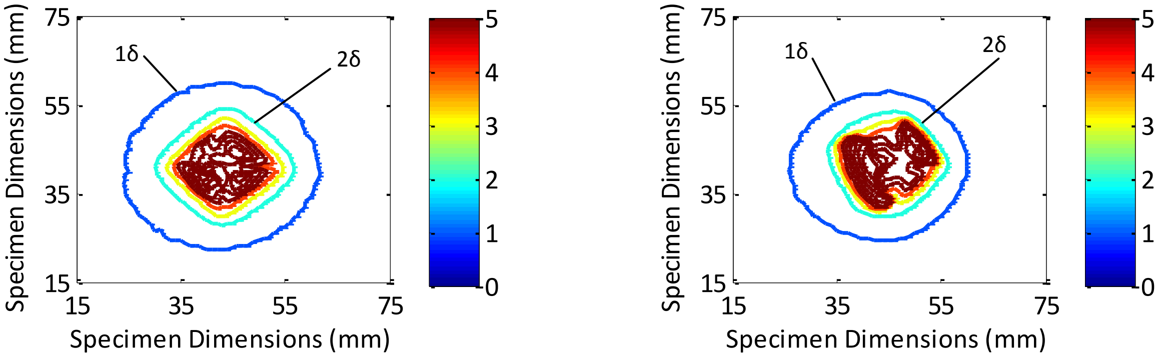

(c) Bead-blasted, etched and anodised (ISA 10)

(d) Bead-blasted (ISG)

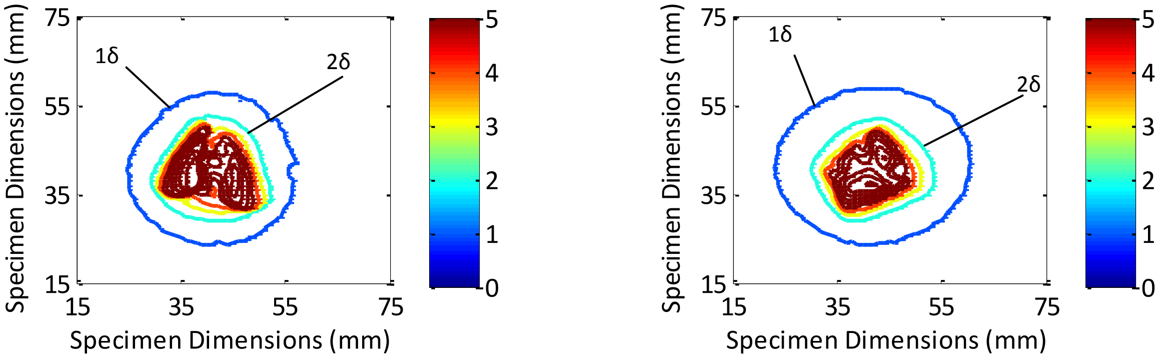

(e) Bead-blasted, etched and anodised (ISS 10)

(f) Bead-blasted (ISG 4)

Figure 5.2.13: The distal face deflection of selected impact tested FMLs represented by contour plots

The localised areas with a high magnitude of deflection represent the areas with rupturing and petalling on the distal face of the FMLs and are referred to as the rupture zone. The shapes of the 2δ deflection contour lines of all the specimens did fit the shapes of their rupture zones closely. The shapes of the 1δ deflection contour lines were circular and independent of the shape of the rupture zone. The distal face deflection of the FMLs gradually increased from the edge of the clamping boundary and was considered significant from 1δ of deflection. The reason the deflection was only regarded as significant from 1δ deflection is explained in Appendix C.

The areas of the contours at 1δ of deflection are listed in Table 5.2.3 as a percentage of the total exposed area. The silane treated specimen ISS 8 in Figure 5.2.5(a) had a significantly larger area of deflection compared to the anodised specimen ISA 3 (b). The anodised specimen ISA 10 (c) had a larger area of deflection than the bead-blasted specimen (d) and the bead-blasted specimen ISG 4 (f) had a larger area of deflection than the silane treated specimen ISS 10 (e). It could not be deduced from this selection of FMLs which type exhibited the highest degree of plastic deformation as no two specimens of the same type exhibited a higher percentage area deflection that was higher than their non-dimensional energy equivalent. There was therefore no consistency within this sample group.

Table 5.2.3: Comparison of the percentage deflection areas of different FMLs with the same non-dimensional energy

Non-dimensional impact energy	**Specimen**	**Deflected area (%)**	**Specimen**	**Deflected area (%)**
0.034	**ISS 8**	21.6	**ISA 3**	16.2
0.041	**ISA10**	17.5	**ISG2**	14.4
0.037	**ISS10**	15.5	**ISG4**	17.2

5.2.4. OVERALL IMPACT LOADING RESULTS

This section describes the overall trends in the results on all the specimens. Neither the deflection nor the separation of the specimens exhibited a linear dependence on the incident impact energy or on the non-dimension energy. In all cases the bead-blasted specimens exhibited the largest amount of scatter and the anodised specimens exhibited the least amount of scatter.

SEPARATION ZONE

The techniques used in Section 5.2.1 were utilized here to determine the areas over which the separation zones extended. The areas were calculated at 1δ and 2δ separation as a percentage of the total clamped areas. The specimens could not be compared based on their dependency of separation on non-dimensional energy, therefore averages were used. Specimens within a 0.0005χ non-dimensional energy range were selected and the average and standard deviation was calculated and are reported in Table 5.2.4.

Table 5.2.4: The average percentage separation areas (1δ, 2δ and Δδ) for specimens that fall within a 0.0005χ non-dimensional energy range

	Anodised FMLs			**Bead-blasted FMLs**			**Silane Treated FMLs**		
	1δ	2δ	Δ δ	1δ	2δ	Δ δ	1δ	2δ	Δ δ
Average	11.3%	6.7%	4.6%	10.0%	6.7%	3.3%	7.9%	5.8%	2.1%
Standard deviation	0.7%	0.3%	1.0%	0.5%	0.5%	1.1%	1.2%	0.3%	0.9%

The 2δ percentage area or rupture zone of the silane FMLs are the smallest and the bead-blasted FMLs had a similar 2δ percentage area to the anodised FMLs. The 1δ separation of the anodised specimens was the largest, and the silane specimens had the smallest 1δ separation areas. The results are plotted as a function of the specimens' non-dimensional energies in Figure D.1 in Appendix D

PLASTIC DEFORMATION

The plastic deformation was measured by the 1δ distal face deflection area as a percentage of the total exposed area as in section 5.2.5. The percentage deflection areas did not show a dependence on the non-dimensional energy. The average 1δ deflection was calculated for the same set of specimens within a 0.0005χ energy range. The averages, standard deviations and the ranges of the different FMLs are reported in Table 5.2.5.

Table 5.2.5: The average 1δ deflection area percentages

	Anodised FMLs	**Bead-blasted FMLs**	**Silane Treated FMLs**
Average	15.5%	17.2%	20.0%
Standard deviation	1.0%	8.0%	3.0%
Range	14.8-16.2%	12.2-22.3%	15.5-22.2%

The bead-blasted FMLs exhibited the largest range and standard deviation compared to the anodised and silane treated FMLs. The anodised specimens exhibited the smallest amount of plastic deformation. The silane treated FMLs exhibited the largest degree of plastic deformation with an intermediate degree of standard deviation. The plastic deformation percentage areas of all the specimens are plotted as a function of their non-dimensional energies in Figure D.

DAMAGE RATIO

The damage ratio was used as a measure of the internal damage relative to the plastic deformation and is calculated as a ratio of the 1δ separation area to the 1δ deflection area. The average damage ratios for the different FML types within the 0.0005χ non-dimensional energy group in Table 5.2.6.

Table 5.2.6: The damage ratios of the different FML types

	Anodised FMLs	**Bead-blasted FMLs**	**Silane Treated FMLs**
Separation Area (1δ)	11.3%	10.0%	7.9%
Deflection Area (1δ)	15.5%	17.2%	20.0%
Damage Ratio	0.72%	0.61%	0.40%
Standard deviation	0.001%	0.13%	0.1%

The silane treated specimens had the smallest damage ratio which was expected as the silane specimens exhibited both the largest 1δ deflected areas and the smallest 1δ separation areas. The damage ratios of the anodised FMLs were the highest, which indicated that the anodised specimens exhibited a substantial amounts of internal damage compared to its plastic deformation. The standard deviation of the bead-blasted FMLs was substantially high therefore some specimens would had similar damage ratios compared to the anodised FMLs. The average damage ratios for all the specimens are recorded in Table D.3.

5.3. SUMMARY OF TEST RESULTS

The impact performance of the FMLs with different surface treatments have been determined using drop loading and considering the ability of different surface treatments' ability to dissipate energy without debonding.

The separation zone measurement was used as a non-destructive method to measure the internal damage of the FMLs. The results are listed in Table 5.3.1. It was noted that:

- The silane treated FMLs had a smaller magnitude of vertical separation than the anodised specimens. The inspection of the adhesive interfaces indicated that the anodised FMLs exhibited debonding on all four adhesive surfaces which may explain the higher vertical separation.
- The silane treated specimens exhibited the smallest 1δ separation area as well as the smallest extent of damage from the damage zone (Δδ).

- The silane treated specimens exhibited the largest extent of plastic deformation and the smallest damage ratio, and therefore exhibited a larger extent of plastic deformation compared to the internal damage.
- The bead-blasted specimens exhibited intermediate damage ratios and the anodised specimens exhibited the largest damage ratios. This was expected as the anodised specimens exhibited larger extent of 1δ separation and a smaller 1δ deflection area.
- Neither the separation zone nor the plastic deformation exhibited any dependence on the non-dimensional impact energy.
- The anodised FMLs exhibited debonding between the aluminium and the film adhesive where the silane treated and grit-blasted FMLs exhibited debonding between the film adhesive and the GFRP.

Table 5.3.1: Summary of impact loading test results

	Anodised FMLs	**Bead-Blasted FMLs**	**Silane Treated FMLs**
Separation area (1δ)	11.3%	10.0%	7.9%
Rupture Zone (2δ)	6.7%	6.7%	5.8%
Separation area (Δ δ)	4.6%	3.3%	2.1%
Deflection area (1δ)	15.5%	17.2%	20.0%
Damage Ratio	0.73	0.61	0.40
Debonding Interface	Aluminium/ Redux 609	Redux 609/GFRP	Redux 609/GFRP

5.4. DISCUSSION:

5.4.1. 3D SCANNING AND SEPARATION ZONE CALCULATIONS

The accuracy of the NextEngine 3D scanner has been reported at 0.12mm [138]. The 3D profiles generated in the NextEngine ScanStudio HD software were realigned in MATLAB such that all the FML edges lay on the same plane. This allowed for accurate measurements of the proximal and distal face profiles. The extent of the separation and deflection were both measured at 1δ (equivalent to 1mm) therefore any surface artefacts (such as resin drops) were not included in the deflection measurements as described in Appendix C. The results obtained from the measured separation zone correlated well with the internal damage observed in the sectioned FMLs.

5.4.2. SAMPLE GROUP REPRESENTATION

The FMLs that were compared in sections 5.2.1 and 5.2.2 were a small sample group that were selected because their non-dimensional energies were equivalent. Table 5.4.1 compares the results of the selected FMLs to the average values of all the tested specimens reported in section 5.2.4 to establish how representative the sample group was.

Table 5.4.1: Comparison of selected FML sample group to average values based overall test results.

	Anodised FMLs			**Bead-Blasted FMLs**			**Silane Treated FMLs**		
	ISA 3	ISA 10	Average	ISG 2	ISG 4	Average	ISS 8	ISS 10	Average
Separation area (1δ)	11.78%	11.86%	11.3%	8.56%	9.28%	10.0%	6.70%	8.25%	7.9%
Rupture Zone (2δ)	6.45%	7.10%	6.7%	6.58%	6.06%	6.7%	5.46%	5.90%	5.8%
Separation area (Δ δ)	5.30%	4.76%	4.6%	1.99%	3.22%	3.3%	1.25%	2.35%	2.1%
Deflection area (1δ)	16.2%	17.5%	15.5%	14.4%	17.2%	17.2%	21.6%	15.5%	20.0%
Damage Ratio	0.73	0.68	0.73	0.60	0.54	0.61	0.31	0.53	0.40

The average values for the different FMLs tended to fall between the values reported for the selected FMLs of the respective FML type, but in some cases the average values were marginally lower or higher than the selected FML values. Despite the variation, the trends for the 1δ separation area and the Δ δ separation areas remained consistent as the anodised FMLs exhibited the largest 1δ and Δ δ separation areas and the silane treated FMLs exhibited the lowest 1δ and Δ δ separation areas. The average rupture zone of the silane treated FMLs remained the smallest, however the average rupture zone of the bead-blasted FMLs and the anodised specimens were equivalent, but the differences compared to the selected FMLs were rather small. No specific trend was identified with regards to the deflection areas of the selected FMLs, but from the average values it was established that the silane treated FMLs had the largest extent of plastic deformation and the anodised specimens had the lowest. The average damage ratio of the silane treated FMLs were lower than the average damage ratios of both the anodised and bead-blasted FMLs.

The average values of the silane treated FMLs correlated well to the results of the ISS 8 and ISS 10 FMLs and were consistent relative to the bead-blasted and anodised FMLs results. Only the average rupture zone deviated from the trends observed from the selected specimens. This could be ascribed to the ISG 2 and ISG 4 FMLs falling within the lower bound of the bead-blasted range of specimens as the average values of the bead-blasted FMLs were marginally higher than the results of the ISG 2 and ISG 4 FMLs. Despite the average values varying marginally from the values of the selected FMLs, similar conclusions were drawn with regards to the overall performance.

5.4.3. NORMALISATION OF PLATE THICKNESS

The surface treatments utilized to prepare the aluminium of the FML impact specimens all modified the surface chemistry or surface morphology by the removal of aluminium from the surface [71], with the exception of the silane treatment. The thickness of each aluminium sheet was reduced by each successive treatment. The reduction in the thickness of the aluminium used for the SLB tests was negligible considering the sheets were 2mm thick. The aluminium used to manufacture the FML impact specimens were 0.46mm thick prior to treatment and the resultant thicknesses of the sheets are reported in Table 5.4.2. The combined thickness of the prepreg and film adhesive layers remained relatively constant which was expected due to their inherent bond-line thickness control.

Table 5.4.2: Average thicknesses of the FML specimens and its constituents

Specimen	**Aluminium thickness (single sheet)**	**Aluminium thickness (3 sheets)**	**Total FML thickness**	**Prepreg & film adhesive thickness**
Bead-blasted	0.46mm	1.39mm	3.71mm	2.31mm
GB, etched and anodised	0.33mm	1.00mm	3.32mm	2.32mm
GB, etched and silane treated	0.38mm	1.15mm	3.50mm	2.35mm

The thinning as a result of the chemical treatments was not an unusual occurrence and has been reported in other studies [75, 114]. The variable thicknesses were accounted for by adapting the aluminium volume fractions in the theoretical UTS calculation using the rule of mixtures. The silane treated specimens with intermediate thickness had the highest plastic deformation. The bead-blasted FMLs were the thickest and had the lowest average plastic deformation, however when the standard deviation reported in section 5.2.4 was considered, the 1δ deflection area of the bead-blasted specimens overlap significantly with both the anodised and silane treated FMLs. This suggested that the aluminium thickness was not the only factor affecting the impact response.

Table 5.4.3: Comparison of aluminium thickness and plastic deformation

Thickness:	Bead-blasted FMLs	>	Silane treated FMLs	>	Anodised FMLs
Plastic deformation:	Silane treated FMLs	>	Bead-blasted FMLs	>	Anodised FMLs

The normalisation of the incident impact energies allowed for reasonable comparison between the impact specimens manufactured with different thicknesses. McKown et al [112] utilized the same normalisation techniques to scale the impact to test its validity for composites. The theoretical UTS was used in the present study to calculate the non-dimensional energy (NDE), where an average of the yield stress and UTS was used by McKown [136] and only the yield stress by Carillo et al [139]. The 0.025-0.045 non-dimensional energy range obtained in this study fell within the range of non-dimensionless energies obtained by McKown (0.005-0.045χ) [136] suggesting that the theoretical UTS provided adequate scaling.

5.4.4. SURFACE TREATMENT PERFORMANCE

It was observed in section 5.2.2.2 that the film adhesive remained bonded to the bead-blasted and silane treated aluminium, but not to the anodised aluminium. The prepreg / film adhesive interface appeared to be weaker than the film adhesive / bead-blasted and silane treated aluminium interface. No aluminium oxide was observed on the film adhesive layer in the anodised FMLs after impact, as shown in Figure 4.13(c), therefore the anodised aluminium / film adhesive interface was weaker than the film adhesive / prepreg interface. The silane treated and the bead-blasted specimens both exhibited debonding at the Redux 609 / GFRP therefore the superior surface treatment could not be identified from this alone. By inspection the following was deduced with regards to the strength of the adhesive interfaces:

Table 5.4.4: Comparison of adhesive interfaces based on results from section 5.2.4

Anodised aluminium/film adhesive	<	Film adhesive/ prepreg	<	Film adhesive/bead-blasted aluminium
				↕ Could not be distinguished from results in 5.2.2.2
Anodised aluminium/film adhesive	<	Film adhesive/ prepreg	<	Film adhesive/bead-blasted, etched and silane treated aluminium

The 1δ separation area of the anodised FMLs was substantially larger than that of the bead-blasted and the silane treated FMLs and extended substantially further from the rupture zone (larger Δδ separation). The extent of the internal damage within the anodised specimens was established as more severe compared to the silane and etched specimens in section 5.2.1. The extent of interfacial delamination was therefore greatest within the anodised specimens. The silane treated specimens had a smaller 1δ separation area, rupture zone and Δδ separation area compared to the bead-blasted specimens. The silane specimens therefore had a smaller extent of internal damage compared to the bead-blasted specimens. A larger extent of internal damage was also observed in the cross-sections of the bead-blasted specimens in section 5.2.2. Therefore the extent of interfacial delamination was found to be the smallest for the silane treated specimens under impact loading.

It was established in section 2.4 that a major factor in the absorption of the incident impact energy was the ability of the adhesive interface to transfer the energy from the outer proximal laminate to the inner laminates for an optimal distribution of energy. It was also determined that a higher degree of plastic deformation was indicative of superior adhesion. The silane specimens exhibited the largest degree of 1δ deflection area therefore the highest ratio of plastic deformation relative to the internal damage. The silane treated FMLs thus exhibited the best impact energy absorption capability. It was not clear from the results whether the impact absorbing capability of the silane treated FMLs were better due to superior bonding exclusively or whether the diffuse molecular layer at the aluminium interface contributed to the dissipation of impact energy. It is also uncertain how this could be determined.

5.4.5. IMPACT RESPONSE DEPENDENCE ON INCIDENT IMPACT ENERGY

The results in section 5.2.4 did not exhibit any obvious dependence of the impact response on the incident impact energy. The energy range over which the different types of FMLs were tested was rather small, therefore the dependence of impact response on impact energy could have been obscured by the standard deviation.

CHAPTER 6: CONCLUSION AND RECOMMENDATIONS:

The aim of this study was to work toward manufacturing FMLs that did not exhibit any interfacial debonding between the metal-GFRP under dynamic loading.

6.1. MANUFACTURING AND SURFACE PREPARATION TECHNIQUES

Three Point Bend tests were performed to determine the best manufacturing method to produce the SLB and FML specimens. It was established that the wet lay-up technique or prepreg sheets should be used to manufacture FMLs. The macro-roughening from the bead-blasting technique was comparable to results found in literature [84]. The surface roughness of the bead-blasted and etched surfaces was higher than typical, but the elemental surface analysis showed that the etchant removed all contaminants and unstable surface oxides. The anodising technique produced a stable surface oxide with consistent pore and cell diameters. The pore diameters were larger than typically reported in literature and the pore distribution density was also significantly lower, therefore the anodised surface had a lower effective surface area.

6.2. SINGLE LEG BEND TESTS

The Single Leg Bend tests were used to measure the fracture toughness of bonds to different surface treatments. Stable crack growth was obtained allowing for good measurements. The specimens manufactured with prepreg sheets exhibited superior adhesion to those impregnated with the Prime 20 LV resin. The fracture toughness of the bonds increased in the order:

- bead-blasted
- bead-blasted and then etched
- bead-blasted, then etched and then anodised
- bead-blasted, then etched then silane treated
- bead-blasted, then silane treatment

The anodised surfaces did not perform as well as expected. The bead-blasted and silane treated specimens had higher energy release rates compared to the anodised and bead-blasted, etched and silane treated SLB specimens. The inclusion of the Redux 609 film adhesive improved the adhesion of the aluminium surfaces drastically such that energy release rate of the combination of bead-blasting, prepreg and the film adhesive approached that reported for GLARE.

6.3. IMPACT LOADING

The internal damage of the impact tested FMLs was investigated by determining the magnitude of separation between the proximal and distal faces of the FMLs. The separation zone was a good measure of the internal damage as it correlated well with the internal damage observed in the sectioned FML panels. The separation zone was measured in a non-destructive manner therefore has the potential to be developed further as an analysis technique in conjunction with other non-destructive testing methods.

The anodised FMLs exhibited the largest extent of interfacial debonding and the least amount of plastic deformation. The bead-blasted specimens exhibited a large amount of scatter in terms of the plastic deformation, but exhibited less interfacial debonding than the anodised specimens. The silane treated specimens exhibited the smallest extent of interfacial debonding and the largest extent of plastic deformation. The silane treatment therefore performed best with regards to being able to absorb the incident impact energy without interfacial debonding.

6.4. RESEARCH OUTCOMES

Very high energy release rates were obtained under quasi-static loading for which specimens approached the energy release rate reported for GLARE, such that the unstable aluminium surface oxide failed instead of the adhesive interface. The impact tested FMLs still exhibited marginal interfacial debonding, however their impact performance was by far superior to the initial FMLs that were produced. FMLs manufactured by silane treated aluminium and Redux 609 film adhesive with SE 84 LV prepreg should produce the FMLs that are able to withstand impacts and blasts approaching those of GLARE.

6.5. RECOMMENDATIONS

- Investigation into the effect that surface roughness has on the measured fracture toughness by various techniques with different mode ratios can reveal details pertaining to the effects of micro- and macro-roughening on crack evolution.
- The clamping mechanisms that hold the impact specimens in place can be modified such that drilling and/or machining is eliminated from the manufacturing process. This would remove any damage that could result from this process.
- The effect of the second curing cycle on the Redux 609 film adhesives should be investigated. There may be merit in consolidating the film adhesives and the prepreg sheets such that a single oven program is followed. The manufacturing cycle time would be reduced with the potential of improved mechanical and adhesion properties of the film adhesive.
- Testing the FMLs over a larger range of impact energies may reveal the dependence of FMLs' impact response on the incident impact energy that was obscured by large scatter in this study. Testing over a larger range of impact energies may also explain the evolution of internal damage within the FMLs. An impact tester with a pneumatic clamp is recommended to prevent the indentor from striking the specimen multiple times after the first impact event at lower energies.
- An elemental surface analysis of the FMLs after the impact event could reveal the mechanism or loci of interfacial debonding as a result of the impact. This could possibility be done using Attenuated Total Reflectance Spectroscopy which is an infrared technique modified to inspect surfaces. The absence and presence of specific bonds can be used to determine the loci of failure at a chemical level.
- Time delays between sequential camera timer programs resulted in a loss of Single Leg Bend data points over those time periods. A continuous timer program could be used otherwise video footage will also improve these measurements.
- The steady increase in energy release rate with crack extension should be investigated to improve understanding of the results produced by the Single Leg Bend test.

REFERENCES

[1] B. Cozzi, “Clipper Maid of the Seas: Flight 103 - Lockerbie, Scotland,” PanAm Air, 2011. [Online]. Available: http://www.panamair.org/accidents/lockerbievictims.htm.

[2] M. Cox and T. Foster, Their Darkest Day: The Tragedy of Pan Am 103 and It's Legacy of Hope, Grove Pr, 1992.

[3] H. Fleischer, “Design and Explosive Testing of a Blast Resistant Luggage Container,” in *International Conference on Structures under Shock and Impact*, Udine, Italy, 1996.

[4] G. Langdon, Y. Chi, G. Nurick and P. Haupt, “Response of GLARE Panels to Blast Loading,” *Engineering Structures,* vol. 31, pp. 3116-3120, 2009.

[5] J. Kim, L. Leung, S. Lee and Y. Hiray, “Impact Performance of a Woven Fabric CFRP Laminate,” *Polmers & Polymer Composites,* vol. 4, pp. 549-561, 1996.

[6] J. Kim and M. Sham, “Impact and Delamination Failure of Woven-Fabric Composites,” *Composites Science and Technology,* pp. 745-761, 2000.

[7] G. Langdon, W. Cantwell and G. Nurick, “The Blast Response of Novel Thermoplastic-based Fibre-metal Laminates - Some Preliminary Results and Observations,” *Composites Science and Technology,* vol. 65, pp. 861-872, 2005.

[8] J. Gerdeen, R. Rorrer and H. Lord, Engineering Design with Polymers and Composites, Taylor & Francis, 2005.

[9] W. Work, K. Horie, M. Hess and R. Stepto, “Definitions and Terms Related to Polymer Blends, Composites and Multiphase Polymeric Materials,” *Pure and Applied Chemistry,* vol. 76, no. 11,

pp. 1985-2007, 2004.

[10] P. Dufton, Lightweight Thermoset Composites: Materials in Use, their Processing and Applications, iSmithers Rapra Publishing, 2000.

[11] A. Baker and S. Dutton, Composite Materials for Aircraft Structures, Reston: American Institute of Aeronautics and Astronautics Inc., 2004.

[12] M. Gupta, Polymer Composite, New Age International, 2005.

[13] J. Mark, Physical Properties of Polymers, Cambridge University Press, 2004.

[14] K. Horie, M. Baron, R. Fox, J. He and M. Hess, “Definitions of Terms Relating to Reaction of Polymers and to Functional Polymeric Materials,” *Pure and pplied Chemistry,* vol. 76, no. 4, pp. 889-906, 2004.

[15] J. Bicerano, Prediction of Polymer Properties, CRC Press, 2002.

[16] S. Beland, High Performance Thermoplastic Resins and Their Composites, New Jersey: Noyes Publications, 1990.

[17] J. Fink, Reactive Polymers Fundamentals and Applications: A Concise Guide to Industrial Polymers, William Andrew, 2013.

[18] A. Bhargava, Engineering Materials: Polymer Ceramics and Composites, New Delhi: PHI Learning Pvt. Ltd, 2005.

[19] J. Massingill and R. Bauer, “Epoxy Resins,” in *Applied Polymer Science: 21st Century*, Oxford, Elsevier, 2000, pp. 393-424.

[20] C. May, “Epoxy Materials,” *Electronic Materials Handbook: Packaging,* p. 1224, 1989.

[21] “Cross-Sections,” Stanford University, 12 April 2010. [Online]. Available: http://cantorscience.wordpress.com/2010/04/12/hey-whats-that-stuff/.

[22] N. Kaprinidis, “Flame Retardant prepregs and laminates for printed circuit boards”. Europe Patent EP 1 948 735 B1, 06 November 2006.

[23] MP Biomedicals , “3,3',4,4'-Benzonphenone tetracarboxylic dianhydride Product Sheet,” MP Biomedicals, [Online]. Available: http://www.mpbio.com/product.php?pid=05220263&country=193.

[24] S. Kouchi, M. Ishikawa, O. H. and G. Tanaka, “Epoxy resin composition for fiber reinforced composite material, a production method for fiber reinforced composite material, and a fibre reinforced composite material”. United States Patent US7709582 B2, 4 May 2010.

[25] P. Smith and J. Yeomans, “Benefits of Fiber and Particulate Reinforcement,” in *Materials Science and Engineering - Volume II*, Encyclopedia of Life Support Systems, 2009, pp. 133-154.

[26] L. Tong, A. Mouritz and M. Bannister, 3D Fibre Reinforced Polymer Composites, Elsevier, 2002.

[27] H. Youssef, H. El-Hofy and M. Ahmed, Manufacturing Technology: Materials, Processes and Equipment, Boca Raton: CRC Press, 2011.

[28] R. Gibson, Principles of Composite Material Mechanics, Boca Raton: CRC Press, 2011.

[29] A. Vlot and J. Gunnink, Fiber Metal Laminates: An Introduction, Springer, 2001.

[30] T. Chou, Microstructural Design of Fibre Composites, Cambridge: Cambridge Universtiy Press, 1992.

[31] S. Bishop, “Strength and Failure of Woven Carbon-fibre Reinforced Plastics for High Performance Applications,” in *Textile Structural Composites*, Elsevier Science Publishers, 1989, pp. 173-207.

[32] J. Whitcomb, “Three-dimension Stress Analysis of Plain Weave Composites,” in *Composite Materials: Fatique and Fracture, Vol 3*, Philadelphia, American Society for Testing and Materials, 1991, pp. 417-438.

[33] C. Zweben, “Mechanics of Composite Materials,” in *Delaware Composites Design Encyclopedia, Vol 1*, Lancaster, Technomic Publishing Co., 1989, pp. 17-48.

[34] S. Kumar and V. Gupta, “High Performance Fibres for High Performance and Non-conventional Applications,” in *Manufactured Fibre Technology*, Cornwall, Chapman & Hall, 1997, pp. 514-548.

[35] R. Hausrath and A. Longobardo, “High Strength Fibres and Markets,” *Fiberglass and Glass Technology,* p. 474, 1 January 2010.

[36] V. Kostikov, Fibre Science and Technology, Springer, 1995.

[37] C. Vermeeren, “A Historic Overview of the Development of Fibre Metal Laminates,” *Applied Composite Materials,* no. 10, pp. 189-205, 2003.

[38] G. Eckhold, Design and Manufacture of Composite Structures, Cambridge: Woodhead Publishing Ltd., 1994.

[39] A. Kulshreshtha and C. Vasile, “Composites: At the Turn of the Century,” in *Handbook of Polymer Blends and Composites: Vol I*, iSmithers Rapra Publishing, 2002, pp. 501-528.

[40] A. Vlot, V. Vogelesang and T. de Vries, “Towards Application of Fiber Metal Laminates in Large Aircraft,” *Aircraft Engineering and Aerospace Technology,* vol. 71, no. 6, pp. 558-570, 1999.

[41] V. Vogelesang and A. Vlot, “Development of Fiber Metal Laminates for Advanced Aerospace Structures,” *Journal of Materials Processing Technology,* vol. 103, pp. 1-5, 2000.

[42] A. Asundi and A. Choi, “Fiber Metal Laminate: Advanced Material for Future Aircraft,” *Journals of Materials Processing Technology,* vol. 63, pp. 384-394, 1997.

[43] J. Remmers, “Discontinuities in Materials and Structures: a Unifying Computational Approach,” PhD Thesis, Delft University of Technology, 2008.

[44] R. Alderstein and J. Homan, “Fatigue and Damage Tolerance Issues of Glare in Aircraft Structures,” *International Journal of Fatigue,* vol. 28, pp. 1116-1123, 2006.

[45] T. Sinmazcelik, E. Avcu, M. Bora and O. Coban, “A Review: Fiber Metal Laminates, Background, Bonding Types and Applied Test Methods,” *Materials and Design,* vol. 32, pp. 3671-3685, 2011.

[46] G. Wu and J. Yang, “The Mechanical Behaviour of GLARE Laminates for Aircraft Structures,” *Journal for the Minerals, Metals & Materials Society,* vol. 57, no. 1, pp. 72-79, 2005.

[47] R. Matsuzaki, M. Shibata and A. Todoroki, “Improving Performance of GFRP/aluminium Single Lap Joints Using Bolted/Co-cured Hybrid Method,” *Composites Part A: Applied Science and Manufacturing,* vol. 39, pp. 154-163, 2008.

[48] G. Critchlow, K. Yendall, D. Bahrani, A. Quinn and F. Andrews, “Strategies for the Replacement of Chromic Acid Anodising for the Structural Bonding of Aluminium,” *International Journal of Adhesion & Adhesives,* vol. 26, p. 419–453, 2006.

[49] W. Brockmann, P. Geiß, j. Klingen and K. Schröder, Adhesive Bonding: Materials, Applications and Technology, Weinheim: John Wiley & Sons, 2009.

[50] S. Ebnesajjad, Handbook of Adhesives and Surface Preparation, William Andrew, Elsevier, 2010.

[51] R. Adams, J. Comyn and W. Wake, Structural Adhesive Joints in Engineering, Springer, 1997.

[52] D. Kyluik, T. Sutton, Y. Scott and M. Scott, “Polymer-Mediated Broad Spectrum Antiviral Prophylaxis: Utility in High Risk Environments,” in *Progress in Molecular and Environmental Bioengineering - From Analysis and Modeling to Technology Applications*, InTech CC BY-NC-SA 3.0 license, 2011.

[53] T. Crompton, Polymer Reference Book, Shawbury: iSmithers Rapra Publishing, 2006.

[54] S. Park and S. M.K., Interface Science and Composites, Academic Press, 2011.

[55] J. Kim and Y. Mai, Engineered Interfaces in Fiber Reinforced Composites, Oxford: Elsevier Science Ltd, 1998.

[56] A. Kinloch, Adhesion and Adhesives: Science and Technology, Cambridge University Press, 1987.

[57] G. Raj, Advanced Inorganic Chemistry, Vol 1, Meerut: Krishna Prakashan Media (P) Ltd., 2008.

[58] D. Mercier and M. Barthes-Labrousse, “The Role of Chelating Agents on the Corrosion Mechanisms of Aluminium,” *Corrosion Science,* vol. 51, pp. 339-348, 2009.

[59] L. Garrigues, N. Pebere and F. Dabosi, “An Investigation of the Corrosion Inhibition of Pure Aluminium in Neutral and Acidic Chlorine Solutions,” *Electrochimico Acta,* vol. 41, pp. 1209-1215, 1996.

[60] S. Park, W. Choi, H. Choi and H. Kwon, “Effects of Surface Pre-treatment and Void Content on GLARE Laminate Process,” *Journal of Materials Processing Technology,* vol. 210, p. 1008–1016, January 2010.

[61] A. Higgins, “Adhesive Bonding for Aircraft Structures,” *International Journal of Adhesion & Adhesives,* vol. 20, pp. 367-376, 2000.

[62] A. Rider, “Bond Durability of Grit-blast and Silane Treated Metallic Adherends Bonded with Room Temperature Curing Adhesives,” DSTO Aeronautical and Maritime Research Laboratory, Victoria, Australia, 2001.

[63] J. Liu, M. Chaudhury, D. Berry and J. Seeburgh, “Effect of Surface Morphology on Crack Growth at a Sol-Gel Reinforced Epoxy/Aluminum Interface,” *The Journal of Adhesion,* vol. 82, pp. 487-516, 2006.

[64] S. Park, W. Choi, H. Choi, H. Kwon and S. Kim, “Recent Trends in Surface Treatment Technologies for Airframe Adhesive Bonding Processing: A Review (1995-2008),” *The Journal of Adhesion,* vol. 86, pp. 192-221, 2010.

[65] A. Harris and A. Beevers, “The Effects of Grit-blasting on Surface Properties for Adhesion,” *International Journal of Adhesion & Adhesives,* vol. 19, pp. 445-452, 1999.

[66] O. Cakir, “Chemical Etching of Aluminium,” *Journal of Materials Processing Technology,* vol.

199, pp. 337-340, 2008.

[67] S. Prolongo and A. Urena, “Effect of surface Pretreatment on the Adhesive Strength of Epoxy-alumnium Joints,” *International Journal of Adhesion & Adhesives,* vol. 29, pp. 23-31, 2009.

[68] A. Pocius, “The Electrochemistry of the FPL (Forest Product Laboratory) Process and its Relationship to the Durability of Structural Adhesive Bonds,” *The Journal of Adhesion,* vol. 39, no. 2-3, 1992.

[69] R. Digby and D. Packham, “Pretreatment of Aluminium: Topography, Surface Chemistry and Adhesive Bond Durability,” *International Journal of Adhesion and Adhesives,* vol. 15, pp. 61-71, 1995.

[70] G. Critchlow and D. Brewis, “Review of Surface Pretreatments for Aluminium Alloys,” *International Journal of Adhesion & Adhesives,* vol. 16, pp. 255-275, 1996.

[71] W. Brockmann, O.-D. Hennemann and C. Matz, “Adhesion in Bonded Aluminium Joints for Aircraft Construction,” *International Journal of Adhesion and Adhesives,* vol. 6, no. 3, pp. 115-143, 1986.

[72] M. Davis and D. Bond, “Principles and Practices of Adhesive Bonded Structural Joints and Repairs,” *International Journal of Adhesion and Adhesives,* vol. 19, pp. 91-105, 1999.

[73] M. Pennisi, 1999. [Online]. Available: http://www.coatfab.com/anodising.htm.

[74] B. Mert, B. Yazici, T. Tuken, G. Kardas and M. Erbil, “Anodizing and Corrosion Behaviour of Aluminium,” *Protection of Metals and Physical Chemistry of Surfaces,* vol. 47, no. 1, pp. 102-107, 2011.

[75] A. Bjorguma, F. Lapiqueb, J. Walmsleya and K. Redford, “Anodising as Pre-treatment for Structural Bonding,” *International Journal of Adhesion & Adhesives,* vol. 23, p. 401–412, May 2003.

[76] Y. Choo and O. Devereux, “Barrier-Type Alumnium Oxide Films Formed under Prolonged Anodizing,” *Journal of the Electrochemical Society,* vol. 122, no. 12, pp. 1645-1653, December 1975.

[77] F. Keller, M. Hunter and D. Robinson, “Structural Features of Oxide Coatings on Aluminium,” *Journal of Electrochemical Society,* vol. 100, no. 9, pp. 411-419, January 1953.

[78] S. Wernick, R. Pinner and P. Sheasby, The Treatment Treatment and Finishing of Aluminium and its Alloys, 5th ed., Trowbridge: Redwood Burn Limited, 1987.

[79] R. Wegman and J. van Twisk, Surface Preparation and Bonding Techniques, 2nd ed., Oxford: William Andrew, Elsevier, 2012.

[80] J. Venables, D. McNamara, J. Chen and T. Sun, “Oxide Morphologies on Aluminium Prepared for Adhesive Bonding,” *Applications of Surface Science,* vol. 3, no. 1, pp. 88-98, July 1979.

[81] L. Domingues, J. Fernandes, M. Da Cunha Belo and M. Ferreira, “Anodising of Al 2024-T3 in a Modified Sulfuric Acid/Boric Acid Bath for Aeronautical Applications,” *Corrosion Science,* vol. 45, p. 149–160, March 2003.

[82] European Union, “Directive 200/53/EC of the European Parliament and of the Council,” 2000.

[83] M. Fedel, “Environmentally Friendly Hybrid Coatings for Corrosion Protection: Silane Based Pre-treatments and Nanostructured Waterborne Coatings,” PhD Thesis, University of Trento, 2010.

[84] B. Johnsen, “Adhesive Bonding of Aluminium,” PhD Thesis, Norwegian University of Science and Technology, 2003.

[85] European Union, “Europa,” European Union, 13 July 2011. [Online]. Available: http://europa.eu/legislation_summaries/environment/waste_management/l28045_en.htm.

[86] N. Voevodin, N. Grebasch, W. Soto and L. Kasten, “An Organically Modified Zirconate Film as Corrosion-resistant Treatment for Aluminium 2024-T3,” *Progress in Organic Coatings,* vol. 41, pp. 287-293, 2001.

[87] G. Nitowski, “Topographic and Surface Chemical Aspects of the Adhesion of Structural Epoxy Resins to Phosphorus Oxo Acid Treated Aluminium Adherends,” PhD Thesis, Virginia Polytechnic Institute and State University, 1998.

[88] J. Osbourne, “Observations on Chromate Conversion Coatings from a Sol-Gel Perspective,” *Progress in Organic Coatings,* vol. 41, pp. 280-286, 2001.

[89] A. Hughes, R. Taylor and B. Hinton, “Chromate Conversion Coatings for 2024 Al Alloy,” *Surface and Interface Analysis,* vol. 25, pp. 223-234, 2007.

[90] A. Rider, C. Olsson-Jacques and D. Arnott, “Influence of Adherend Surface Preparation on Bond Durability,” *Surface and Interface Analysis,* vol. 27, pp. 1055-1063, 1999.

[91] A. Rider and D. Arnott, “Boiling Water and Silane Pre-treatment of Aluminium Alloys for Durable Adhesive Bonding,” *International Journal of Adhesion and Adhesives,* vol. 20, pp. 209-220, 2000.

[92] M. Abel, R. Digby, I. Fletcher and J. Watts, “Evidence of Specific Interaction Between Glycidoxypropyltrimethoxysilane and Oxidized Aluminium using High-mass Resolution TOF-SIMS,” *Surface and Interface Analysis,* vol. 29, no. 2, pp. 115-125, February 2000.

[93] D. Berry and A. Namkanisorn, “Fracture Toughness of a Silane Coupled Polymer-Metal Interface: Silane Concentration Effects,” *The Journal of Adhesion,* vol. 81, pp. 347-370, 2005.

[94] J. Watts, “The interfacial chemistry of adhesion: Novel routes to the holy grail,” in *Adhesion - Current Research and Application*, Weinheim, 2005 WILEY-VCH Verlag GmbH & Co, 2005, pp. 1-16.

[95] A. Vreugdenhil, V. Balbyshev and M. Donley, “Nanostructured Silicon Sol-Gel Surface Treatments for Al 2024-T3 Protection,” in *78th Annual Meeting of the Federation of Societies of Coatings Technology*, Chicago, IL, 2000.

[96] A. Rider, “Surface Properties Influencing the Fracture Toughness of Aluminium-Epoxy Joints,” PhD Thesis, University of New South Wales, 1998.

[97] J. Hu, L. Liu, J. Zhang and C. Cao, “Electrodeposition of Silane Films on Aluminium Alloys for Corrosion Protections,” *Progress in Organic Coating,* vol. 58, pp. 265-271, 2007.

[98] Momentive Performance Materials, “Momentive Performance Materials,” [Online]. Available: http://www.momentive.com/products/showtechnicaldatasheet.aspx?id=10050. [Accessed 20 January 2014].

[99] 3M, “3M Surface Pre-Treatment AC -130,” February 2012. [Online]. Available: http://multimedia.3m.com/mws/mediawebserver?mwsId=SSSSSufSevTsZxtUoYtx5Y_BevUqevTSevTSevTSeSSSSSS%EF%BF%BD&fn=TDS_AC130_AC130-2.pdf.

[100] R. Atkinson, “Hexcel,” 16 June 2004. [Online]. Available: http://www.hexcel.com/news/archive/news-20040616. [Accessed 6 November 2013].

[101] J. Bishopp, “The History of Redux and the Redux Bonding Process,” *Inernational Journal of Adhesion and Adhesives,* vol. 17, pp. 287-301, 1997.

[102] C. Wang and P. Chalkley, “Plastic Yielding of a Film Adhesive under Multi-axial Stresses,” *Internation Journal of Adhesion and Adhesives,* vol. 20, pp. 155-164, 2000.

[103] R. Govender, “Characterisation of Glass Fibre Polypropylene and GFPP Based Fibre Metal Laminates at High Strain Rates,” PhD Thesis, University of Cape Town, 2011.

[104] A. Zehnder, “Fracture Mechanics,” PhD Thesis, Cornell University, 2007.

[105] J. Reeder, “A Bilinear Failure Criterion for Mixed-mode Delamination,” *Composite Materials: Testing and Design,* vol. 11, pp. 303-322, 1993.

[106] R. Alderstein, “Analytical Prediction Model for Fatigue Crack Propagation and Delamination Growth in GLARE,” *International Journal of Fatigue,* vol. 29, pp. 628-646, 2007.

[107] R. Alderstein, J. Schijve and J. van der Zwaag, “Application of the Energy Release Rate Approach for Delamination Growth in GLARE,” *Engineering Fracture Mechanics ,* vol. 73, pp. 697-709, 2006.

[108] B. Davidson, S. Gharibian and L. Yu, “Evaluation of the Energy Release Rate-based Approaches for Predicting Delamination Growth in Laminated Composites,” *International Journal of Fracture,* vol. 105, pp. 343-365, 2000.

[109] A. Vlot, “Impact Properties of Fibre Metal Laminates,” *Composites Engineering,* vol. 3, no. 10, pp. 911-927, 1993.

[110] J. Laliberte, C. Poon and P. Straznicky, “Low Velocity Impact Damage in GLARE Fibre Metal Laminates,” *American Institute for Aeornautics and Astronautics,* vol. 43, no. 11, pp. 2445-2462, 2005.

[111] P. Cortés and W. Cantwell, “The Impact Properties of High Temperature Fiber Metal Laminates,” *Journal of Composite Materials,* vol. 41, no. 5, pp. 613-632, 2007.

[112] G. Reyes, P. Compston, F. Gullen, W. Cantwell and N. Jones, “The Impact Resistance of Thermoplastic-based Fibre Metal Laminates,” in *Proceedings of the 13th International Conference for Composite Materials*, Beijing, 2001.

[113] G. Reyes and W. Cantwell, “The Mechanical Properties of Fibre-metal Laminates Based on Glass Fibre Reinforced Polypropylene,” *Composites Science and Technology,* vol. 60, pp. 1085-1094, 2000.

[114] M. Ardakani, A. Khatibi and S. Ghazavi, “A Study on the Manufacturing of Glass-Fiber-Reinforced Aluminium Laminates and the Effect of the Interfacial Adhesive Bonding on the Impact Behavior.,” in *Society for the Experimental Mechanics XIth International Congress and Exposition*, Orlando, 2008.

[115] E. Cody, “Pan Am Jet Crashes in Scotland, Killing 270,” Washington Post Foreign Service, 1988.

[116] F. Bagnolia, M. Bernabei, D. Figueroa-Gordonb and P. Irving, “The Response of Aluminium/GLARE Hybrid Materials to Impact and to In-plane Fatigue,” *Materials Science and Engineering A,* vol. 523, pp. 118-124, May 2009.

[117] J. Kim, D. MacKay and Y. Mai, “Drop-weight Impact Damage Tolerance of CFRP with Rubber-modified Epoxy Matrix,” *Composites,* vol. 24, no. 6, pp. 485-494, 1993.

[118] B. Briscoe, R. Court and D. Williams, “The Effects of Fabric Weave and Surface Texture on the Interlaminar Fractue Toughness of Aramid/Epoxy Laminates,” *Composites Science and Technology,* vol. 47, no. 3, pp. 261-270, 1993.

[119] S. Blake, K. Berube and R. Lopez-Anido, “Interlaminar Fracture Toughness of Woven E-glass

Fabric Composites," *Journal of Composite Materials,* vol. 46, no. 13, pp. 1583-1592, 2012.

[120] D. Hunston, A. Kinloch and S. Wang, "Micromechanics of Fracture in Structural Adhesive Bonds," *Journal of Adhesion,* vol. 28, no. 2-3, pp. 103-114, 1989.

[121] Gurit, "Gurit - Marine Product Catalogue," 2012. [Online]. Available: http://www.gurit.com/files/documents/marine-product-catv15pdf.pdf. [Accessed July 2013].

[122] Gurit, "AMT Composites," 8 June 2011. [Online]. Available: http://www.amtcomposites.co.za/sites/default/files/data-sheets/prime-20lvv8pdf.pdf. [Accessed June 2013].

[123] Hexcel, "Hexcel Composites," 2010 March. [Online]. Available: http://www.hexcel.com/Resources/DataSheets/Adhesives-Data-Sheets/609_eu.pdf. [Accessed June 2013].

[124] S. George, Interviewee, *Anodising of aluminium.* [Interview]. March 2012.

[125] C. Boothroyd, "Lecture Slides: Microanalysis in the Electron Microscope," 16 September 2010. [Online]. Available: http://phyweb.physics.nus.edu.sg/~phybcb/teaching/DTU%20Adv%20EM%20EDX%2030.pdf.

[126] ASTM D7264, *Standard Test Method for Flexural Properties of Polymer Matrix Composite Materials,* ASTM International, 2007.

[127] Cytec, "FM94 Adheisive Film Technical Data Sheet," 29 March 2010. [Online]. Available: http://www.cemselectorguide.com/pdf/FM_94_032910.pdf. [Accessed 6 November 2013].

[128] P. Joyce, "Mechanical Testing of Composites," 2003. [Online]. Available: http://www.usna.edu/Users/mecheng/pjoyce/composites/Short_Course_2003/12_PAX_Shor

t_Course_Mechanical-Testing.pdf.

[129] Y. Zhang and G. Spinks, “An Atomic Force Microscopy Study of the Effect of Surface Roughness on the Surface Roughness on the Fracture Energy of Adhesively Bonded Aluminium,” *Journal of Adhesion Science and Technology,* vol. 11, no. 2, pp. 207-223, 1997.

[130] G. Sulka and K. Parkola, “Anodising Potential on Well-ordered Nanostructures Formed by Anodisation of Aluminium in Sulphuric Acid,” *Thin Solid Films,* vol. 515, pp. 338-345, 2006.

[131] S. Yoon and C. Hong, “Modified End Notch Flexure System for Mixed Mode Interlaminar Fracture in Laminated Composites,” *International Journal of Fracture,* vol. 43, pp. R3-R9, 1990.

[132] F. Hashagen and R. de Borst, “Numerical Assessment of Delamination in Fibre Metal Laminates,” *Computer Methods in Applied Mechanics and Engineering,* vol. 185, pp. 141-159, 2000.

[133] G. Lawcock, L. Ye and Y. S. C. Mai, “Effects of fibre/matrix adhesion on carbon-fibre reinforced metal laminates -II: Impact behaviour,” *Composites Science and Technology,* vol. 57, no. 12, pp. 1621-1628, 1998.

[134] F. Yan, K. Qi, J. Rose and H. Weiland, “Delamination Defect Detection Using Ultrasonic Guided Waves in Advanced Hybrid Structureal Elements,” in *American Institute of Physics Conference Proceedings*, Annapolis, 2010.

[135] M. Alves and R. Oshiro, “A Methodology for Scaling Impacted Structures,” *Impact Loading of Lightweight Structures,* vol. 49, pp. 17 - 34, 2005.

[136] S. McKown, W. Cantwell and N. Jones, “Investigation of Scaling Effects in Fiber Metal Laminates,” *Journal of Composite Materials,* vol. 42, pp. 865 - 888, 2008.

[137] P. Pintado and J. Morton, “On the Scaling of Impact Loaded Composite Beams,” *Composite Structures,* vol. 27, no. 4, pp. 357-365, 1994.

[138] NextEngine, “NextEngine 3D HD scanner,” NextEngine , [Online]. Available: http://www.nextengine.com/products/scanner/features/accurate.

[139] J. Carrillo and W. Cantwell, “Scaling Effects in the Low Velocity Impact Response of Fiber-Metal Laminates,” *Journal of Reinforced Plastics and Composites,* vol. 27, no. 9, pp. 893-907, 2008.

[140] F. Galal, C. Soutis and A. Hodzic, “Blast Resistance and Damage Modelling of Fibre Metal Laminates to Blast Loads,” *Applied Composite Materials,* vol. 19, pp. 619-636, 2012.

[141] D. Karagiozova, G. Langdon, G. Nurick and S. Chung Kim Yuen, “Simulation of the Response of Fibre-metal Laminates to Localised Blast Loading,” *International Journal of Impact Engineering,* vol. 37, pp. 766-782, 2010.

[142] C. Soutis, A. Mohamed and A. Hodzic, “Modelling the Structural Response of GLARE Panels to Blast Load,” *Composite Structures,* vol. 94, pp. 267-276, 2011.

APPENDICES

A. ADDITIONAL SLB TEST RESULTS

The energy release rates of alodined surfaces are shown in Figure A.1, where the one series was adhered with the film adhesive (SLR) and the other without (SL). Both sets of SLB specimens were manufactured with prepreg. This figure was used to illustrate how inconsistencies affected the mean energy release rate trend line. The energy release rates of the individual specimens are plotted with markers and dotted or dashed lines, the mean energy release rate is plotted by the solid lines and the shaded areas represent the standard deviation.

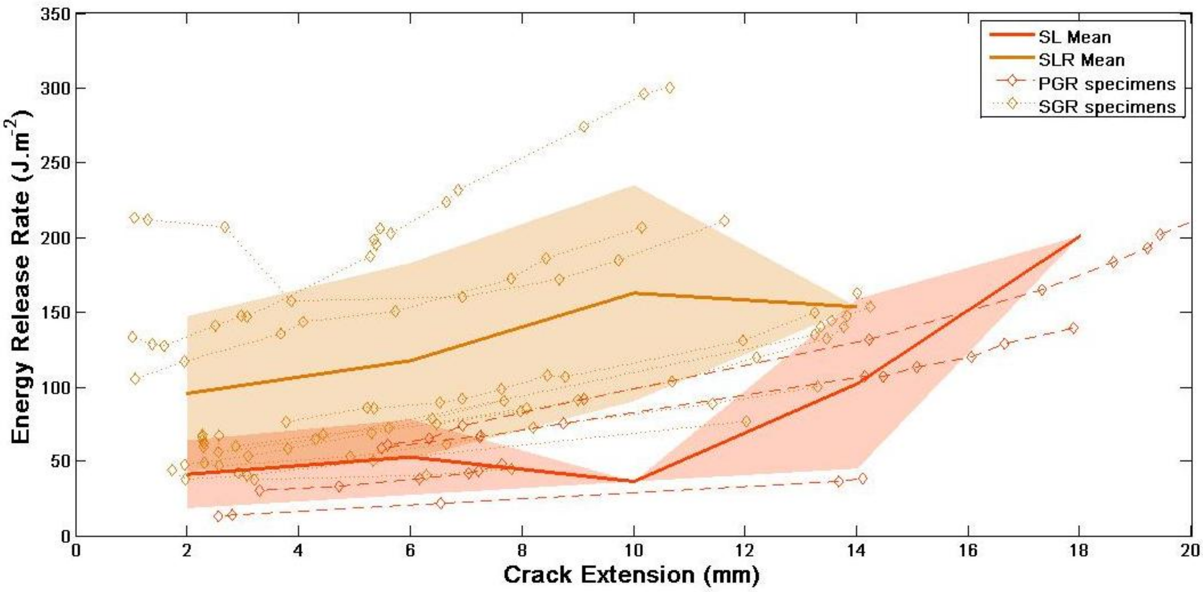

Figure A.1: The energy release rate of alodined and prepreg SLB specimens of which one was prepared with a film adhesive (SLR) and one without (SL)

The individual specimens of the SL series exhibited a linear increase in energy release rate with crack extension, but the mean energy release rate exhibited a decrease in the energy release rate at 10mm of crack extension at which point the standard deviation also decreased completely. This was created by a lack in data points in that range of crack extension, which in was caused by a 5 second time delay in the camera timer function between subsequent sets of the custom timer which captured 10 images with 3 second time intervals.

The individual specimens of the SLR series exhibited an approximately linear increase in the energy release rates with crack extension, where the mean energy release rate trend line increased linearly and then decreased towards 14mm of crack extension. The decrease was as a result of the crack growth of the SLR specimens above the trend line only being recorded up to 12mm crack extension. The decrease in the mean energy release rate at 14mm was as a result of only the specimens below the mean being included in the average value at that point. This could have been caused by small variations of the position of the specimen on the supports of the Three Point Bend rig or premature termination of an experiment.

B. PRELIMINARY IMPACT RESULTS

B.1. OBJECTIVES

The preliminary impact tests were performed to determine which manufacturing technique would produce FMLs with the best impact response with regards to damage absorption. The different techniques included the use of different glass fibre fabrics to determine their response to impact.

B.2. MANUFACTURING:

The FMLs for impact testing were prepared using four different techniques and the materials used are summarised in Table D.1. The techniques described in Section 3.5.2 were used to manufacture the FML specimens as well as the UD lay-up technique and VARTM technique described further.

FMLs were prepared in two stages. Four FMLs with dimensions 300mm x 300mm were manufactured at the University of Cape Town (UCT). The aluminium alloy 2024-T3 was used and the aluminium was alodined prior to the manufacturing process. These FMLs were transported to the University of Liverpool where they were each cut up with a band saw into nine FMLs of equivalent size. Holes were drilled in to the 100mm x 100mm FMLs with a drill press such that the holes lined up with those of the clamp frame.

Table B.1: Summary of preliminary impact FML specimens

Specimen Code	**Manufacturing method**	**Glass Fibre**	**Resin**
SPP	Dry lay-up (Prepreg)	Woven	SE 84 LV
PWW	Wet lay-up	Woven	Prime 20 LVLV
PUW	Wet lay-up	UD	Prime 20 LVLV
PIN	VASRTM (Infusion)	Injectex	Prime 20 LVLV

B.2.1. WET LAY-UP PRODUCTION OF UD AND WOVEN GF FMLS

The wet lay-up technique was used to produce FMLs composed of both UD and woven glass fibre, the lay-up of which is displayed in Figure B.1. The UD glass fibre FML plies were arranged according to the Al/0°/90°/Al/90°/0°/Al GLARE configuration, the production of which will be described. The differences in the production of FMLs with woven glass fibre will be discussed separately.

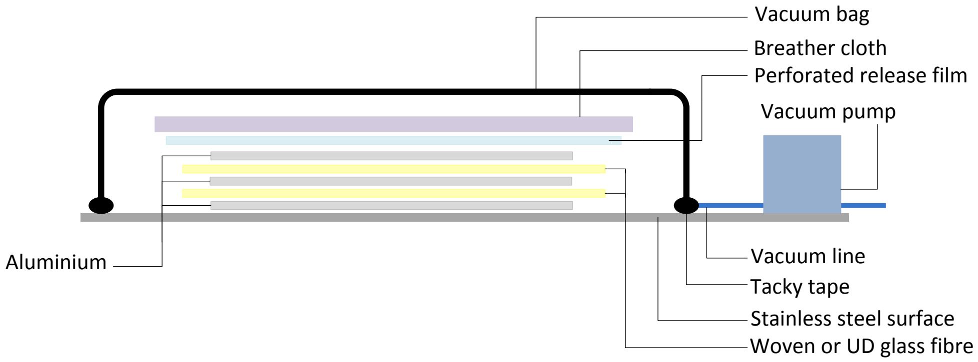

Figure B.1: Wet lay-up configuration of FMLs

UD GF WET LAY-UP

(a) The aluminium was degreased via the solvent wipe method. The first sheet of aluminium was coated with Prime 20 LV resin premixed with LV hardener and was placed on the stainless steel surface, with the coated side facing upward.

(b) A sheet of UD glass fibre (GF) was placed over the aluminium and a paint brush was used to impregnate it with resin. The direction of the glass fibre was designated 0°.

(c) A second sheet of UD GF was placed over the first and consolidated with resin. The ply was arranged at 90° relative to the first sheet.

(d) A second sheet of aluminium was coated with Prime 20 LV resin on both sides. The aluminium sheet was placed exactly over the first sheet of aluminium. It is possible to see the outline of the underlying aluminium sheet as the GF became transparent when wetted out.

(e) A third sheet of GF is placed over the aluminium and impregnated with resin. The fibres were orientated at 90°, the same as the sheet in (c).

(f) A fourth sheet of GF was placed over the third at an orientation of 0° and consolidated with resin.

(g) The third sheet of aluminium was coated with resin on one side and is placed with the resin side down on top of the lay-up.

(h) A sheet of non-perforated release film was placed over the lay-up.

(i) A breather cloth layer was placed on top of the lay-up to absorb any excess resin.

(j) The surface surrounding the lay-up was cleaned of any resin and the lay-up was outlined with tacky tape. The lay-up was covered with a vacuum bag which was sealed off with the tacky tape. The vacuum bag was shaped to include pleats that accomodated the three-dimensional shape of the lay-up. A vacuum line was connected to the vacuum bag via a vacuum breach unit. A vacuum pressure of -75kPa was applied which drew excess resin into the breather cloth and removing any air and creating a compression pressure on the lay-up. The lay-up was left under vacuum for 24 hours for the resin to cure The vacuum bag, breather cloth, non-perforated release film and tacky tape were removed once the hardening process had been completed. The FMLs were placed inside the oven and subjected to the Prime 20 LV curing cycle.

WET LAY-UP OF FMLS WITH WOVEN GLASS FIBRE

The lay-up of a FML with woven glass fibre was more straightforward, because the fibre direction of the plies did not have to be considered. Three sheets of woven glass fibre were used between adjoining sheets of aluminium because the areal density of the woven glass fibre was significantly lower.

B.2.2.VARTM OF FMLS

The resin transfer moulding technique was used to produce FMLs with Injectex glass fibre only. The lay-up sequence of the infusion process is depicted in Figure B.2. The individual steps of the manufacturing process were explained.

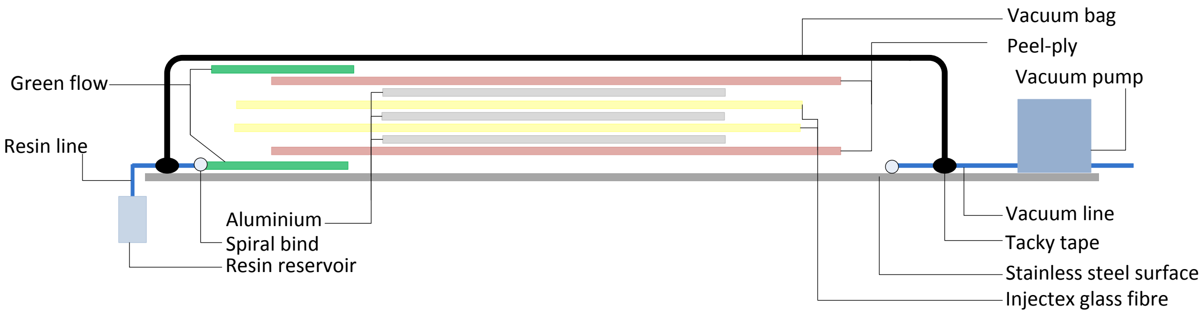

Figure B.2: Configuration of FML infusion

Prior to the start of the manufacturing process, all the glass fibre sheets were weighed as a whole. After the lay-up is complete, Prime 20 LV resin was prepared such that the mass of both the resin and the hardener were equivalent or in excess of the mass of the glass fibre. The resin was put in a resin reservoir which was connected to the resin line.

(a) A piece of green flow was secured to the stainless steel surface with masking tape and tacky tape. The tacky tape was used on the side where the spiral bind would be placed later. The purpose of the green flow was to enhance resin flow.
(b) A sheet of peel-ply was arranged as shown with an overlap of approximately 20mm with the green flow.
(c) The aluminium was placed on the sheet of peel ply close to the edge where the green-flow was, but did not overlap with it.
(d) Three sheets of Injectex GF were placed over the first sheet of the aluminium. Each time the position of the corners was marked with a permanent marker to ensure that the aluminium sheets lined up.
(e) A sheet of aluminium (with Redux 609 on both sides) was placed directly within the marked corners.
(f) Three more sheets of Injectex GF were placed on top of the aluminium as in (d).
(g) The third sheet of aluminium was placed between the marked corners with the Redux 609 side face down.
(h) A second sheet of peel-ply is placed directly over the first one.
(i) A second piece of green flow was placed over the first one. Significant amounts of tacky tape was used such the tacky tape stuck through the green flow mesh.

(j) A single strip of spiral bind was adhered to the tacky tape on the green flow and stretched partially to create space for the resin to flow through freely. A second strip of spiral bind was stuck to the stainless steel surface on the opposite side of the lay-up and also partially stretched. Piping was connected to both strips of spiral bind. The line connected to the spiral bind on the green flow was connected to the resin reservoir and the other line was connected to the vacuum pump.

(k) The lay-up was outlined with tacky tape (with the backing paper still on) and care was taken to secure the vacuum and resin line with tacky tape.

(l) The backing paper was systematically pulled off as the edges of the vacuum bag were bonded to the tacky tape. Pleats in the vacuum allowed space for the 3D shape of the lay-up. The resin line wais clamped off before the vacuum pump was switched on. Care was taken to detect any air leaks in the vacuum bag once all the air had been withdrawn. The resin line was unclamped and the resin front flowed through the resin line and was conducted along the green flow mesh and towards the Injectex glass fibres. Once the resin front had flowed through the FML or once the resin reservoir was almost empty, the resin line was clamped off. The lay-up was left under vacuum for 24 hours for the resin to harden.

The vacuum pump was switched off after 24 hours and the vacuum line, resin line, spiral bind, vacuum bag and tacky tape were discarded. The FML panel was removed from the surface and the peel-ply and green flow layer were peeled off. The panel was post-cured in the oven according to the temperature profile for Prime 20 LV.

B.3. EXPERIMENTAL PROCEDURE

The FMLs were tested on a drop weight setup at the University of Liverpool which was similar to that shown in Figure 4.1.1. The drop mass was kept constant at 2.06kg and the drop height was varied from 0.5 to 1.5m (drop height limit of instrument). A 10m hemispherical indentor was used to impact the specimens. A 20 kN load cell was connected to the indentor and used to measure the force and a high speed camera was used to measure the incident and rebound velocities of the indentor at 10 000 frames a second.

B.4. PRELIMINARY IMPACT RESULTS

The results from these tests were not useful as the near catastrophic delamination occurred on most of the specimens as shown in Figure B.3. The outer aluminium layers were only prevented from complete interfacial debonding by one corner of the FML where adhesion was still intact. The poor performance of these FMLs was ascribed to the machining process that induced weak points which facilitated the delamination process. Very poor bonding of the alodined surfaces also contributed to the interfacial debonding as the absence of surface roughness allowed unobstructed crack propagation.

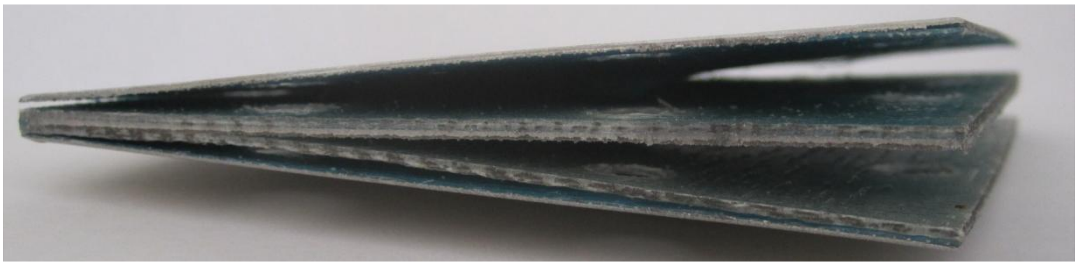

Figure B.3: Photograph of a FML specimen after a preliminary impact test.

C. DEFLECTION AND SEPARATION ZONE CALCULATIONS

The methods used to calculate the deflection and the separation zone areas were described in Chapter 5. This Appendix will elaborate on the reasons the deflections and separations were measured at 1δ deflection or separation respectively. This was illustrated for a typical specimen, referred to as ISS 12, but applies across the range.

The impact damage on the distal face of the FML specimens was localised and the deflection of the FML panels as a whole was minimal. It was important that the deflection of the FML plate was distinguished from the deflection which arose as a result of petalling on the distal face. It can be seen in Figure C.1 that there was a high concentration of contour lines at the centre where the impact event occurred, but the contour lines became sparse towards the edges of the specimen. From this it could be deduced that the majority of the deflection resulted from the petalling.

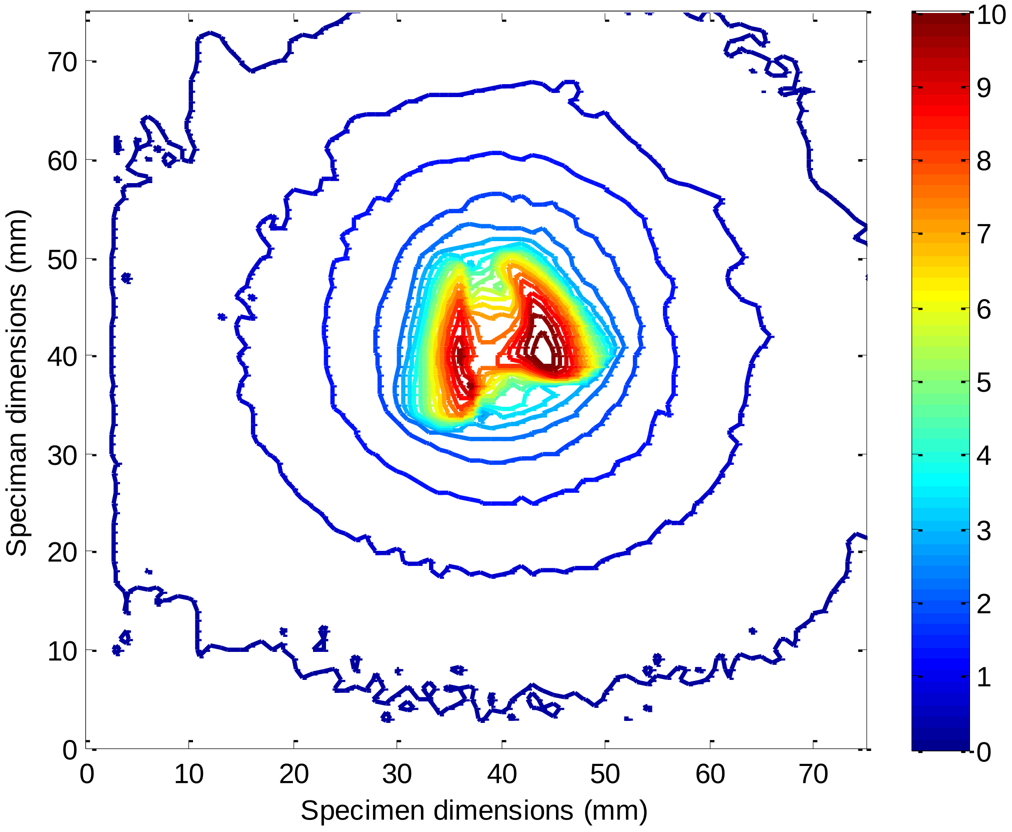

Figure C.1: A contour plot of the distal side of the impact tested ISS 12 specimen

Figure C.2 shows a photo of the petalling on the distal side of the ISS 12 specimen. The petalling was not the only feature on the surface of the aluminium, but ridges could also be seen which affected scanned the surface profile. The ridges that formed on the surface of the aluminium were as a result of excess Redux 609 and SE 84 LV resin being drawn off by the vacuum. These ridges formed in the shape of folds between the vacuum bag and the aluminium. White poster paint was used to dull the aluminium surface such that the incident laser beams used to scan the surface would not be scattered. This poster paint obscured these ridges to some extent, but the ridges were still detected by the scanner as can be seen in Figure C.3

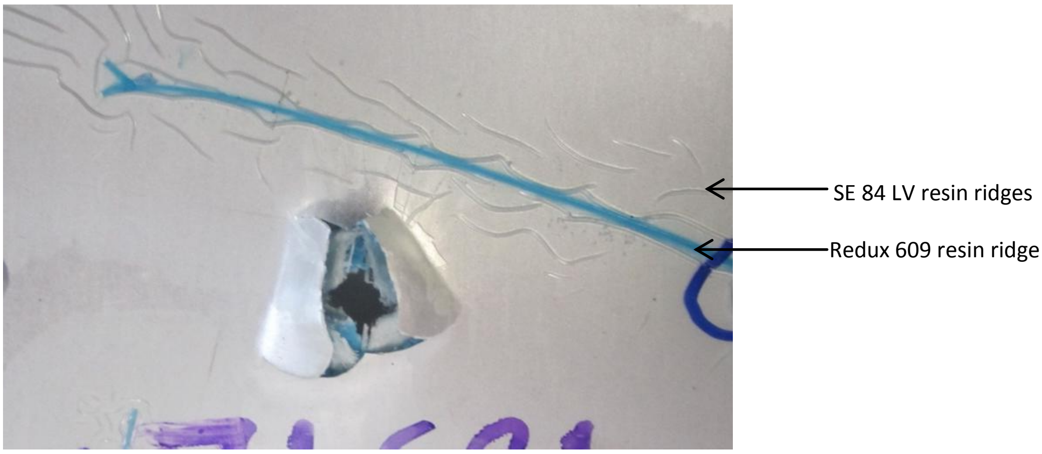

SE 84 LV resin ridges

Redux 609 resin ridge

Figure C.2: Photograph of the distal side of the impacted ISS 12 specimen showing the occurrence of ridges

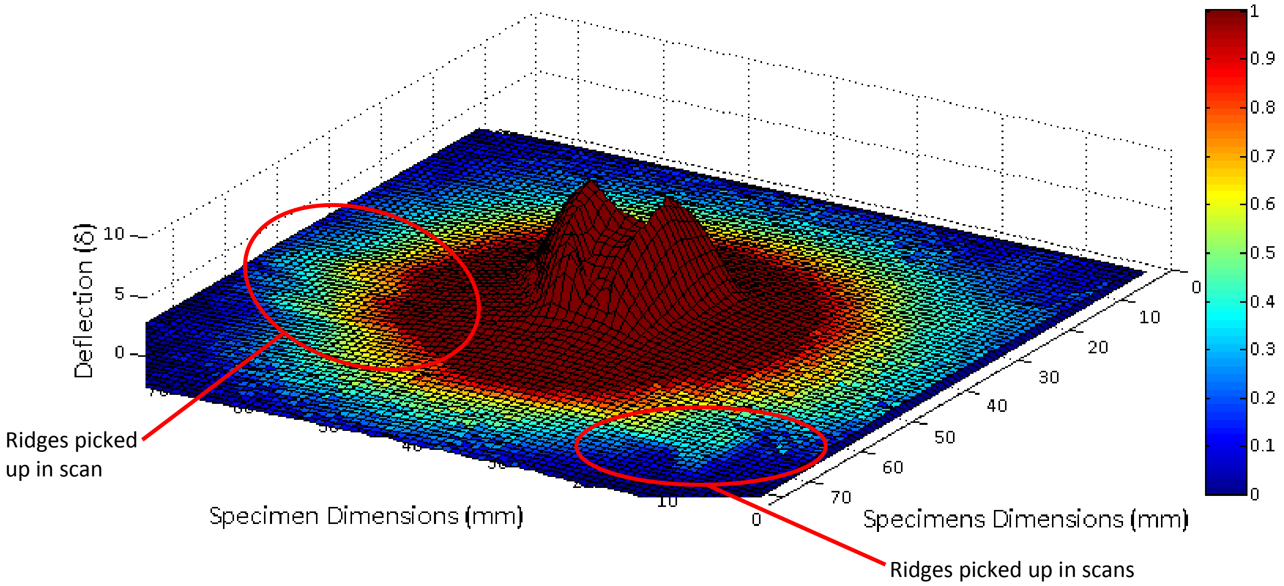

Ridges picked up in scan

Ridges picked up in scans

Figure C.3: A surface plot of the distal face of the impact tested ISS 12 specimen

The colouring of the plot was adjusted so that the surface deflected above 1δ is shown as maroon. This allowed variations in the deflection below 1δ to be highlighted by changes in colour as indicated by the colour bar. The ridges seen in the scan affected the deflection areas when the deflected areas were measured below 1δ, therefore the areas of deflection or separation were not measured below 1δ. The same ridges are observed on the contour plot of specimen ISS 12 in Figure C.4, where only the contour lines from 0.2δ to 1δ are plotted. Bulges can be seen at the location of the ridges which are more pronounced at contour lines with lower deflection values. These bulges are minimal or absent on the 1δ contour line therefore are a better measure of the deflected area.

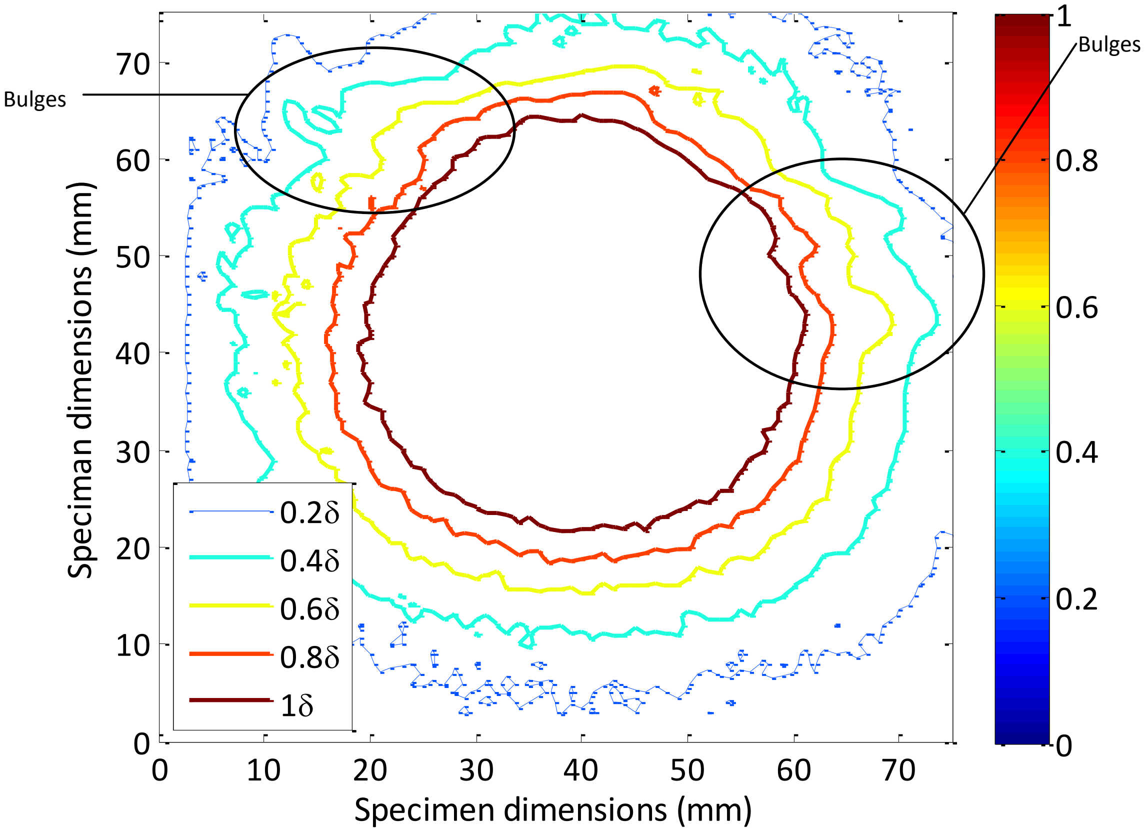

Figure C.4: Contours at 0.2- 1δ on the distal face of the ISS 12 specimen

The deflection contours between 1δ and 2δ are illustrated in Figure C.5(a): the 1δ and 1.2δ contour lines are much further apart than the 1.8δ and 2δ contour lines. The contours lines in Figure C.4(b) almost lie directly on top of each other which suggests a near vertical increase in deflection as a result of petalling. From this it can be deduced that the deflection as a result of petalling becomes significant at approximately 2δ.

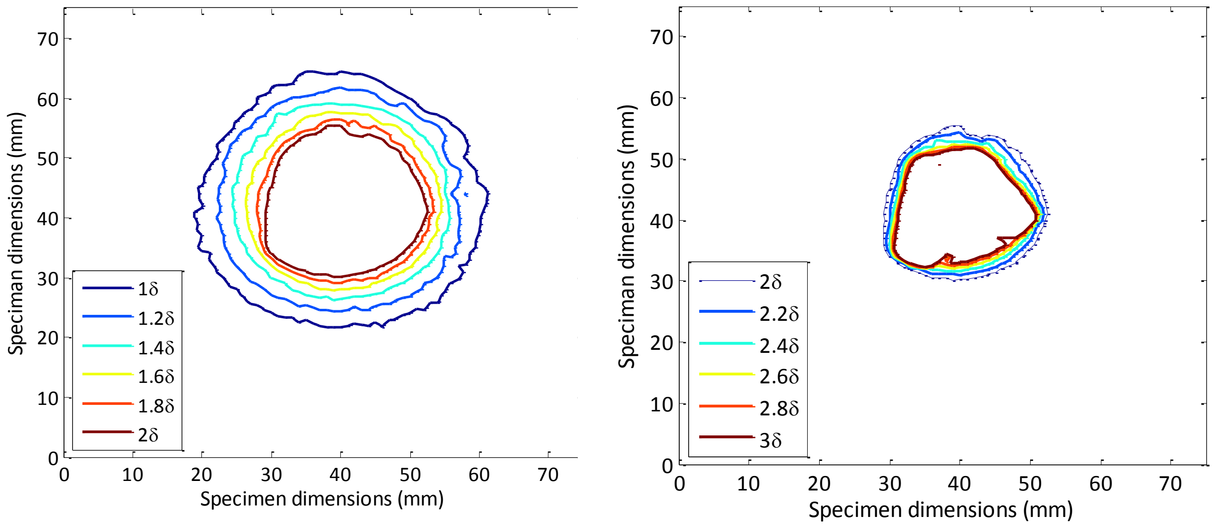

Figure C.5: Contour plots of the ISS 12 specimens' distal face with the deflection ranging between (a) 1-2δ and (b) 2-3δ.

The contour lines that are associated with the deflection caused by the petalling all have a distinct shapes determined by shape of the petalling as seen in Figure C.4(b). The contour lines associated with the deflection at 1δ are circular and independent of the shape of the petalling. This is also seen in Figure 5.2.13 where the shapes of the 1δ contour lines were independent of the shape of the petalling at 2δ.

D. ADDITIONAL IMPACT RESULTS

The separation zone areas of all the impact tested specimens are plotted in Figure D.1 as a function of their non-dimensional energies. The specimens that were circled are the specimens that were selected for comparison based on their individual

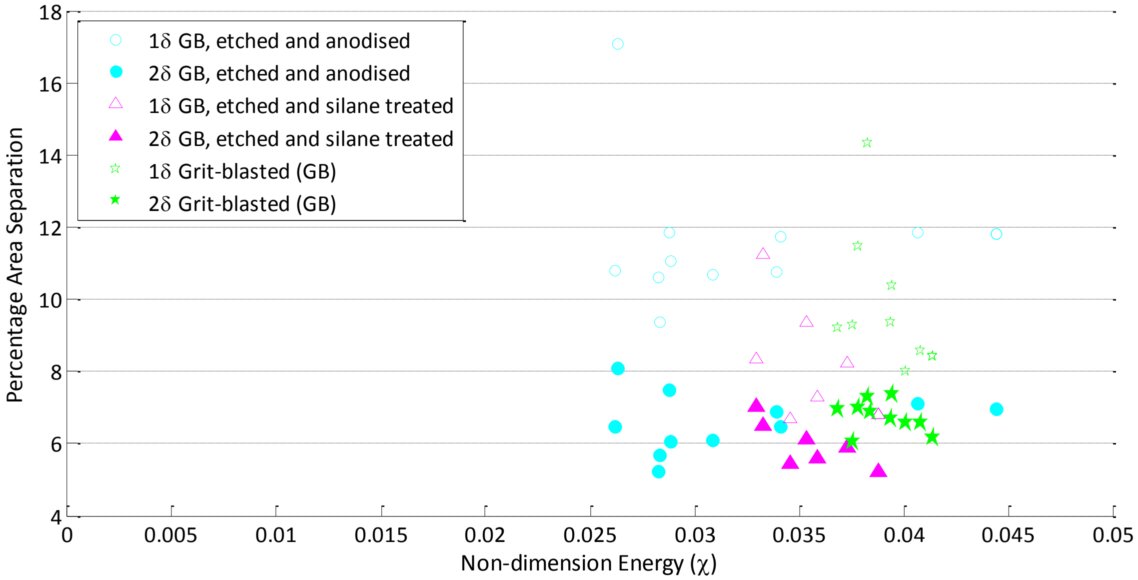

Figure D.1: The areas of the separation zones at 1δ and 2δ separation as percentages of the area exposed to impact.

The deflection areas of all the specimens are plotted as a function of their non-dimensional energies in Figure D.2. The specimens that were circled are the specimens that were compared in sections 5.2.1 and 5.2.2. Table D.1 lists the average damage ratios for all the specimens that were tested and not just those in the 0.0005χ group.

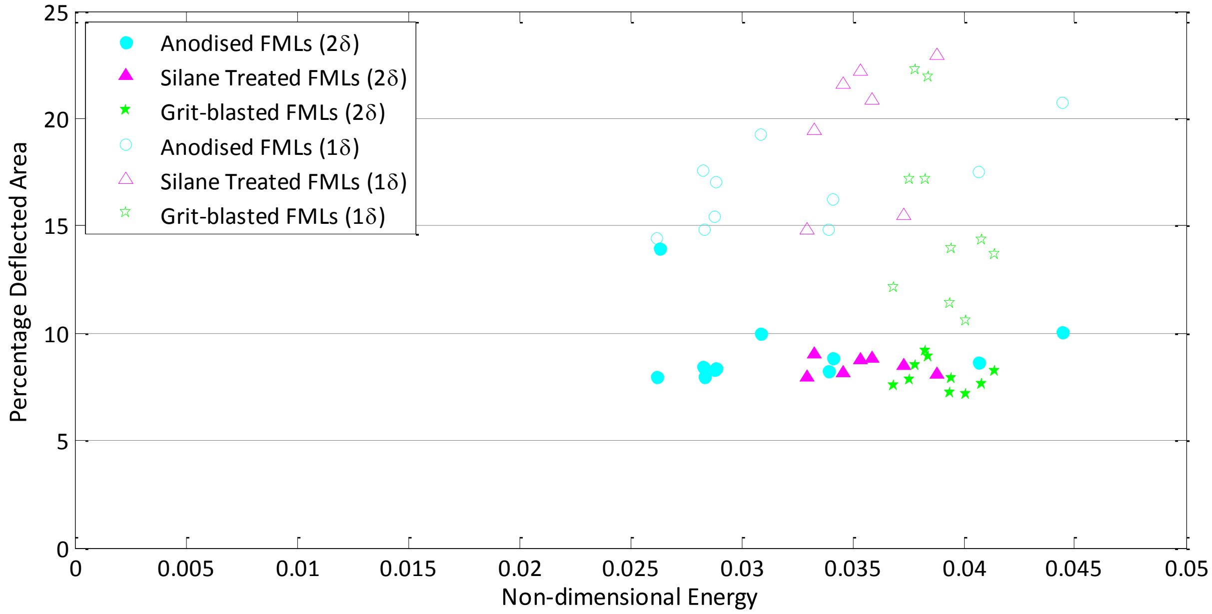

Figure D.2: The percentage 1δ deflection areas of all the impact tested specimens

Table D.1: The average damage ratios for all impact tested specimens

	Anodised FMLs	**Bead-blasted FMLs**	**Silane Treated FMLs**
Separation Area (1δ)	11.3%	10.0%	7.9%
Deflection Area (1δ)	15.5%	17.2%	20.0%
Damage Ratio	0.72%	0.61%	0.40%
Standard deviation	0.001%	0.13%	0.1%